LOCAL PROBE INVESTIGATION OF EMERGENT PHENOMENA IN COMPLEX OXIDE HETEROINTERFACES

by

Mengchen Huang

Bachelor of Science, Nanjing University, 2009

Submitted to the Graduate Faculty of

the Kenneth P. Dietrich School of Arts and Sciences in partial fulfillment

of the requirements for the degree of

Doctor of Philosophy in Physics

University of Pittsburgh

2016

UNIVERSITY OF PITTSBURGH

KENNETH P. DIETRICH SCHOOL OF ARTS AND SCIENCES

This thesis was presented

by

Mengchen Huang

It was defended on

April. 26th. 2016

and approved by

Adam Leibovich, Associate Professor, Department of Physics and Astronomy

Gurudev Dutt, Associate Professor, Department of Physics and Astronomy

Brian D’Urso, Assistant Professor, Department of Physics and Astronomy

David Pekker, Assistant Professor, Department of Physics and Astronomy

Steven R. Little, Professor, Department of Chemical and Petroleum Engineering

Thesis Director: Jeremy Levy, Professor, Department of Physics and Astronomy

LOCAL PROBE INVESTIGATION OF EMERGENT PHENOMENA IN COMPLEX OXIDE HETEROINTERFACES

Mengchen Huang, PhD

University of Pittsburgh, 2016

LOCAL PROBE INVESTIGATION OF EMERGENT PHENOMENA IN COMPLEX OXIDE HETEROINTERFACES

Mengchen Huang, Ph.D.

University of Pittsburgh, 2016

Complex oxide heterointerfaces exhibit rich physics as well as many veiled puzzles. $LaAlO_3$/$SrTiO_3$ (LAO/STO) is one of the prototype of such heterointerfaces. In 2004, Ohtomo and Hwang first reported a conducing interface emerged between perovskite oxide insulators $LaAlO_3$ and $SrTiO_3$. Following this seminal discovery, many emergent phenomena like metal-insulator transition, piezoresponse, superconductivity, magnetism, strong spin-orbit coupling and coexistence of superconductivity and magnetism were reported in the fascinating LAO/STO system. However, the origin of the conducting interface is still the subject of intense debate, and the physics behind these emergent phenomena remains a wild space to be explored. My Ph.D. study focused on the emergent phenomena in LAO/STO by using “local probes” — nanostructures created by conductive atomic force microscope (c-AFM) lithography and the AFM itself. I used piezoresponse force microscope (PFM) to study the electromechanical response in LAO/STO and developed a high-resolution, non-destructive PFM imaging technique to visualize nanostructures at LAO/STO interface. The results indicate that the PFM signal is related to a carrier density mediated interfacial lattice distortion, and surface adsorbates can affect the PFM signal via coupling to the electrons at the interface. I integrated graphene on LAO/STO, created field-effect devices in graphene/LAO/STO and collaborated with Dr. Giriraj Jnawali to investigate the transport properties. The high quality single layer graphene on LAO/STO exhibited the half-integer quantum Hall effect and room temperature weak antilocalization behavior. I performed transport measurements in (110)-oriented LAO/STO to investigate anisotropic quasi one-

dimensional superconductivity in nanowires. Based on the results I proposed a plausible explanation related to the Lifshitz transition and anisotropic band structures of nanowires in (110)-oriented LAO/STO. Co-worked with Dr. Keith Brown, I studied the conductivity switching of LAO/STO interface by solvent immersion and light exposure. We reported a fully reversible, more than four order of magnitude conductance modulation and proposed a surface protonation model. Besides these main research projects that are discussed in this thesis, I also contributed in many other research projects by optimizing the proper sample preparation methods, performing nanostructures fabrication and characterization, and being actively involved in the measurements, data analysis and manuscript preparation.

TABLE OF CONTENTS

LIST OF TABLES

LIST OF FIGURES

PREFACE

Finally, I approach the end of my Ph.D. journey. I want to say thank you to all the people who helped me get to this point.

Thank you, my adviser Jeremy Levy. I still remember the first two things you taught me when I just joined the group, first is not letting the BNC cables dangle in the air and the second is not touching the electronic instruments without hands grounded. These things seem just happened yesterday but now I am going to graduate. Time flies and I will never forget what I have learnt from you, not just knowledge in physics, but also the way of thinking and solving problems. Thank you again for all the invaluable things you have taught me.

Thank you, all my lab mates. Patrick Irvin, Cheng Cen, Guanglei Cheng, Daniela Bogorin, Giriraj Jnawali, Anil Annadi, Yanjun Ma, Dongyue Yang, Feng Bi, Shicheng Lu, Shuo Li, Michelle Tomczyk, Megan Kirkendal, Lu Chen, Jianan Li, Qing Guo, Yunyi Pai and Yuhe Tang. Because of you, the life in the lab is never boring or tough but very colorful. I will always remember your names, your faces, your voice, your smiles and the unique experience we have in LevyLab.

Thank all my committee members for your helpful guidance. Thank all the faculty who taught me courses. Thank all the staff in the department, especially Leyla Hirschfeld and Laura Provolt, for your help in so many things. Thank all the collaborates, especially Prof. Chang-Beom Eom and his group members Chung Wung Bark, Hyungwoo Lee and Sangwoo Ryu for the high quality samples.

Special thanks to my wife, Mrs. Feiling Hu. Her support and encouragement is always there, no matter what happens. Right now I am finishing my Ph.D., I may leave the lovely lab, my dear advisor, my dear lab mates, but my wife will always stay with me in the future journeys in our life.

Looking back on my Ph.D. journey, besides physics, I see tears, laughs, frustration and happiness. They will not show in this thesis but I know they will reappear in front of my eyes from time to time.

1.0 INTRODUCTION

“Often, it may be said that the interface is the device.” stated Herbert Kroemer in his Nobel address [1]. Although this was in reference to the astonishing success of devices based on traditional semiconductors, e.g. silicon, germanium or III-V compounds, it is now particularly important for complex oxide interfaces as well. The symmetry breaking and interplay between spin, charge and lattice in complex oxide heterointerfaces [2] generate a rich spectrum of emergent phases including magnetism, superconductivity, ferroelectricity, ferromagnetism, piezoresponse, and spin-orbit coupling. These exotic phenomena make complex oxides the forefront of modern condensed matter physics and materials science, also possible substitutions for traditional semiconductors in electronic applications [3]. Although traditional semiconductor electronics, e.g. silicon metal oxide semiconductor field-effect transistors (MOSFETs), are still the workhorses of mainstream electronics and will continue in this role for the foreseeable future, there are quantum mechanical limitations of miniaturizing them [4]. One means to overcome these scaling limitations and boost their performance is to combine semiconductor electronics with the correlated electron systems in complex oxides. Growing oxides on silicon substrates was proven to be possible [5]. It is good to say that the (complex oxide) interface is still the device [6].

Despite all these merits, there remain conceptual challenges and technical obstacles to a systematic and comprehensive understanding of the complex oxide heterointerfaces [7]. To realize the full potential of oxide heterointerfaces requires mastering their unique properties. Motivated by that, my graduate research focused on the exotic emergent phenomena in one of the most actively studied complex oxide heterostructures: $LaAlO_3/SrTiO_3$ (LAO/STO). Local probes—nanodevices and nanostructures created by conductive atomic force microscope (c-AFM) lithography as well as the AFM itself, are the tools used to explore the novel phenomena in complex oxide heterostructures at nanoscale dimensions.

The thesis is organized in the following way: the first chapter introduces the key properties of LAO/STO heterostructures. Chapter 2 describes the experiment methods used in my research. Chapter 3 to Chapter 6 describes my main research projects, including piezoresponse force microscopy (PFM) study of LAO/STO (Chapter 3), Field effect and transport study of graphene/LAO/STO (Chapter 4), anisotropic transport properties of nanowires in (110) LAO/STO (Chapter 5) and conductivity switching of LAO/STO governed by surface protonation (Chapter 6). The last chapter is a brief summary of the thesis and gives a future perspective.

The introduction chapter starts from reviewing the basic material properties and electronic structures of LAO/STO, followed by summarizing the reported rich emergent phenomena. Then the material growth method is described and possible explanations of the conducting interface formation are discussed.

1.1 COMPLEX OXIDE HETEROINTERFACES

Heterointerfaces, the interface of heterostructures, have been extensively studied in the past half century. The research in traditional semiconductor heterointerfaces has already been a tremendous success, not only in the fundamental physics concepts but also the real-world device applications. The 1985 Nobel Prize in Physics was awarded for the discovery of quantum Hall effect, first reported in Si MOSFETS. The 1998 Noble Prize in Physics was awarded for the discovery of a new form of quantum fluid with fractionally charged excitations, or fractional quantum Hall effect, first reported in GaAs heterostructures. The 2000 Nobel Prize in physics was awarded for the development of semiconductor heterostructures used in high-speed- and opto-electronics.

In the last decades, a new type of heterointerface composed of complex oxides came into the spot light of condensed matter physics research because it possesses a richness of phenomena that is unparalleled in other solid state systems. The atomic scale control in thin-film growth, enabled by advances in pulsed laser deposition (PLD), molecular beam epitaxy (MBE) and other material growth techniques, led to the arise of complex oxide heterointerfaces. Reminiscent to traditional semiconductor heterointerfaces half a century ago, the challenge and the payback to understand, predict, and tailor the physical properties of complex oxides heterointerfaces are both enormous. In this thesis, the discussion is restricted to one prototype complex oxide heterointerfaces—$LaAlO_3$/$SrTiO_3$, beginning with introducing the bulk properties of the two building blocks, $SrTiO_3$ and $LaAlO_3$.

1.1.1 $SrTiO_3$ (STO)

Strontium titanate ($SrTiO_3$) has been extensively and continuously studied since the 1940s due to its remarkable properties. Under suitable conditions, $SrTiO_3$ (STO) is known to exhibit structural phase transitions, resistive switching, metal-insulator transitions, superconductivity, magnetism, ferroelectricity, nonlinear optical properties, and giant Seebeck coefficients. Another reason for the long-last intensive scientific interest is that STO serves as the near-universal substrate on which complex oxide structures are built and from which their properties are largely inherited [8]. STO is rightfully regarded as the “hydrogen atom of the solid state”.

At room temperature STO is cubic with lattice constant $a_{STO} \approx 3.905$ Å. The cubic structure is composed of an outermost arrangement of eight strontium (Sr) atoms. Centered on each face of the cube is one of six oxygen (O) atoms, which form together the vertices of an octahedral cage. At the center of this cage lies the titanium (Ti) atom (Fig. 1.1a). At $T \approx 105$ K, neighboring oxygen octahedra rotates in opposite directions [9,10] and as a result the cubic symmetry is lower to tetragonal symmetry (Fig. 1.1b). This ferroelastic transition naturally leads to the formation of domains within the STO with different orthogonal orientations of the tetragonal unit cells. Further lowering of the crystal symmetry into orthorhombic structures occurs at lower temperatures [11].

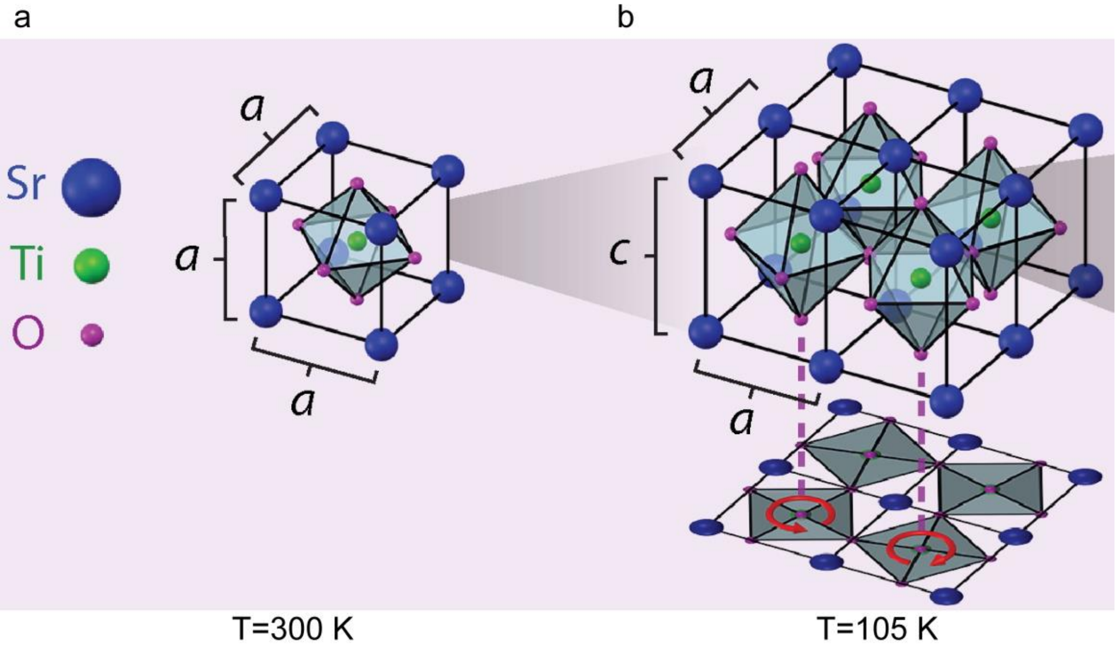

Figure 1.1 $SrTiO_3$ unit cell structure. a, T=300 K, cubic structure. **b,** T=105 K, tetragonal structure. Adapted from ref. [8].

At room temperature STO is paraelectric. The Ti atom is centered inside the oxygen cage and only application of an external electric field can cause Ti displace off-center. Although there are structural phase transitions at lower temperature, the paraelectric state persists for $T \rightarrow 0$ K due to quantum fluctuations, a phenomena termed "quantum paraelectricity" [12]. This quantum paraelectric state is so close to a ferroelectric state that STO is also known as incipient ferroelectric [13]. The dielectric constant of STO rapidly increases with decreasing temperature then gets cut off by the quantum tunneling at a high value of ~20,000 at 4K [14]. By growing thin films of STO on tensile-strained substrates, ferroelectricity can be observed as high as room temperature [15].

Although STO is a band insulator (band gap $E_{gap}^{STO} = 3.2\ eV$), it can be doped to be conducting by, for example, substituting Latium (La) for Sr or Niobium (Nb) substituting Ti or by creating oxygen vacancies [16]. Electric double layer (EDL) gating is another route to dope STO surface to be conducting [17]. At very low temperature (T ~ 300 mK), doped STO becomes a superconductor [18,19], a property shared by many STO-based oxide heterostructures. Bulk STO is non-magnetic, however magnetism emerges in STO-based heterostructures, e.g. LAO/STO [20,21], and can persist at room temperature [22,23]. Besides superconductivity and magnetism, many more emergent phenomena in LAO/STO will be discussed in subsequent sections.

1.1.2 LaAlO$_3$ (LAO)

LaAlO$_3$ (LAO) is the second building block of LAO/STO. At room temperature, LAO is pseudocubic with lattice constant $a_{LAO} \approx 3.789$ Å [24]. The structure of LAO unit cell differs from the cubic perovskite by small anti-phase rotations of the AlO$_6$ octahedra. LAO single crystal substrates have ill-defined surface compared to the untwined STO because of the presence of twinning domains. Therefore LAO is commonly used as thin film on STO substrates to form LAO/STO heterointerfaces.

Like STO, LAO is also a non-magnetic, band insulator (band gap $E_{gap}^{LAO} = 5.6\ eV$). The dielectric constant of LAO is about 25 for temperatures between 300K and 4K [25]. The relatively high value of dielectric, combined with low dielectric loss [26], good lattice matching with many high-temperature superconductors [26-28] and high crystal quality at relatively low costs attainable by Czochralski-growth, make LAO a popular substrate material as well as an appealing gate-dielectric material in field effect devices.

1.1.3 $LaAlO_3/SrTiO_3$ (LAO/STO)

The reasonably small lattice mismatch of 3% between LAO and STO, together with their similar thermal expansion coefficients [28,29] allow the epitaxial growth of LAO on STO. In 2004, Ohtomo and Hwang [30] first reported that if LAO is epitaxially grown on the TiO_2-terminated and (001)-oriented surface of STO, a conducting electron-doped (n-type) sheet is generated at the interface. In most studies of LAO/STO, the crystalline LAO is grown over the (001)-oriented STO substrates, labeled as (001) LAO/STO. It was also reported that a conducting interface can form at (111) LAO/STO [31], (110) LAO/STO [31,32] and even amorphous LAO/STO [33,34]. In this thesis, LAO/STO refers to the regular (001) LAO/STO unless otherwise noted.

1.2 ELECTRONIC STRUCTURE OF LAO/STO INTERFACES

Bulk STO is a band insulator with an energy gap between occupied O_{2p} bands and unoccupied Ti_{3d} bands. The Ti_{3d} orbitals of Ti atom are five-fold degenerated but the degeneracy is lifted in bulk STO by the surrounding oxygen cage (Fig. 1.2a), which splits the levels into a high-energy doublet (e_g states, $d_{3z^2-r^2}$, $d_{x^2-y^2}$) and a low-energy triplet (t_{2g} states, d_{xy}, d_{xz}, d_{yz}). For a given orbital, the hopping matrix elements are much larger in the plane of the lobes than out of the plane of the lobes. For example, for the d_{xy} orbital the hopping is much stronger along the x and y directions than along the z direction (Fig. 1.2b), and as a result the effective mass is lower along the x and y directions than it is along the z direction. The lower effective mass leads to a cigar-shaped Fermi surface along the k_z direction (Fig. 1.2c). The ferroelastic and ferroelectric distortions in bulk STO can lift the degeneracy of the three t_{2g} orbitals, as do spin-orbit interactions and the breaking of inversion symmetry near STO surface or an heterointerface, e.g. LAO/STO [35].

The electronic structure of LAO/STO interfaces is inherited but different from bulk STO. In LAO/STO, DFT calculations [36] and X-ray absorption spectroscopy (XAS) experiments [37] have demonstrated that the lowest available levels in LAO/STO interface is the d_{xy} state (Fig. 1.2d). The band ordering at the LAO/STO interface is reversed compared to the STO bulk, in which the lowest available levels are the d_{yz} and d_{xz} states. Interestingly, for (110) LAO/STO interface [38,39] or (110) STO surface [40], the lowest available levels are still the d_{yz} and d_{xz} states (Fig. 1.2e). These results can also be understood in the point of suppressed inter-plane hopping at the interface or surface (Fig. 1.2f and g) due to the confinement [39,41].

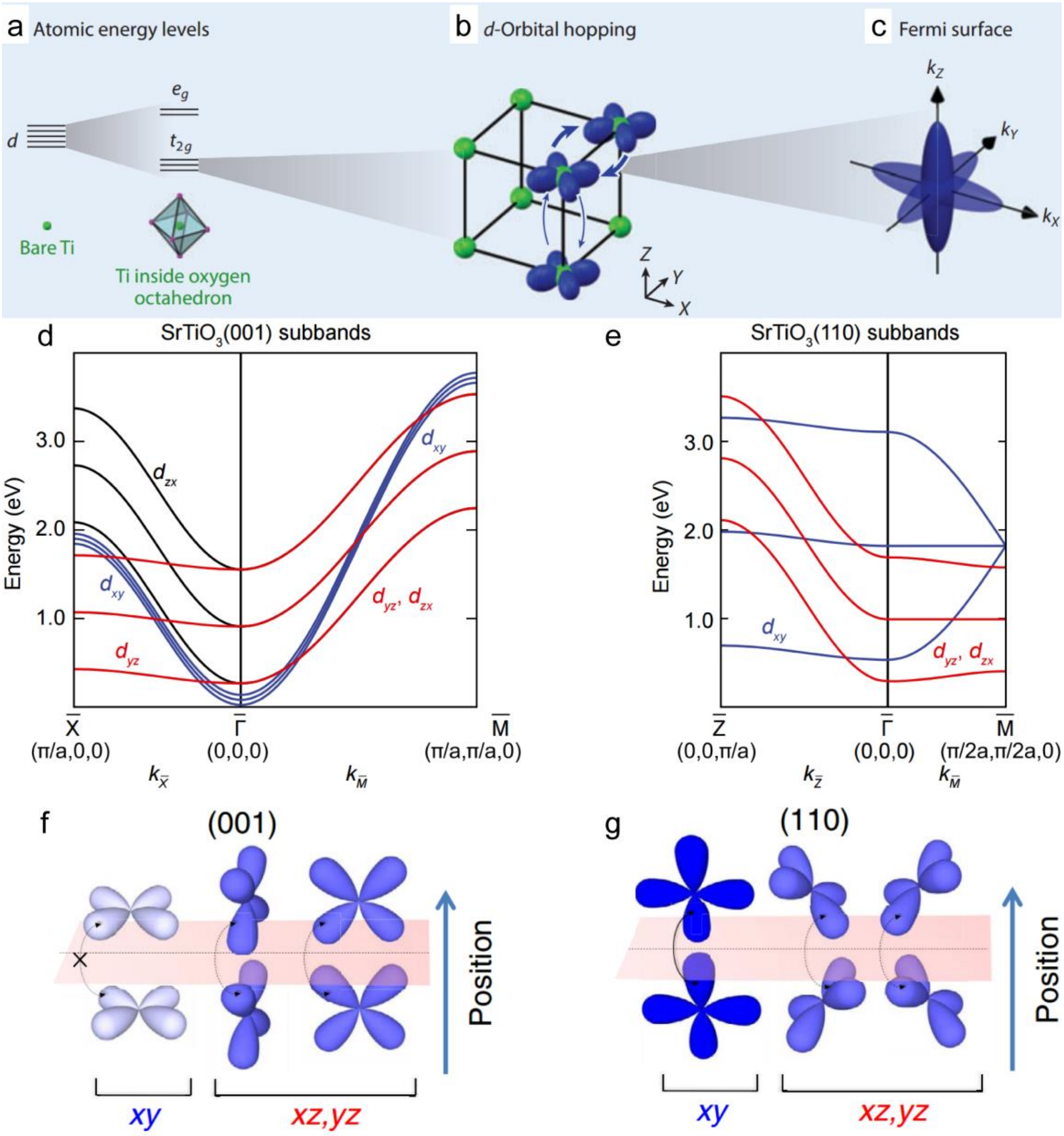

Figure 1.2 Electronic structure of LAO/STO. a, Ti d-orbital energy splitting in STO. **b,** hopping between t_{2g} orbitals. **c,** Fermi surface of STO. **d,** band structure of (001) STO surface and **e,** (110) STO surface. **f,** Inter-plane hopping in (001) LAO/STO and **g,** (110) LAO/STO. Adapted from Ref. [8], [39] and [40].

At conducting LAO/STO interfaces, electrons first occupy Ti d_{xy} orbital, which is strongly two dimensional (2D) with negligible inter-plane coupling. First principle calculations show that d_{xy} orbital electrons are bound at the interface within 2 nm while d_{xz} and d_{yz} electrons can extend farther from the interface [42,43]. Experiments using c-AFM [44], hard x-ray photoelectron spectroscopy [45], Mn dopants substitution at different distances from the interface [46], mapped out that the conducting layer is only several nm. Low temperature superconducting results also pointed out the 2D nature of the conducting interface [47]. Therefore, the conducting LAO/STO interface was initially referred to host a two dimensional electron gas (2DEG). However, electrons in this 2D interface are strongly subjected to electron-electron interactions and therefore referred to form a two dimensional electron liquid (2DEL). Although many researchers are still calling the 2D electron system at LAO/STO as a 2DEG, in this thesis 2DEL is used to represent the 2D electron system. The electron-electron interactions in the 2DEL plays an important role in the rich emergent phenomena at LAO/STO heterointerfaces.

1.3 EMERGENT PHENOMENA AT LAO/STO INTERFACES

Since the seminal discovery of a conducting interface formed at LAO/STO in 2004 [30], over one decade intensive study on LAO/STO has revealed a remarkable variety of emergent phenomena, including metal-insulator transition (MIT) [48,49], superconductivity [47,50], magnetism [20-23], coexistence of superconductivity and magnetism [51-53], spin-orbit coupling [54,55] and piezoresponse [56]. These emergent phenomena can be tuned by, e.g. electric fields, magnetic field, stress etc. Although following sections describe these phenomena separately, they can actually couple with each other and therefore a good theory explaining one phenomena must also accommodate with others.

1.3.1 Metal-insulator Transition

The LAO/STO interface exhibited a metal-insulator transition (MIT) as a function of the LAO layer thickness [48]. The critical LAO thickness of the MIT is $d_c = 4$ unit cell (uc). Below d_c, the interface is insulating; while at or above d_{c}, the interface becomes conducting (Fig. 1.4a). For LAO/STO samples with LAO layer thickness barely below d_{c}, e.g. 3 uc, the interfacial MIT can be controlled by voltages applied to the back of the STO substrate (Fig. 1.4 b). A positive back gate voltage $V_{\mathrm{G,b}}$ drives the insulating 3 uc LAO/STO interface to a conducting state which remains for a time after $V_{\mathrm{G,b}}$ is reset to zero. A negative $V_{\mathrm{G,b}}$ restores the interface to the originally insulating state. For 3 uc LAO/STO, a biased c-AFM tip can tune the interfacial MIT in nanoscale [49]. By manipulating the movement (speed, trajectory etc.) and the bias of the tip, "on-demand" nanodevices and nanostructures can be created at LAO/STO interface [57]. The c-AFM lithography technique will be described in more details in Section 2.3.

There also exists a critical thickness for (111) LAO/STO, (110) LAO/STO and amorphous LAO/STO [31-34], where the c-AFM lithography can still work similarly to the (001) LAO/STO case. The origin of the conducting interface are generally attributed to polar catastrophe, oxygen vacancy, or interfacial cation intermixing (See section 1.5). Surface chemistry also plays an important role in tuning the interfacial conductivity. Chapter 6 focuses on my research project studying the giant conductivity switching of LAO/STO interface governed by surface protonation.

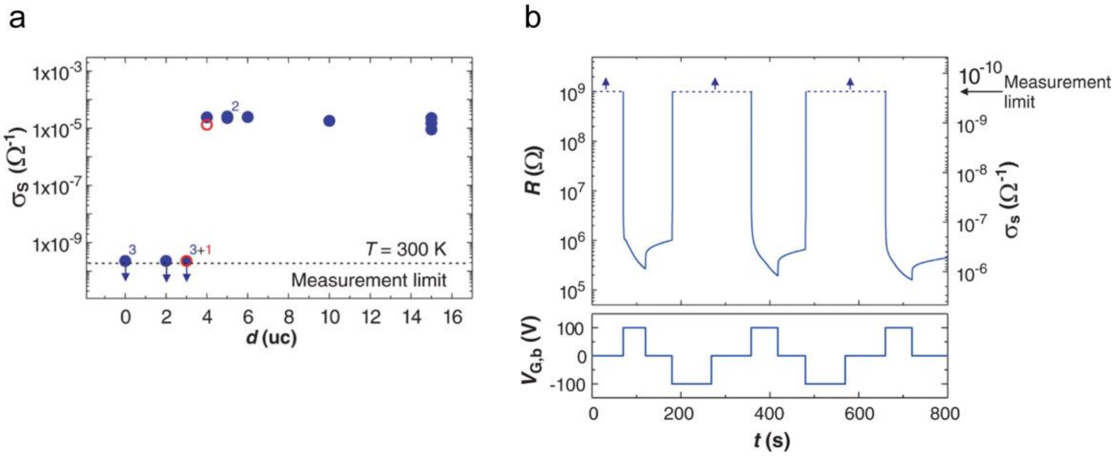

Figure 1.3 Metal-insulator transition (MIT) in LAO/STO interface. a, MIT modulated by the LAO layer thickness. **b,** Tuning the MIT in 3 uc LAO/STO interface by back gate voltages $\boldsymbol{V}_{\mathbf{G,b}}$. Adapted from ref. [48].

1.3.2 Superconductivity

Electron doped SrTiO$_3$ is the first known superconducting semiconductor [18]. At low temperature, a superconducting phase is reported at LAO/STO interface with measured transition temperature T_{c} around 200 mK [50]. Subsequent experiments demonstrated an interfacial superconductor-insulator quantum phase transition [47] controlled by electric fields (Fig. 1.5a). Although it is temperature dependent, the upper critical magnetic field H_{c} is commonly reported to be less than 1 T for out-of-plane filed $H_{\perp}$ and round 1 T to 2 T for in-plane field $H_{\parallel}$ (Fig. 1.5b) [58]. Recently it was discovered that above H_{c}, electrons at LAO/STO interface still form a pairing state without superconductivity [59], suggesting novel strongly correlated electronic phases. Superconductivity was also reported at (110) LAO/STO interface [39]. Chapter 5 describes my research project investigating the anisotropic superconductivity of nanowires at (110) LAO/STO.

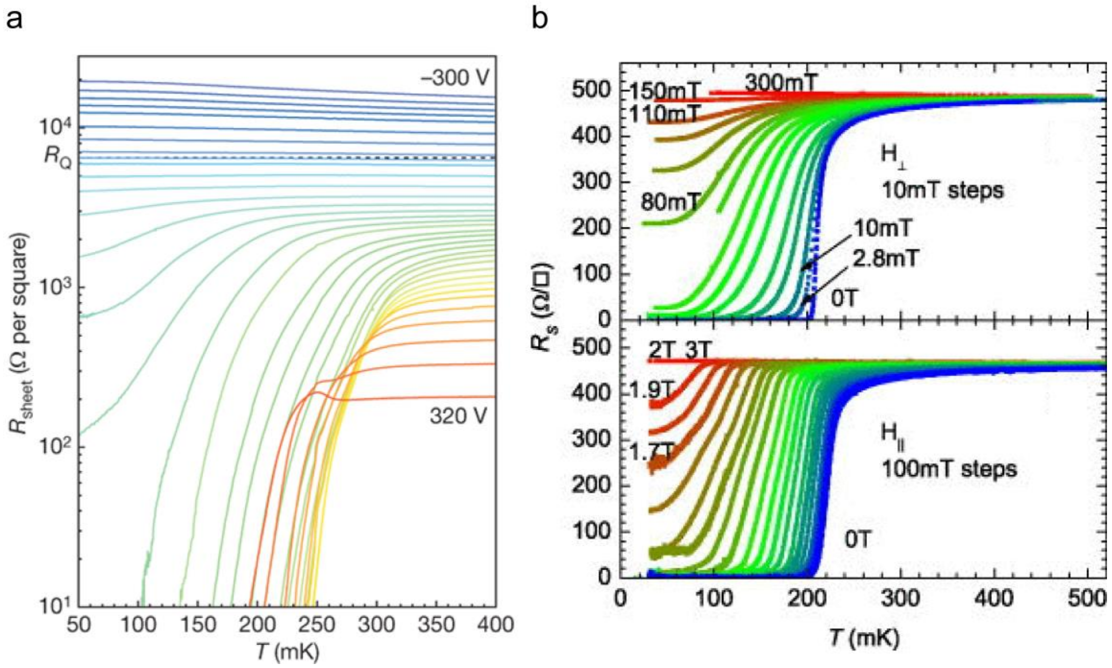

Figure 1.4 Superconductivity in LAO/STO interface. a, Interfacial superconductor-insulator transition modulated by back gate voltages. Adapted from ref. [47]. **b,** Out-of-plane magnetic field $\boldsymbol{H}_\perp$(upper panel) and in-plane magnetic field $\boldsymbol{H}_\parallel$ (lower panel) dependence of the interfacial superconductivity. Adapted from Ref. [58].

1.3.3 Magnetism

Although both LAO and STO are non-magnetic, many experiments demonstrate magnetic properties in the LAO/STO interface. The magnetic signatures were first reported in magneto-transport measurements [20]. A Kondo like temperature dependence of the resistance indicated the presence of magnetic scattering at the interface (Fig. 1.6a). The magnetism was further investigated [21-23] using DC scanning quantum interference device (SQUID) magnetometry (Fig. 1.6b), X-ray magnetism circular dichroism (XMCD) (Fig, 1.6c), and magnetic force microscopy (MFM) (fig 1.6 d). These experiments established that the magnetic moments reside in the plane along the interface and can persist up to room temperature. Generally, the postulated mechanisms of magnetism in LAO/STO invoke localized unpaired d_{xy} electron spins at the interface that couple via exchange with itinerate carriers [60-62]. Oxygen vacancy plays an important role in providing local magnetic moments [63,64].

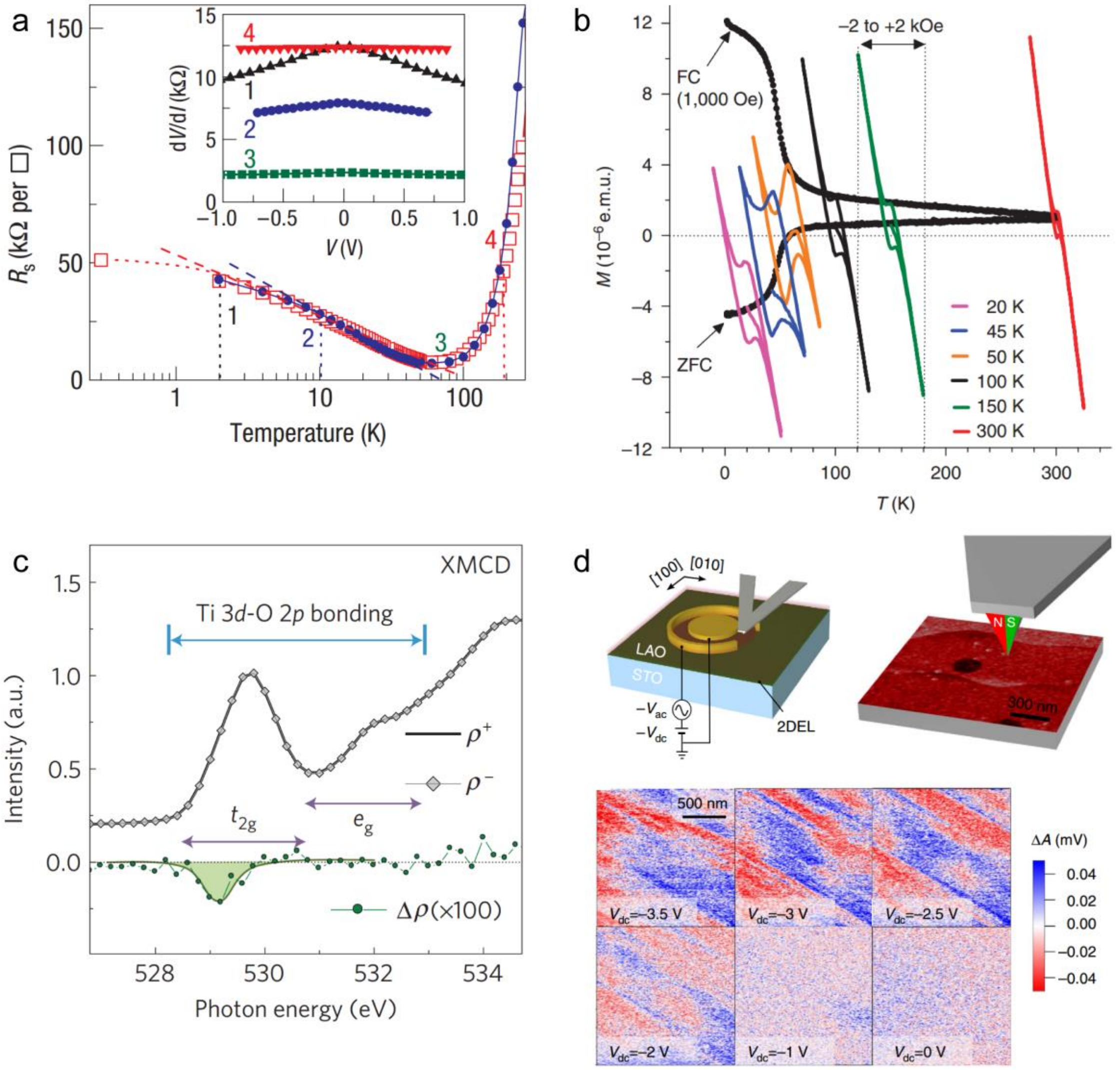

Figure 1.5 Magnetism signal observed in LAO/STO. a, transport measurement results, adapted from Ref. [20]. **b,** scanning quantum interference device **(**SQUID) results, adapted from Ref. [22]. **c,** X-ray magnetism circular dichroism (XMCD) results, adapted from Ref. [21] and **d,** magnetic force microscopy (MFM) results, adapted from Ref. [23].

1.3.4 Coexistence of superconductivity and magnetism

Conventionally superconductivity and magnetism repel each other, but a coexistence of superconductivity and magnetism has been demonstrated in LAO/STO [51-53] by measuring torque magnetometry (Fig. 1.7a-c) or magnetotransport (Fig. 1.3d-f) in the superconducting region. One of the possible explanations is called “phase separation” [22] where magnetism and superconductivity coexist on the same sample but in different areas of the interface. Another important ingredient is spin-orbit coupling [65] since the coupling effect can be strong in LAO/STO and affect both the superconductivity and magnetism.

1.3.5 Spin-orbit coupling

At heterointerface, inversion symmetry breaking happens due to the lattice difference across the interface. Atomic spin-orbit coupling (SOC) combined with such symmetry breaking can lead to a Rashba-like SOC effect. Tunable spin-orbit coupling are reported in LAO/STO interface [54,55]. A steep rise of the SOC strength starts at the quantum critical point which separates the insulating and superconducting states. Theory calculations reveals that SOC in LAO/STO interface has peculiar properties arising from its multi-orbital character [35,66]. SOC in the d_{xy} band has linear momentum dependence whereas in the d_{xz} and d_{yz} bands the momentum dependence is cubic. A large spin splitting can happen at the crossing point of d_{xy} and $d_{yz/zx}$ orbitals (a Lifshiz transition). Theorists also analyzed the effect of SOC on magnetotransport of LAO/STO via calculating the weak anti-localization (WAL) corrections [66]. The Rashba-like SOC can also affect the ferromagnetic exchange in LAO/STO by mediating the zero-field ground state [61].

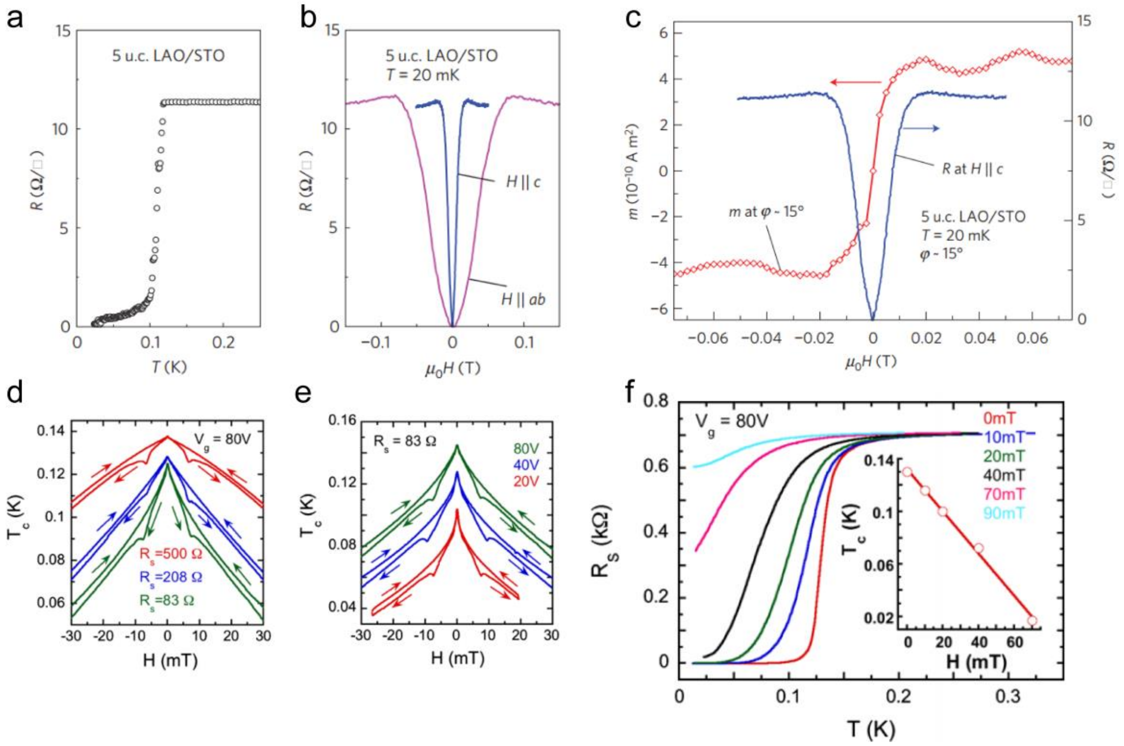

Figure 1.6 Coexistence of superconductivity and magnetic ordering at LAO/STO. a, Temperature (*T*) dependence of the resistance (R). **b,** Magnetic field (*H*) dependence of R in different field directions taken at T = 20 mK. **c,** Sample magnetization (*M*) measured using torque magnetometry at *T* = 20 mK wtih *H* tilts $\varphi \sim 15^{\circ}$ away from the c axis and with *H* parallel to the c axis. **d,** Phase diagram, T_c vs *H*, for a gate voltage of V_g = 80 V, where the superconducting properties are maximal. **e,** Phase diagrams at a bias point of R_s = 83 Ω. **f,** Superconducting transition for V_g = 80 V at a few different magnetic fields. Insert: T_c vs. *H*. Panel **a, b** and **c** are adapted from Ref. [51]. Panel **d, e** and **f** are adapted from Ref. [53].

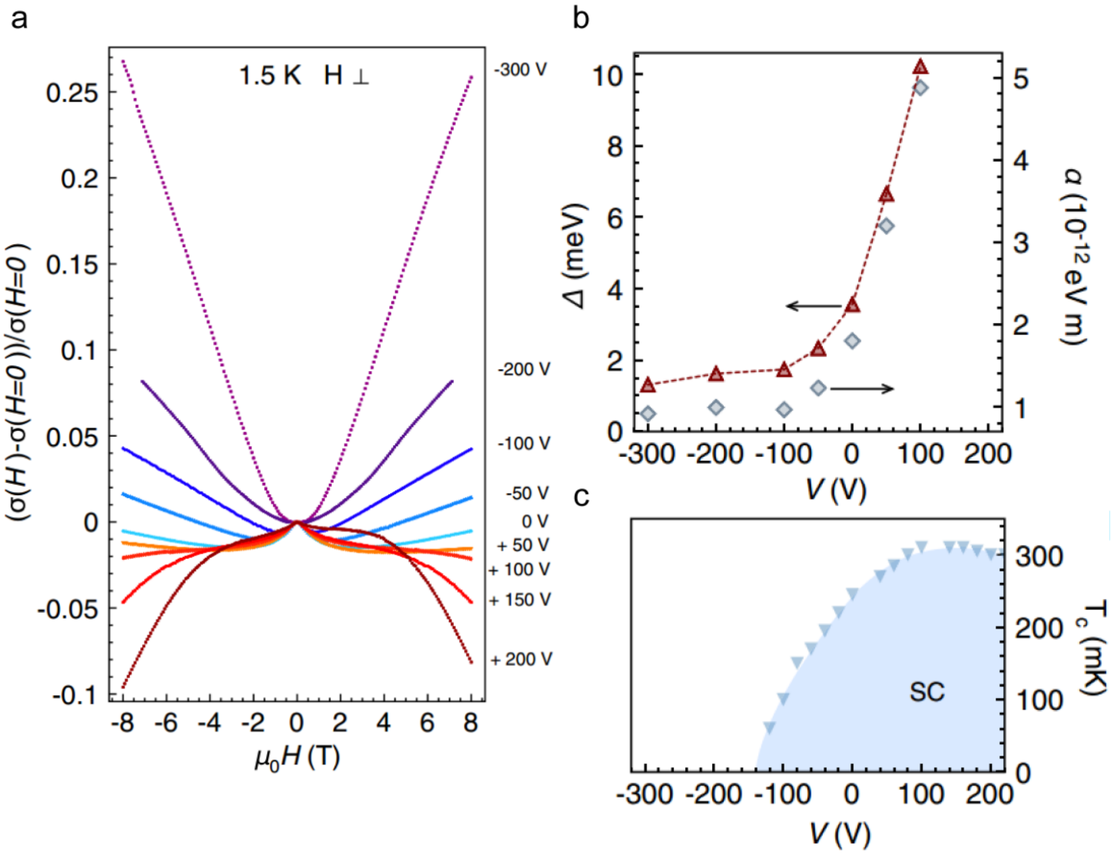

Figure 1.7 Gate tunable spin-orbit coupling at LAO/STO. a, Magnetoconductance at different back gate voltages. **b,** field effect modulation of the Rashba spin splitting energy *Δ* and coupling constant *α*. **c,** Superconducting critical temperature T_c as a function of gate voltage for the same sample. Adapted from Ref. [55].

1.3.6 Piezoresponse

Neither LAO nor STO is known as piezoelectric material but a switchable piezoelectric response is reported in LAO/STO interface via piezoresponse force microscopy (PFM) [56]. The origin of the piezoresponse can be related to carrier-mediated lattice distortions at LAO/STO interface [67,68], and the PFM imaging can map out the interfacial carrier density [69]. Since the electrical response of LAO/STO interfaces is connected to the mechanical conditions, mechanical control (voltage free) of the interfacial conductance can be realized [70]. Oxygen vacancy motions [56,71] and surface adsorbates [72] also affect the piezoresponse. Chapter 3 describes my research project of PFM study at LAO/STO.

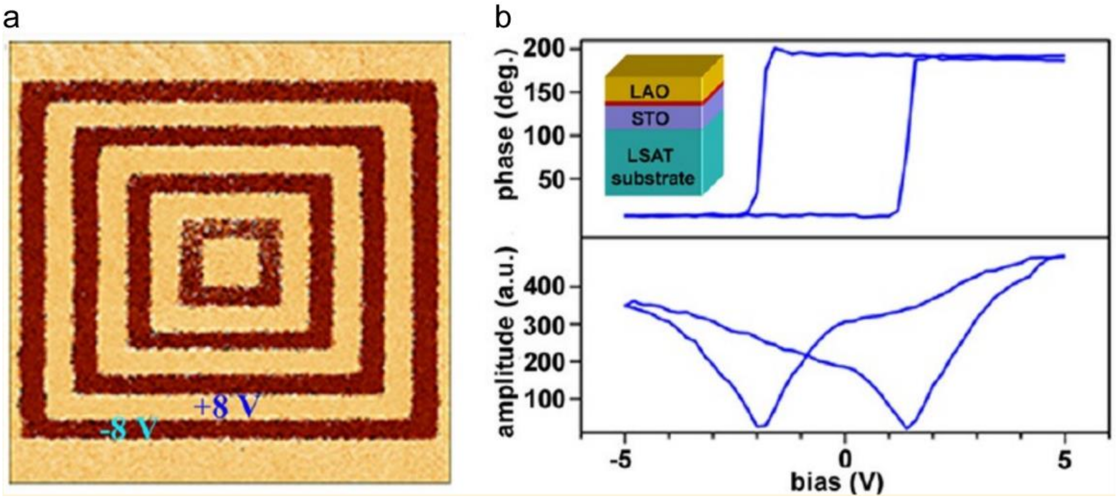

Figure 1.8 Piezoresponse at LAO/STO. a, PFM amplitude images of the frames after poling with ± 8 V. **b,** PFM phase and amplitude hysteresis loops. Adapted from Ref. [56].

1.4 GROWTH OF LAO/STO HETEROINTERFACES

Advances in material growth techniques, including pulsed laser deposition (PLD) [73] and molecular beam epitaxy (MBE) [74], make atomically sharp heterointerfaces available. In 2004, Ohtomo and Huang first successfully synthesized the conducting LAO/STO heterointerfaces using PLD [30]. Afterwards the PLD growth method is optimized and to grow high quality LAO/STO heterostructures. LAO/STO have also been successfully grown by MBE [75], sputtering [5] and atomic layer deposition (ALD) [76]. Besides the regular (001) LAO/STO, the conducting interface can form at (111) LAO/STO [31], (110) LAO/STO [32,33] and even amorphous LAO/STO [33] produced by PLD above a critical LAO layer thickness. The amorphous LAO/STO can also be grown by ALD [34].

The growing processes can significantly affect the properties of LAO/STO interface. Several important factors are: (1) STO termination. For (001) LAO/STO, only growing LAO thin films on the TiO_2-terminated STO substrate produces a conducting interface [30]. A chemical etching method using buffered hydrofluoric acid (BHF) is routinely applied to STO substrates to obtain the TiO_2-termination [77,78] before growing the top LAO thin films. (2) Growth conditions, including temperature, oxygen pressure during growth and post-growth thermal annealing. For PLD growth, the typical growth temperature window is 500 ℃ to 800 ℃ and oxygen pressure window is 10^{-5} to 10^{-3} mbar. In this thsis, two recipes with optimized combination of the growth parameters are used to produce high quality LAO/STO interface with minimum defects, e.g. oxygen vacancies. One is named as the Augsburg recipe since it was established by Dr. Jochen Manhart’s group at the University of Augsburg. The Augsburg recipe uses growth temperature ~ 780 ℃ , oxygen pressure $P_{O_2}{\sim}10^{-5}$ mbar and post-growth thermal annealing at 600 ℃, oxygen sufficient atmosphere (P_{O_2}~ 300 mbar) for 1 hour. The other recipe is tested out by Dr. Chang-Beom Eom’s group at the University of Wisconsin-Madison, which uses growth temperature ~ 550 ℃ , $P_{O_2}{\sim}10^{-3}$ mbar and no post-growth annealing. Most of the LAO/STO samples discussed in this thesis are grown by PLD in Dr. Chang-Beom Eom’s group. Samples grown by other recipes will be noticed. (3) Epitaxial strain. Growing LAO/STO interface on different substrates with various lattice mismatch can modulate the epitaxial strain at the interface and mediate the interface properties [79]. Tensile strain makes the interface insulating, while compressive strain makes the interface metallic, allowing critical thickness and interfacial conductivity modulation. (4) LAO stoichiometry. Controversial results were reported about the stoichiometry dependence. Some group claims that Al-rich LAO layer helps to make a conducting interface, while La-rich LAO may lead to an insulating interface [80]. Other group states that off-stoichiometry LAO layer reduce the carrier density by 2 orders [81]. Besides these listed four factors, other growth details may also affect the LAO/STO properties, for example, the plasma plume in PLD growth [82].

The standard sample growth steps are summarized as following. Before the PLD, low miscut (< 0.10 °) single crystal STO (001) substrates were etched by buffered hydrofluoric (BHF) acid for 60 seconds to obtain TiO_2 terminated surface. Then, the substrates were annealed in a tube furnace at 1000 ℃ for several hours to form an atomically smooth surface with single unit cell height steps. During the PLD growth, a KrF exciter laser (λ = 248 nm, energy density ~ 2.0-2.5 J/cm^2, pulsed at 3 - 5 Hz.) beam is focused on a stoichiometric LAO single crystal target. The laser pulse ablates the LAO target and the plume of ejected material is deposited onto the STO substrates. *In-situ* reflection high-energy electron diffraction (RHEED) is used to monitor the LAO thickness during the growth (Fig. 1.10b), which enables the precise control of layer-by-layer growth. After the PLD, the samples were slowly cooled down to room temperature at high pressure oxygen environment (> 1000 mbar). The high quality LAO/STO interface is verified by high resolution transmission electron microscopy (TEM) images (Fig. 1.10c). Terraces-like surface patterns (Fig. 1.10d) imaged by AFM also indicate good layer-by-layer LAO growth on STO substrates.

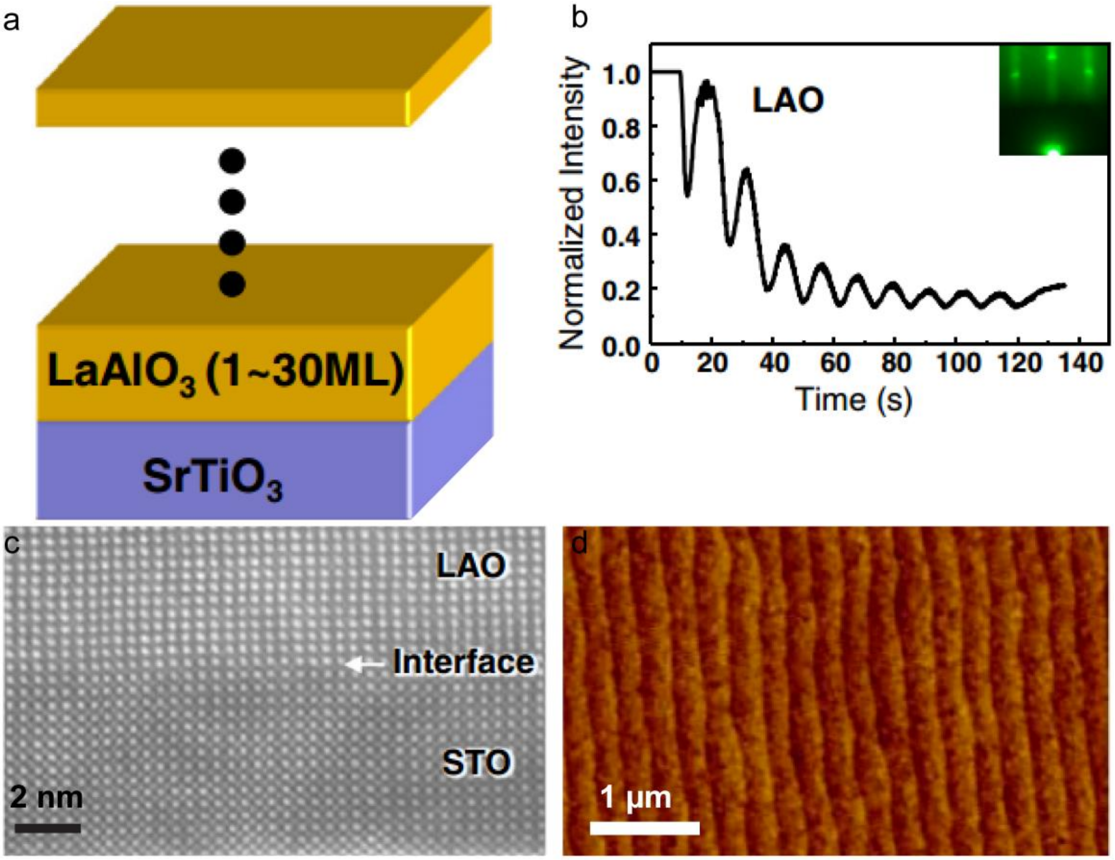

Figure 1.9 PLD growth of LAO/STO. a, schematic diagram of grown structures. **b,** RHEED intensity oscillations. **c,** High-resolution TEM image of LAO/STO. **d,** AFM images of LAO/STO surface. Adapted from Ref. [79].

1.5 POSSIBLE ORIGINS OF CONDUCTING LAO/STO INTERFACE

Although it is more than ten years since the first report of LAO/STO conducting interface, the origin of the interfacial conductance is still under debate. Several mechanisms were proposed and experimentally demonstrated to play roles in the formation of the conducing interfaces.

1.5.1 Polar catastrophe

The polar catastrophe scenario describes an intrinsic electron reconstruction process at LAO/STO. The STO substrate is non-polar material with $Ti^{4+}O_2^{2-}$ and $Sr^{2+}O^{2-}$ planes that are both charge neutral (Fig. 1.11a). LAO is polar material with $La^{3+}O^{2-}$and $Al^{3+}O_2^{2-}$planes that have net charge +*e* and -*e* respectively. When LAO is grown on STO, there is a polar discontinuity across the interface, leading to a built-in electric potential which diverges with increasing LAO thickness. When the LAO thickness reaches a critical value, an electronic reconstruction is proposed to occur in which electrons transfer from the LAO surface to the interface (Fig. 1.11b), thus screening the built-in polarization. This charge transfer naturally results in the formation of a conducting 2D layer near the interface. The polar catastrophe scenario is reminiscent of field-effect gating, in which the field is generated by the LAO layers and compensated by further charge transfer from the surface to the interface.

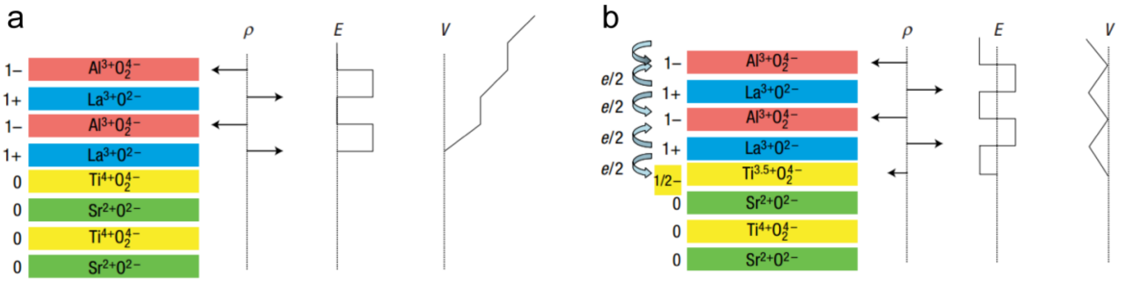

Figure 1.10 Polar catastrophe illustrated for LAO/STO. a, The unreconstructed LAO/STO interface. **b,** The reconstructed LAO/STO interface. The divergence catastrophe at the AlO2/LaO/TiO2 interface can be avoided if half an electron is added to the last Ti layer. Adapted from Ref. [83].

The fact that the observed critical thickness for conductivity in (001) LAO/STO is universal across many labs throughout the world strongly supports the polar catastrophe scenario. Density function theory (DFT) calculation also predicts the electronic reconstruction above the critical LAO layer thickness [36,84]. The polar catastrophe scenario also suggests that a hole gas should form at the LAO surface from the vacancies created by the electrons transferred to the interface, however, evidence of this hole gas has not been seen experimentally so far. Furthermore, there is no polar discontinuity across the interface of (110) LAO/STO and amorphous LAO/STO, but conducting interface still emerges at (110) LAO/STO [31,32] and amorphous LAO/STO [33,34] above a critical LAO thickness. The polar catastrophe scenario alone cannot completely explain the formation of conducting LAO/STO interface and there must be other factors. It is possible that other mechanisms outlined below are also sensitive to the local polarization fields that may lead to very similar critical thickness dependence.

1.5.2 Oxygen vacancy

Many experiments showed that the electrical properties of LAO/STO interfaces is highly sensitive to the oxygen partial pressure during the growth and the post annealing process [85-87], suggesting that oxygen vacancies can serve as donors, providing electrons to form the conducting interface. DFT calculations is also applied to investigate the mechanism of oxygen vacancy formation and the related conducting interface properties [88,89]. In these theory calculations, oxygen vacancy formation is considered to be coupled with the charge transfer and atomic relaxation. A systematic study [90] of sample growth across the parameter space in which oxygen vacancy formation and/or polar catastrophe are expected to be relevant indeed demonstrated how different mechanisms can coexist. Recent study of magnetism in LAO/STO shows there is also a strong relation between the magnetic properties and oxygen vacancies [63,64,91].

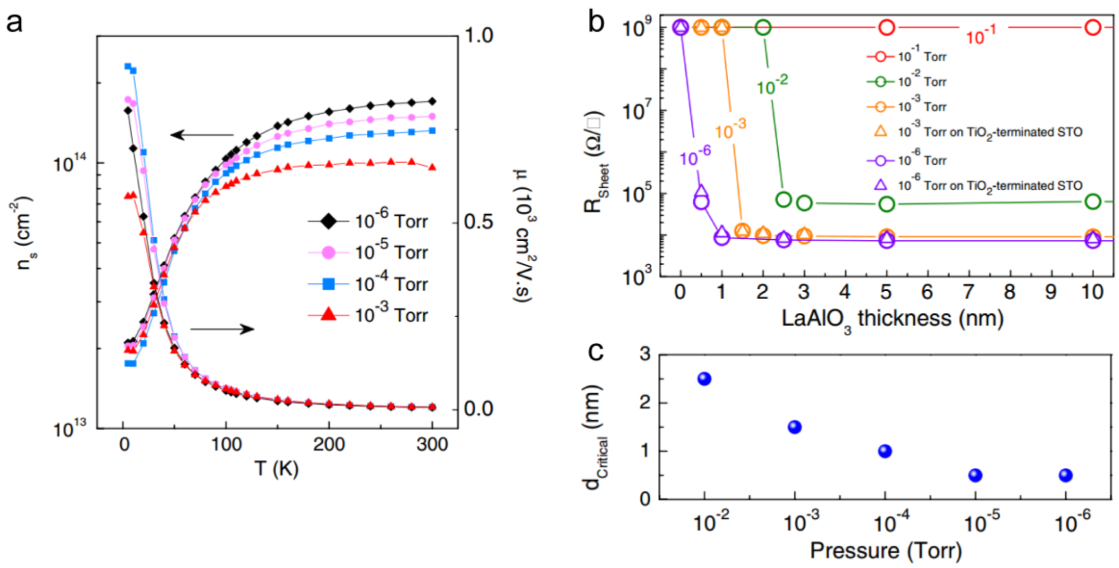

Figure 1.11 Effects of oxygen vacancies on amorphous LAO/STO. a, Electrical transport properties of amorphous LAO/STO heterostructures. **b,** Critical thickness for appearance of conductivity in amorphous LAO/STO heterostructures. **c,** Critical thickness as a function of deposition oxygen pressure. Adapted from Ref. [90].

1.5.3 Cation intermixing and stoichiometry

Another defects related mechanism is cation intermixing across the interface in which atoms of different valence are exchanged. TEM [83] and XRD [92] studies showed that the interface is not always atomically sharp (Fig. 1.13), hinting the existent of cation intermixing. The exchange of La/Sr at the interface may result in local doping and the formation of conducting layer La$_{1\text{-}x}$Sr$_x$TiO$_3$ [92]. X-ray photoelectron spectroscopy (XPS) studies on epitaxial La$_{1\text{-}x}$AL$_{1+x}$O$_3$/STO heterostructures [93] revealed extended diffusion of La and Al into the STO. The stoichiometry in the LAO layer can also tune the interfacial conductance [80,81]. By replacing pure LAO with ultrathin films of LAO diluted with STO ((LAO)$_x$(STO)$_{1-x}$ or LASTO:x), the critical thickness of forming conducing LASTO:x/STO interface is measured to be tunable by the x value. The stoichiometry control is generally related to the polar catastrophe model via mediating the strength of the built-in electric field in LAO.

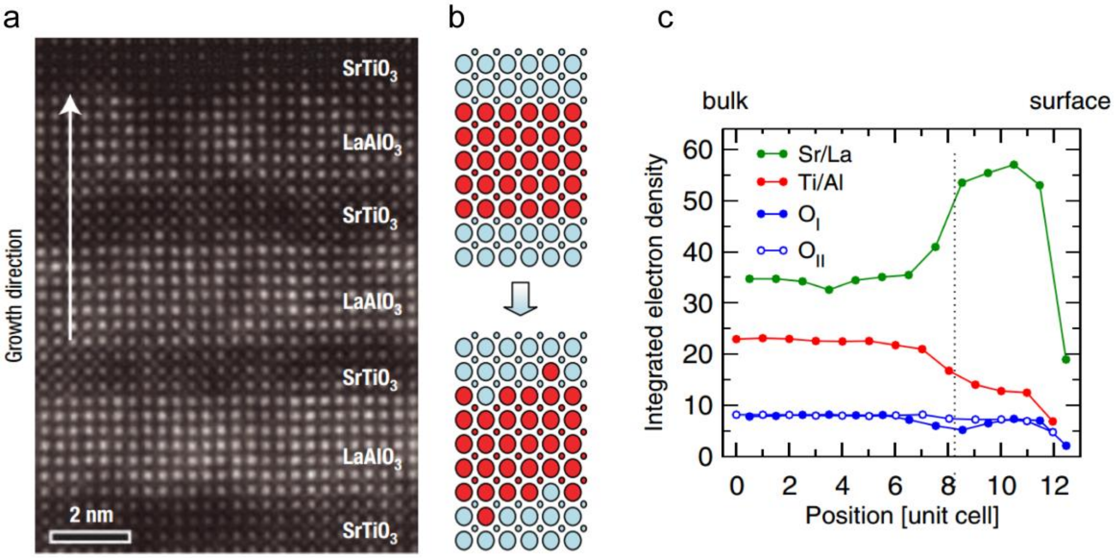

Figure 1.12 Cation intermixing at LAO/STO interface. a, TEM images of n-type LAO/STO interface, showing cations intermixing **b,** A schematic of the cation intermixing observed in **a.** The large blue circles are Sr, small blue for Ti, large red for La and small red for Al. **a** and **b** are adapted from Ref. [83]. **c,** integrated electron densities calculated from XRD data on LAO/STO. Adapted from Ref. [92].

1.5.4 Surface chemistry

The LAO/STO surface potential can significantly affect the interface conductivity. Immersion LAO/STO surface in solvents could alter the 2DEL mobility [94]. DFT calculations demonstrated how a surface metal layer can tune the 2DEL [95]. Experimentally researchers used metallic nanoparticles, e.g. Pd [96] or Au [97] on LAO/STO surface to enhance photo response, or other oxide layers, e.g. PZT [98] or $SrCuO_2$ [99] to tune electrical properties of the 2DEL. Theoretical studies have stressed the importance of surface chemistry by linking 2DEL formation to chemical phenomena including the protonation of oxygen, the generation of oxygen vacancies, and adsorption of water [100-102] at LAO surface. Recently my research project of the surface effect, collaborated with Dr. Keith Brown, demonstrated that a surface protonation procedure can induce a larger than 4 order of magnitude interfacial conductance switch [103]. The nominally conducting interface of 4 uc LAO/STO can be driven into an insulating state by rinsing into water and exposure to UV light restore the conductance. This effect persist for 5 uc and 6 uc LAO/STO samples and disappear at or above 7 uc. Chapter 6 describes more of this research project.

1.5.5 Summary

In a brief summary, four scenarios of the 2DEL formation at LAO/STO heterointerface are introduced above. These scenarios (including polar catastrophe, oxygen vacancies, cation intermixing and surface chemistry) are not mutually exclusive or isolated from each other. Under generic growth conditions, multiple mechanisms may be at play simultaneously.

2.0 EXPERIMENTAL METHOD

Chapter 2 introduces the main experimental methods in my research, including device fabrication in the cleanroom, standard AFM operation modes—contact modes and AC modes, as well as PFM, MFM and c-AFM lithography, transport measurements in dilution refrigerators (DR).

2.1 DEVICE FABRICATION

The primary goal of the device fabrication is to make electrical contact to the LAO/STO interface and allow us electrically access the interface. To fulfill various experiment purposes, different electrical contact patterns are designed and fabricated using photolithography, Ar+ ion etching and sputtering deposition (or e-beam evaporation). Ultrasonic washing in acetone and isopropyl alcohol (IPA), as well as oxygen plasma cleaning are applied to samples to obtain a clean LAO/STO surface. Generally, our device fabrication process needs to make two layers of electrodes. First layer consists of electrodes which are contacting the interface, and the second layer consists of larger metal pads (for wire bonding) with metal paths connected to the first layer (interface contacting electrodes). In the end, we connect the pads in the chip and the pads on the sample by wire bonding.

2.1.1 Sample processing overview

The fabrication process starts with spin-coating photoresist (AZ P4210) uniformly (4000 rpm for 30 seconds, ~2 μm thickness) on the LAO/STO surface, followed with soft baking at 95 ℃ for 1 minute (Fig. 2.1a). Then the sample covered with photoresist is exposed to UV (λ = 365 nm) light under a predesigned mask using a mask alignment system (Fig. 2.1b). The UV light is selectively allowed to pass through the mask, therefore the photoresist is selectively exposed. After UV exposure, the sample is soaked in developer (AZ 400K) solvent to dissolve the UV light exposed photoresist so that the photoresist is patterned (Fig. 2.1d). This whole process described in this paragraph is called photolithography.

The next step after the photolithography is to make electrodes which are contacting the LAO/STO interface. Samples with patterned photoresist are loaded into an Ar+ milling system. In areas with photoresist the LAO layer is protected from the ion beam, while in areas without photoresist the LAO layer is etched away (Fig. 2.1c). After ion milling, metals are deposited via sputtering. Usually Ti is first deposited as an adhesive layer (~ 4 nm) followed with Au (~ 25 nm) to fulfill the etched trench (Fig. 2.1e). Ohmic contact to the LAO/STO interface is achieved for the Ti/Au electrodes. Samples after sputtering deposition go to the liftoff process—samples are first immersed in a photoresist stripper or in acetone for several hours then ultrasonically washed in acetone for 2 minutes. The photoresist is dissolved and the metal rests on photoresist is washed away, leaving only the patterned electrodes (Fig. 2.1g). The samples are ultrasonically washed again isopropyl alcohol (IPA) for 2 minutes to dissolve the acetone and then blown dry using a N_2 stream.

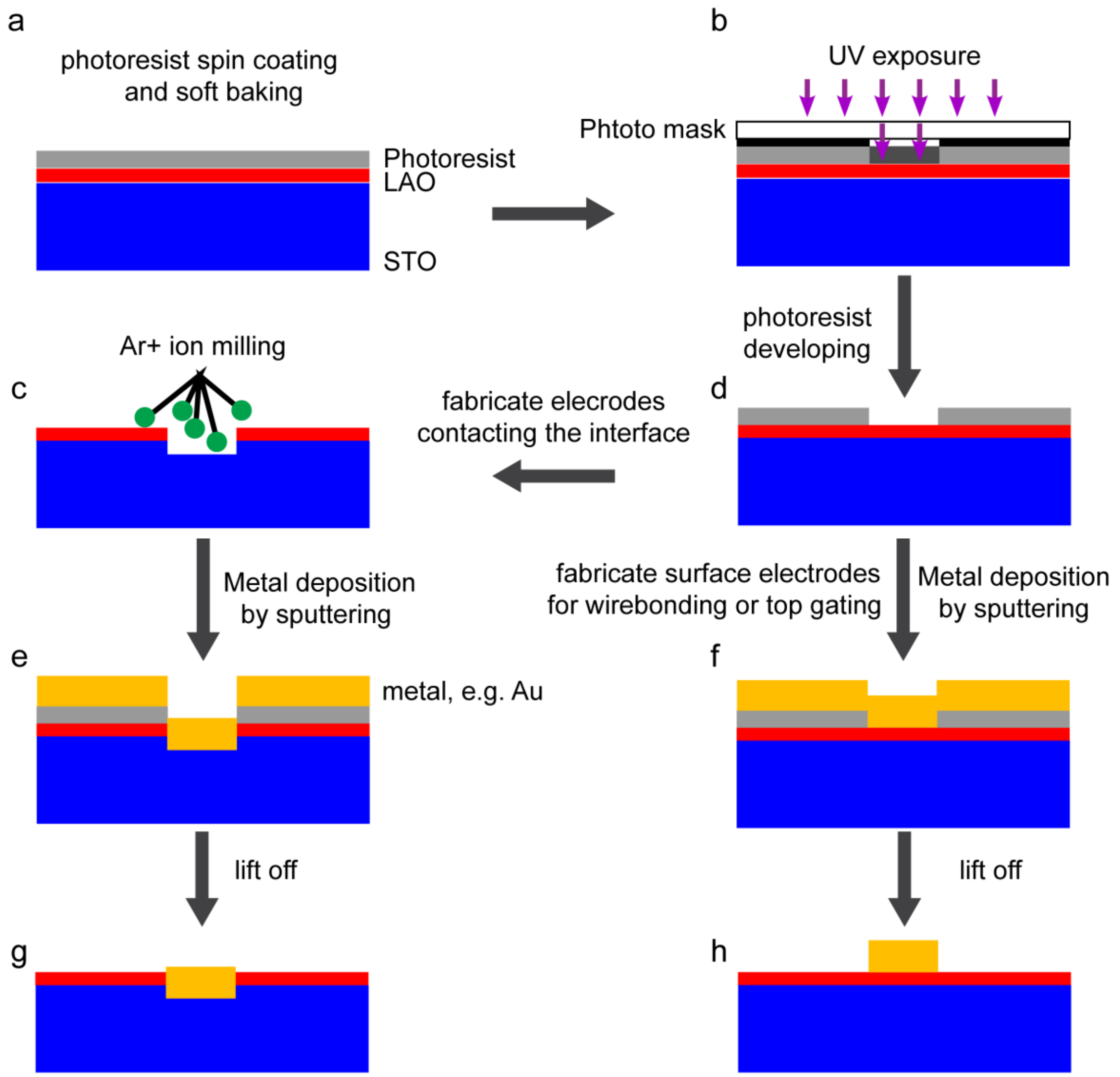

Figure 2.1 Schematic of fabricating electrodes to LAO/STO samples. a, photoresist spin coating and soft baking. **b,** UV exposure under a predesigned mask. **c,** develop the exposure photoresist. **d,** Ar+ ion mill to etch away the LAO layer for fabricate electrodes contacting the interface. **e,** metal electrodes (usually Ti/Au) deposition via sputtering, which fills the trench created in the Ar+ milling step. **f,** Surface electrodes for wire bonding or top gating is also deposited by sputtering. **g, h** lift off process, leaving the metal patterns as electrodes at LAO/STO for following experiments.

Similar processing steps are applied to make the 2nd layer of electrodes (the wire bonding pads). First the photoresist is spin coated on LAO/STO surface. After the photolithography process, no Ar+ ion milling is needed now since the wire bonding pads are on LAO/STO surface.

An oxygen plasma cleaning step (1 Torr, 100 W, 20 s) is performed to remove possible photoresist residue on the photoresist-dissolved LAO surface. The following sputtering uses Ti adhesive layer (~ 4 nm) plus thick Au layer (~ 50 nm) for wire bonding (Fig. 2.1f). Liftoff process goes after the sputtering (Fig. 2.1g) and an oxygen plasma cleaning is performed (1 Torr, 100 W, 20 s) again to remove possible photoresist residue on LAO/STO surface.

2.1.2 Device overview

The as-received samples from our collaborators have a typical size of 5 mm by 5 mm (Fig. 2.2a), the thickness is either 1 mm or 0.5 mm. After our processing, the samples surface is almost fully covered with Ti/Au patterns (Fig. 2.2b). To obtain electrical access to the sample, the LAO/STO sample is glued to a chip and gold wires are used to make electrical connections by a wire bonding machine (Fig 2.2 c). The most commonly used device geometry is called a “canvas” (Fig. 2.2d), where 16 electrodes contact the LAO/STO interface and define one 30 μm × 30 μm area. The AFM image of one canvas (Fig. 2.2e) shows two layers of electrodes (Fig. 2.2f) as mentioned in the sample processing overview.

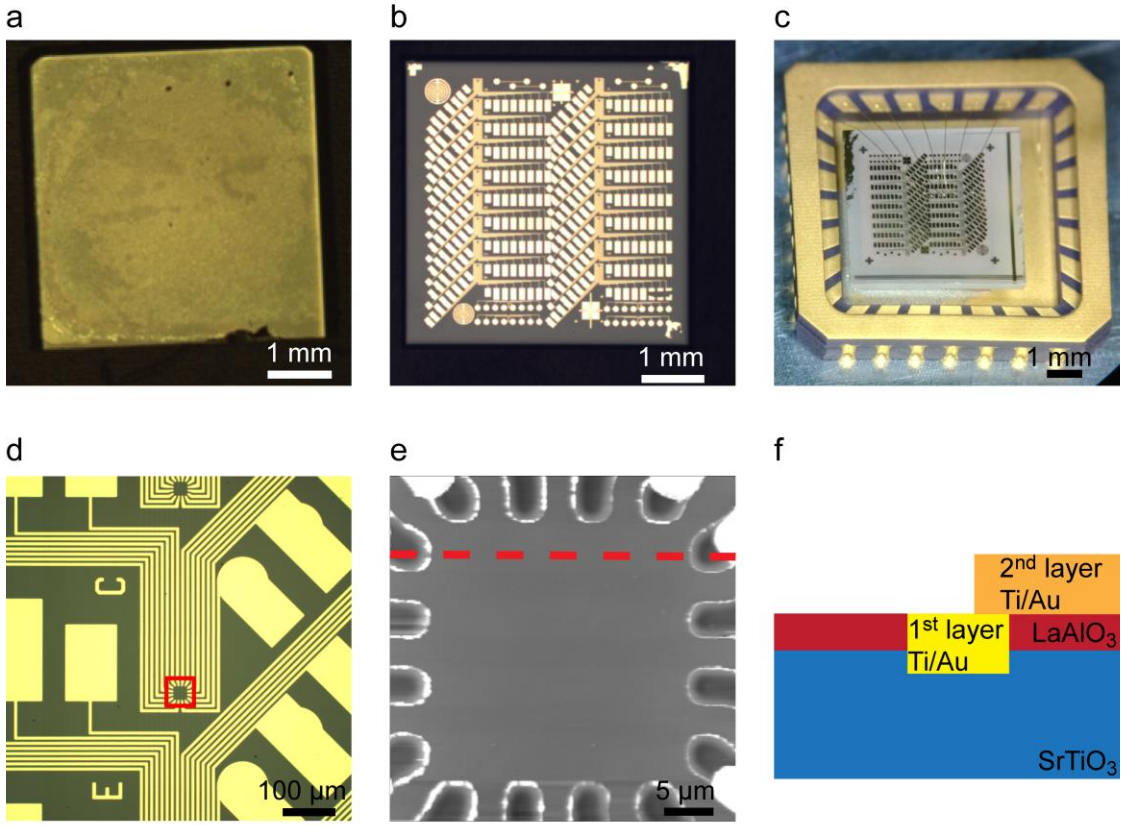

Figure 2.2 LAO/STO sample images. a, as-received sample from our collaborators. **b,** sample after electrodes patterning. **c,** sample after wire bonding and loading into a chip. **d,** close-up optical images of one canvas **e,** AFM images of the canvas which is marked in a red rectangular in **d**. **f,** schematic of the two layers of Ti/Au electrodes, which can be verified from the profile of the red dash line in **e**.

The 30 μm × 30 μm "canvas" device is largely used for c-AFM lithograph and followed transport or optical experiments. There are experiments that need modified device geometry and some experiments also require modify the sample processing procedure. For example, For the MFM experiments we used the round-disk geometry for top gates (Fig. 2.2a), and to suppress the leakage current from the top gate to the LAO/STO interface, only Au is used without the Ti adhesion layer as the top gate metal. For the graphene experiments we want to independently gate the LAO/STO interface and the graphene layer, so we modified the "canvas" structure to be half of the 16 electrodes contacting the interface and the other half only contacting the surface (Fig.

2.2b). Another example is LAO/STO samples that are covered with *in-situ* Au top layers. We first used photolithography and chemical etch to pattern the *in-situ* Au layer to be the designed top gate geometry. Then the regular sample processing procedure follows to make other electrical contact patterns. The remaining *in-situ* Au serves as top gates for tunneling and SET experiments (Fig. 2.2c) with better quality than the *ex-situ* deposited Au top gate. The adhesion between Au and LAO surface is not very strong without the Ti adhesion layer, so in the liftoff and cleaning steps, the power and time of ultrasonic washing is largely reduced. In a word, we modify the device geometry and processing steps to fulfill our specific experiment requirements.

2.2 ATOMIC FORCE MICROSCOPY

Atomic force microscopy (AFM) is one type of scanning probe microscopy (SPM) with demonstrated resolution on the order of fractions of a nanometer (atomic resolution) [104,105]. The first AFM was invented by Binnig, Quate and Gerber in 1986 [106], and since then numerous remarkable progress and breakthrough has been made to improve the performance and expand the applicability.

Nowadays AFM has been an invaluable asset in the surface scientist’s toolbox due to its unique advantages. (1) Most AFM modes can work perfectly well in ambient air or liquid environment which enables AFM to study biological macromolecules and even living organism. While an electron microscopy, such as scanning electron microscopy (SEM) or transmission electron microscopy (TEM), needs an expensive vacuum environment for proper operation. (2) Samples viewed by AFM do not require any special treatments (such as metal/carbon coatings) that can irreversibly change or damage the sample, and does not typically suffer from charging artifacts in the final image. While SEM, TEM or scanning tunneling microscopy (STM) requires the sample to be conductive or treated to be conductive. (3) AFM provides a three-dimensional surface profile, unlike electron microscopies, which provide a two-dimensional projection or a two-dimensional image of a sample. (4) AFM can provide higher resolution than SEM and comparable resolution to STM and TEM. True atomic resolution using AFM has been demonstrated under ultra-high vacuum (UHV) and in liquid environments [105]. (5) AFM can be combined with a variety of optical microscopy techniques such as fluorescent microscopy, further expanding its applicability. Combined AFM-optical instruments have been applied primarily in the biological sciences but have also found a niche in some materials applications, especially those involving photovoltaics research [107].

There are also limitations of AFM. (1) AFM can only image a maximum height on the order of 10-20 micrometers and a maximum scanning area of about 150×150 micrometers. SEM can image an area on the order of square millimeters with a depth of field on the order of millimeters. (2) AFM requires several minutes for a typical scan while a SEM is capable of scanning at near real-time, although at relatively low quality. The relatively slow rate of scanning during AFM imaging often leads to thermal drift in the image making the AFM less suited for measuring accurate distances between topographical features on the image. Ultra-fast scanning (> 100 Hz/line [108]) and multi-probe technique (> 10 million tips [109]) are also developed to increase the throughput of AFM, giving it wider applications in industry.(3) Due to the nature of AFM probes, they cannot normally measure steep walls or overhangs. Specially made cantilevers and AFMs can be used to modulate the probe sideways as well as up and down (as with dynamic contact and non-contact modes) to measure sidewalls, at the cost of more expensive cantilevers, lower lateral resolution and additional artifacts. (4) As with any other imaging technique, there is the possibility of artifacts in AFM images, which could be induced by an unsuitable tip, a poor operating environment, or even by the sample itself. These image artifacts are unavoidable but can be reduced through various methods.

2.2.1 AFM working principle

The AFM consists of a cantilever with a very sharp tip (the radius of curvature is on the order of nanometers) over a sample surface (Fig. 2.3). When the tip is brought into proximity of a sample surface, forces between the tip and the sample will cause a deflection of the cantilever. To measure the cantilever deflections, the most popular way is using an optic level system. By reflecting an incident laser beam off the flat top of the cantilever, any cantilever deflection will cause slight changes in the direction of the reflected beam. A position-sensitive photo diode (PSPD) can be used to track these changes. Thus, if an AFM tip passes over a raised or lowered surface feature, the resulting cantilever deflection is recorded by the PSPD and converted to topography information. The tip or sample can move in the x, y and z directions (usually using piezeoelectronics). During scanning in the x-y directions, a feedback loop is used to control the height of the tip above the surface—thus maintaining constant force between the tip and the sample. The topography information is recorded and plotted out versus the x, y coordination during the AFM scanning.

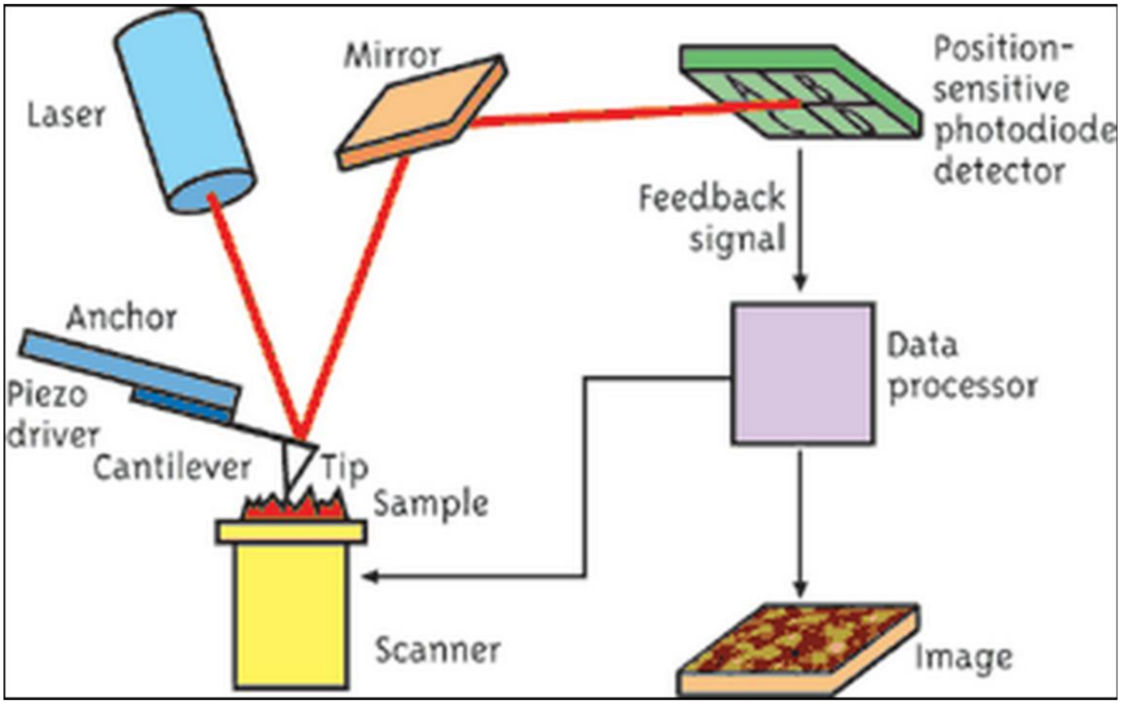

Figure 2.3 Schematic diagram of atomic force microscopy (AFM). AFM consists of a cantilever, a laser beam, a position-sensitive photodiode detector (PSPD), a data processing system (controllers, computers and AFM software), feedback loop and a scanner (usually using piezoelectronics). Adapted from Ref. [110].

Depending on the properties of tip, sample, and tip-sample interaction, many kinds of forces paly roles in AFM scan, including mechanical contact force, van der Waals forces, capillary forces, chemical bonding, electrostatic forces, magnetic forces, Casimir forces, and solvation forces etc. Generally, as the tip approaches the surface, the attractive force between the surface and the tip causes the cantilever to deflect towards the surface (Fig. 2.4). However, as the cantilever is brought even closer to the surface, such that the tip makes contact with it, increasingly repulsive force takes over and causes the cantilever to deflect away from the surface. When the cantilever is far away from the surface, the AFM is operating in the so-called non-contact (NC) mode (or dynamic mode). Initially the NC mode includes both the amplitude modulation (AM) mode and frequency modulation (FM) mode. The AM mode was later used very successfully at a closer distance range in ambient conditions involving repulsive tip-sample interactions [111]. Now AM mode is also called as tapping mode, AC mode or vibrating mode. When the tip is contacting the sample surface, the AFM is operating in the contact mode (or static mode). Contact mode and AC mode will be introduced in the following sections since they are routinely used in our research activities.

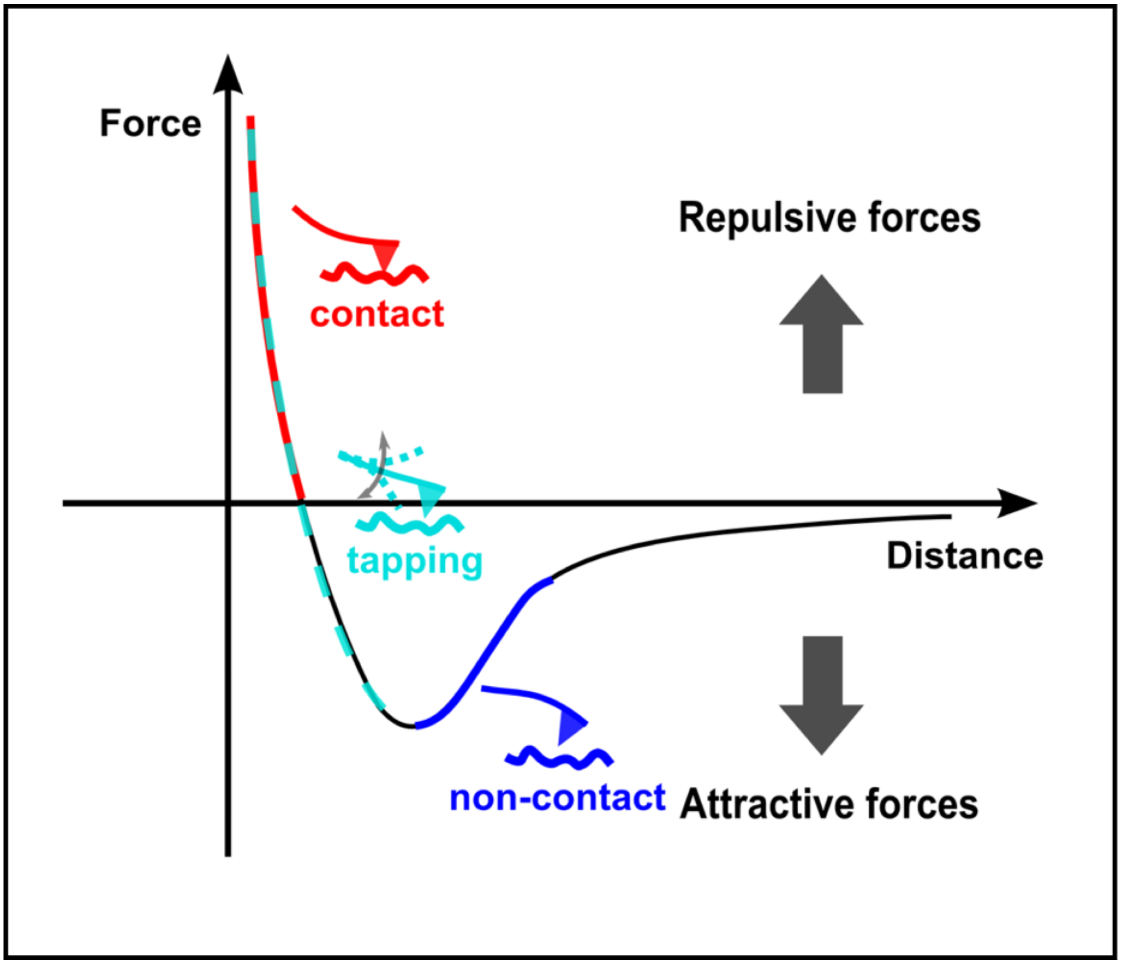

Figure 2.4 Force curve in AFM. Illustration of the force curve versus tip-sample distance and related AFM operation modes: non-contact, tapping and contact modes. Adapted from http://www.teachnano.com/education/AFM.html.

2.2.2 Contact mode

In contact mode, the tip directly contacts the sample surface, where the overall force between tip and sample is repulsive. Low stiffness cantilevers (i.e. cantilevers with a low spring constant *k*) is preferred to use in contact mode because the measurement of a static signal is prone to noise and drift. When tip approaches samples surface, attractive forces can be quite strong, causing the tip to "snap-in" to the surface. Thus, contact mode AFM is almost always done at a depth where the overall force is repulsive, that is, in firm "contact" with the solid surface below any adsorbed layers.

When the tip engages on a sample surface, the tip deflects and exerts a force (*F*) to the sample, which can be expressed by $F = - k \bullet \mathrm{D}$. *k* is the cantilever's spring constant and *D* is the distance of tip deflection. During the contact mode scan, the topography of the surface is measured either using the deflection of the cantilever directly or, more commonly, using the feedback signal required to keep the cantilever at a constant force (or a constant deflection). In the latter case, the deflection signal *D* from the photodiodes serves as the error signal in the feedback loop. The feedback output signal controls the piezo movements in the z direction and maps out the surface topography spatially during the scan.

2.2.3 AC mode (tapping mode)

AC mode (or tapping mode) is another commonly used AFM scanning mode. In ambient conditions, most samples develop a liquid meniscus layer. Because of this, keeping the probe tip close enough to the sample for short-range forces to become detectable while preventing the tip from sticking to the surface presents a major problem for non-contact dynamic mode in ambient conditions. AC mode (also called intermittent contact, dynamic contact mode or tapping mode) was developed to bypass this problem [111].

In contact mode, the AFM cantilever is static. However, in AC mode, the cantilever is dynamic, where a shake piezo is used to mechanically drive the cantilever to oscillate at or near its resonant frequency ω. The amplitude (A) of this oscillation is typically 100 to 200 nm. The tip strikes against the surface and detaches from the sample surface on each oscillation cycle by using this relatively large vibration amplitude. Depending on the tip-sample distance, the interaction between the tip and sample surface can be repulsive or attractive. When the tip comes closer to the surface, the interaction of forces acting on the cantilever caused the amplitude of the oscillation to decrease. To obtain the surface topography, the feedback circuit is used to maintain the the amplitude signal A constant at the set point by adjusting tip height. The amplitude signal A serves as the error signal in the feedback loop and the feedback output controls the tip height and maps out the sample surface profile. Besides the cantilever's oscillation amplitude (A), the phase (θ) are also measured by the lock-in amplifier during the scan.

2.2.4 Non-contact mode

In non-contact mode, the tip is held above the surface and similar to the AC mode, the tip oscillates at its resonance frequency (frequency modulation) or just above the resonance frequency (amplitude modulation) with a much smaller amplitude (~ a few nanometers). As the tip approaches sample surface, the attractive force between the tip and the sample changes the amplitude, phase and frequency of the cantilever's resonant oscillation. The feedback loop system maintains a constant oscillation amplitude or frequency by adjusting the average tip-to-sample distance. The feedback output signal maps out the tip-to-sample distance spatially and constructs a topographic image of the sample surface via AFM software.

To perform non-contact mode AFM scan in an ambient atmosphere, it is critical to prevent the tip from contacting the sample surface. Once the tip makes accidental contact with the sample, the tip can stick to the sample surface and stop its vibration due to the meniscus force of the liquid layer on the sample surface. Non-contact mode AFM does not suffer from tip or sample degradation effects that can happen after taking numerous scans with contact AFM. This makes non-contact AFM preferable to contact AFM for measuring soft samples, e.g. biological samples and organic thin film. In the case of rigid samples, contact and non-contact images may look the same. However, if a few monolayers of adsorbed fluid are lying on the surface of a rigid sample, the images may look quite different. An AFM operating in contact mode will penetrate the liquid layer to image the underlying surface, whereas in non-contact mode an AFM will oscillate above the adsorbed fluid layer to image both the liquid and surface.

Besides the three basic AFM scan modes listed above for topography imaging, AFM has many other applications, including a variety of force sensing (electric force, magnetic force, Casimir forces, etc.), lithography (local oxidation lithography, dip pen lithography, etc.), nanomanipulation and nanoindentation. In the following sections, piezoresponse force microscopy (PFM) and magnetic force microscopy (MFM) will be introduced.

2.2.5 Piezoresponse force microscopy (PFM)

The piezoelectric effect is understood as the linear electromechanical interaction between the mechanical and the electrical state of piezoelectric materials. When a mechanical force is applied to piezoelectric materials, an internal electric field is generated. The reverse effect can also be observed as an electric field is applied, mechanical deformation occurs, either expansion or contraction. Some piezoelectric materials show spontaneous non-zero net polarization even without mechanical stress and they are called ferroelectric. Piezoresponse force microscopy (PFM) characterizes materials' electromechanical response. Commonly the PFM technique is used to image and manipulate ferroelectric domains.

In PFM mode, a conductive cantilever (e.g. Pt coated tip) scans over the ferroelectric sample surface in contact mode (Fig. 2.5a). In regularly PFM operations, an ac voltage at frequency ω is applied to the tip and the sample is grounded. The ac modulated electric field runs across the ferroelectric material and causes a structure distortion and corresponded cantilever deflection signal oscillating at frequency ω. By using a lock-in amplifier, the amplitude and phase of the cantilever deflection is measured and plot out as PFM images. The PFM amplitude and phase information can be interpolated to understand the piezoelectric strain constant and the spontaneous polarization direction of the scanned sample. For example, depending on the sample's polarization direction, the deformation could oscillates in-phase (0 degree, Fig 2.5 b and c) or out-of-phase (180 degree, Fig 2.5 d and e) with the applied ac excitation.

In our PFM study, instead of applying voltages directly to the tip, we apply electric field to the sample and grounded the tip. More details of our PFM experiments on LAO/STO can be found in Chapter 3.

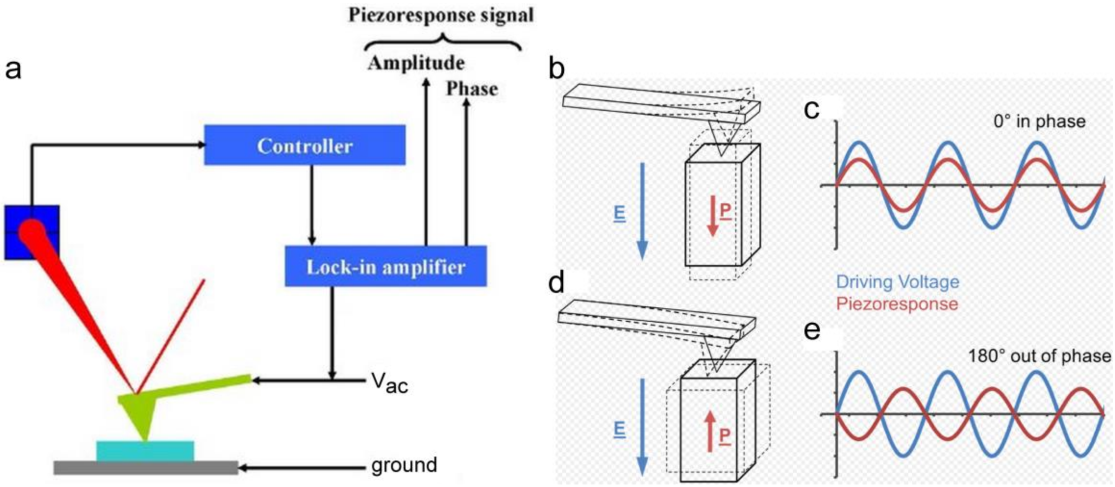

Figure 2.5 Schematic of Piezoresponse force microscope (PFM). a, PFM set-up diagram. **b,** Sample expands when external electric field is parallel to sample's polarization and corresponded **c,** in-phase piezoresponse**. d,** Sample contracts when external electric field is anti-parallel to sample's polarization and corresponded **e,** out-of-phase piezoresponse**.** Adapted from website http://www.azonano.com/article.aspx?ArticleID=2682 and Wikipedia.

2.2.6 Magnetic force microscopy (MFM)

In magnetic force microscopy, a sharp magnetized tip (e.g. CoCr coated tip) scans over a magnetic sample. MFM scanning often uses non-contact AFM (NC-AFM) mode and the tip-sample magnetic interaction, e.g. magnetic dipole–dipole interaction, is detected and used to reconstruct the sample's magnetic structure.

In MFM mode, the cantilever is mechanically driven by a piezoelectric transducer at or near its resonant frequency and scans at a constant height Δh above the sample surface (Fig 2.6). When the tip is brought in proximity to sample surface, the amplitude (A), phase (φ) and frequency (f) of the cantilever's resonant motion are altered. The changes (ΔA, $\Delta\varphi$, Δf) can be directly related to the force gradient $\partial F_z/\partial z$, by the following expressions:

$$\Delta A \approx \frac{2A_0Q}{3\sqrt{3}k}\cdot\frac{\partial F_z}{\partial z} \tag{2-1}$$

$$\Delta\varphi \approx \frac{Q}{k}\cdot\frac{\partial F_z}{\partial z} \tag{2-2}$$

$$\Delta f_0 \approx -\frac{1}{2k}\cdot\frac{\partial F_z}{\partial z}\cdot f_0 \tag{2-3}$$

Therefore the MFM signal can be recorded in three ways: phase detection, which measures the cantilever’s phase of oscillation relative to the piezo drive; amplitude detection, which tracks variations in oscillation amplitude; and frequency modulation, which directly tracks shifts in resonant frequency. In the amplitude and phase detection, the cantilever oscillates at a fixes frequency f0 and the change of amplitude and phase (ΔA, Δφ) are recorded as MFM signal. In the frequency modulation, a 90 ° phase shift between the cantilever drive and response is maintained using a feedback look, then the frequency shift Δf is detected as the MFM signal. Generally, phase detection and frequency modulation produce superior results compared to the amplitude detection. The surface topography can also be monitored in MFM mode as a check of cross talk between magnetic interaction and other forces.

Based on the MFM set-up, applying an *in-situ* modulated electric field (*E*) allows local detection of the *E*-induced magnetic signal and imaging the coupling between the magnetic and electric dipoles in magneto-electric materials [112]. Such detection technique is called magneto-electric force microscopy (MeFM). In our magnetic study of LAO/STO, the MeFM method is employed to explore how the ferromagnetism evolves as a function of carrier density tuned by electric field.

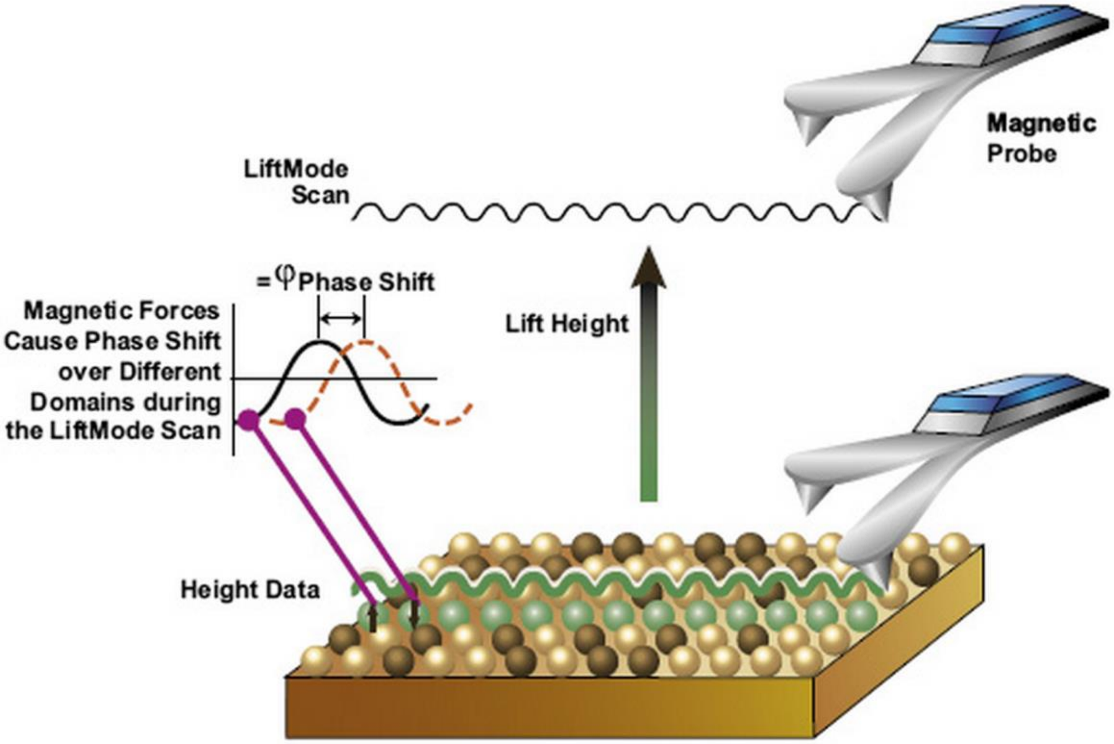

Figure 2.6 Schematic diagram of magnetic force microscopy (MFM). Adapted from website http://blog.brukerafmprobes.com/guide-to-spm-and-afm-modes/magnetic-force-microscopy-mfm/

2.3 C-AFM LITHOGRAPHY ON LAO/STO

As discussed in Section 1.3.1, for LAO/STO with LAO thickness just below 4 uc, the interface can be macroscopically modulated through the metal to insulator transition (MIT) by back gating. Using a biased AFM tip which serves as a nanoscale top gate, the interfacial MIT can also be locally controlled [49]. For 3 uc LAO/STO, a positively biased AFM tip can switch the insulating interface to be conducting. On the other hand, a negatively biased AFM tip can restore the conducting state back to be insulating. The conductive AFM (c-AFM) lithography technique provides a flexible and convenient way to fabricate on-demand nanodevices and nanostructures [57] for potential nanoelectronic applications as well as scientific research purposes.

2.3.1 C-AFM lithography operation

In c-AFM lithography operation, the conductive probe is contacting the LAO/STO surface. For the writing process (Fig. 2.7a), the AFM tip is positively biased, scans from one electrode to another in contact mode. As soon as the tip reaches the second electrode, the conductance between two electrodes shows an abrupt jump (Fig. 2.7b). Same writing process performed between electrodes not contacting the interface does not show any conductance jump, therefore the conducting channel must form at the LAO/STO interface. The created conducting nanostructures can also be erased (Fig. 2.7c). As the negatively biased AFM tip moves vertically across the written nanowire, the conductance between two electrodes drops to zero (Fig. 2.7d). By fitting the drop of conductance curve, the nanowire width can be estimated. Commonly the nanowire width is tens of nanometers. Optimizing the writing parameters can make the nanowire width as small as 2 nm [49].

The conducting nanostructures created by c-AFM lithography at the LAO/STO interface can be directly imaged using PFM [69], The nanowire as well as the junction are clearly visualized in PFM images (Fig. 2.7e and f). The resolution of PFM imaging is limited by tip sharpness and tip-feature convolution [69].

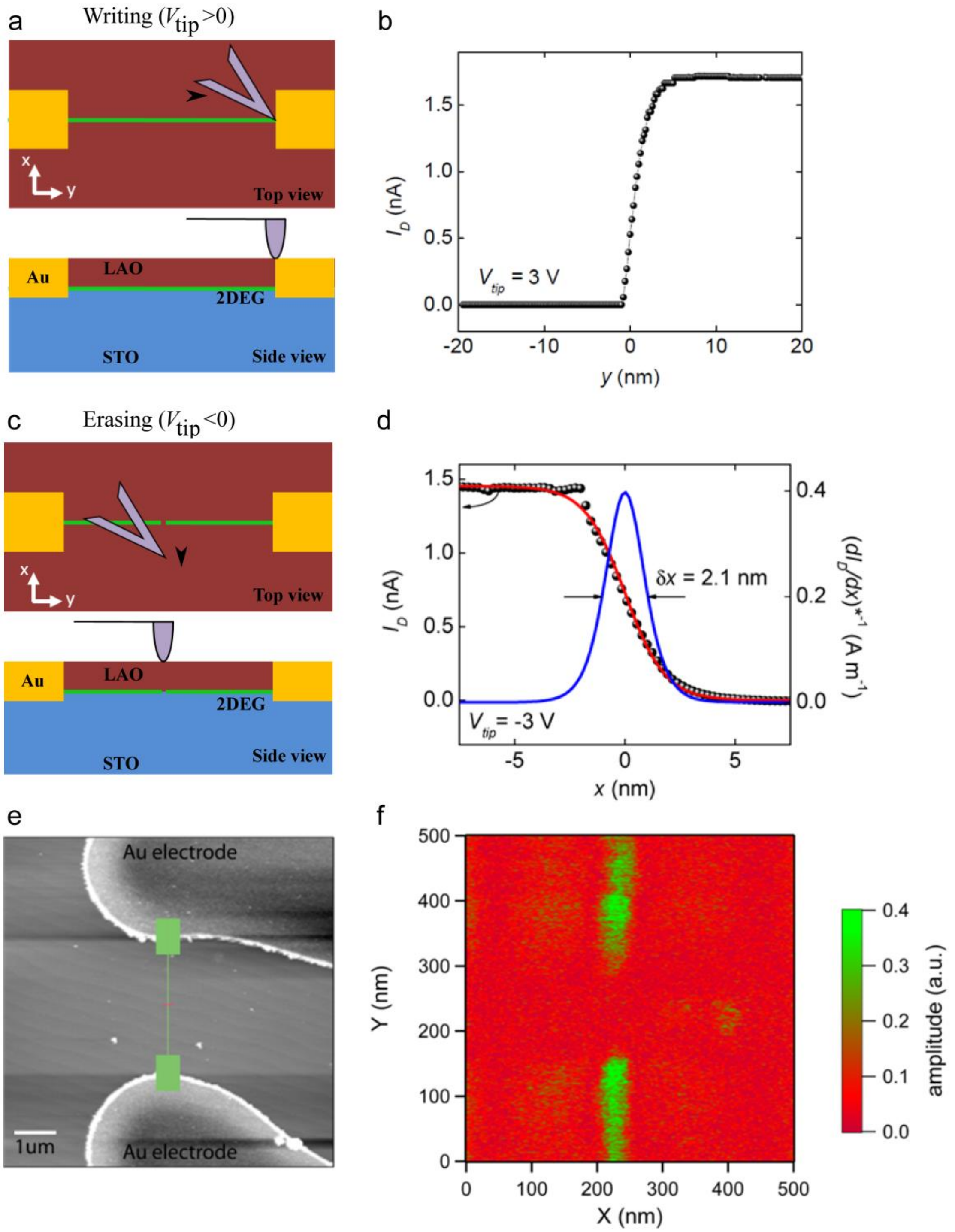

Figure 2.7 Conductive AFM lithography on 3 uc LAO/STO. a, schematic of writing process. **b,** conductance jump during writing. **c,** schematic of erasing process. **d,** conductance drops to zero after erasing. Data can be fit to extract the wire width. **e,** AFM lithography pattern between two Au electrodes and **f,** the corresponded PFM image. Data in **b** and **d** is adapted from Ref. [49]. Image **e** and **f** are adapted from Ref. [69].

2.3.2 “Water cycle” mechanism of c-AFM lithography

The most possible working mechanism of the c-AFM lithography involves a surface protonation process. First principal calculation suggests that H_2O can be adsorbed on LAO surface and dissociates into OH^- and H^+ (Fig. 2.8a) [102,113]. During the writing process, the positively biased AFM tip removes the OH^- adsorbates (Fig. 2.8b), locally charging the LAO surface with an excessive H^+ ions. The charge writing dopes the LAO/STO interface and consequently switches the interface from insulating to conducting. During the erasing process, the negatively biased AFM tip removes H^+ adsorbates (Fig. 2.8c), restoring the OH^-- H^+ balance, and the interface reverts back to an insulating state. The "water cycle" process permits multiple writing and erasing runs without physical modification of the oxide heterostructures. Experiments performed in AFM under vacuum or various gas mixture conditions [114] support this “water cycle” mechanism. The writing process cannot make conducting wires in vacuum chamber or a chamber filled with other gases except water vapor.

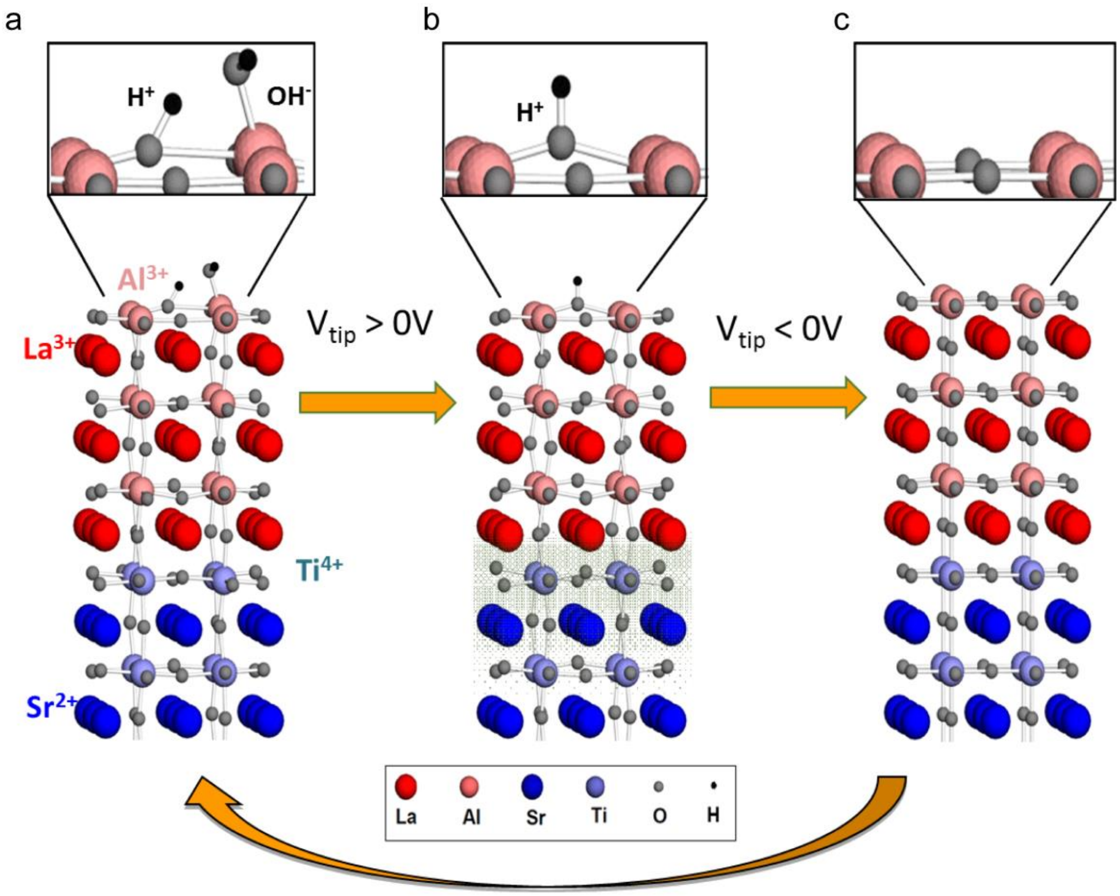

Figure 2.8 "Water cycle" mechanism of c-AFM nanolithography at LAO/STO. a, Water can be spontaneously adsorbed at the LAO surface. **b,** Positively biased tip removes OH^-, leaving H^+ and producing a metallic interface. **c,** Negatively biased tip bias removes residual H^+ thus restores the interface to be insulating. Adapted from C. S. Hellberg, APS talk slides.

2.3.3 On-demand nanodevices and nanostructures

The c-AFM lithography method enables on-demand nanodevices and nanostructures be fabricated at LAO/STO to fulfill various application and scientific research purposes. Sketched field effect transistor (FET) shows high on-off current ratio [57] and can operator at frequency in excess of 2 gigahertz (GHz) band with (Fig. 2.9a and b) [115], making it a potential candidate for logic elements. Sketched single electron transistor (SET) in LAO/STO is also realized using the c-AFM lithography (Fig. 2.9c). The conducting island is as small as several nanometers. By using the side gate, a single electron can be precisely controlled to tunnel in or out of the center island [116]. Written with an AFM tip using an asymmetric voltage (e.g. triangular wave from -10 V to 10 V), electric rectifiers can also be created (Fig. 2.9d) which allows current flow only in one direction [117]. A nano junction created by cutting the nanowire with a negatively biased tip can serve as a sensitive photodiode [118]. With a laser illumination, a highly localized photo current can be detected on the junction (Fig. 2.9e). This nano junction structure can also work as a terahertz (THz) radiator and detector (Fig. 2.9f) [119].

Besides these all-oxide based nanostructures/nanodevices for potential applications, nanostructures, e.g. nanowires, Hall bar structures, quantum dots (QD), confined nanowires with main channel width ~ 10 nm, are created to explore the exotic 1D and 0D transport phenomena at LAO/STO. 1D superconductivity at LAO/STO interface was thoroughly investigated and characterized [120,121]. Enhanced high mobility was reported in the 1D nanowires [122]. Fabry-Perot interference and conductance quantization were observed in the confined nanowire structures. In the superconducting single electron transistor (SSET) device, where the QD is coupled to two superconducting nanowire leads and a side gate, electron pair can form without showing superconductivity [59], demonstrating an unconventional electron paring phase. Andreev band states (ABS) was also observed in the SSET device.

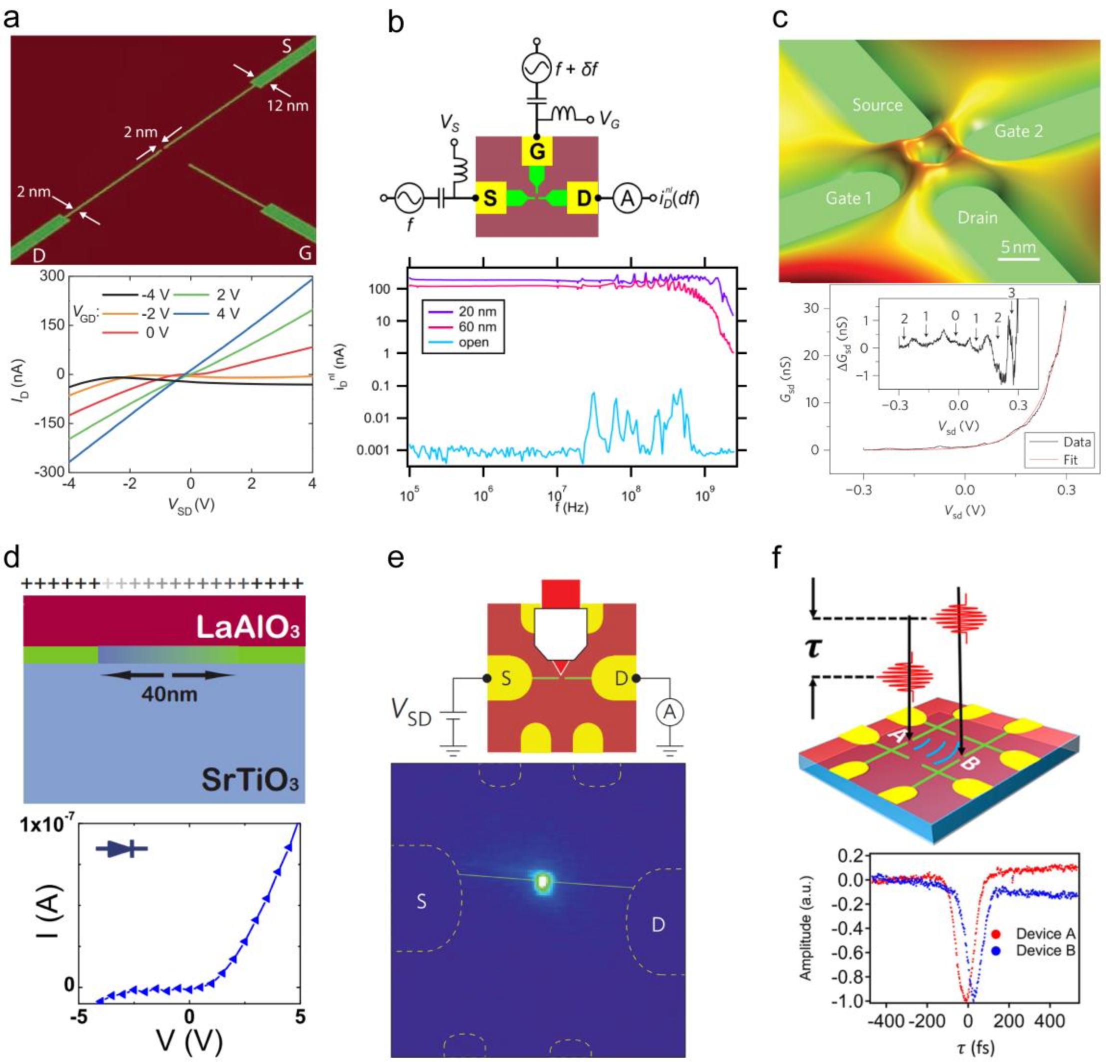

Figure 2.9 On-demand nanoelectronics. a, nanoscale field effect transistor (FET) IV curves under different gate voltages. (Adapted from Ref. [57]). **b,** FETs can operator at frequency > 2 gigahertz (GHz) (Adapted from Ref. [115]). **c,** single electron transistor (SET) created by c-AFM lithography with the Column peaks resolved in the transport measurements (Adapted from Ref. [116]). **d,** nanodiode and the IV performance showing rectifying function. (Adapted from Ref. [117]). **e,** nanojunction structure serves as a photodiode where photocurrent generates under laser illumination (Adapted from Ref. [118]) . **f,** nanojuncton structure works as a terahertz radiator and detector (Adapted from Ref. [119].

2.4 ELECTRICAL TRANSPORT MEASUREMENTS IN DILUTION REFREGERATOR

Quantum transport measurements usually require low temperature (mini Kelvin range) to suppress the thermal excitations. In our quantum transport study on LAO/STO, a ^{3}He/^{4}He dilution refrigerator (DR) is commonly used to provide the low temperature condition. External magnetic field is also integrated into the DR system. Other electronics like amplifiers, data acquisition (DAQ) cards are customized and programmed by Labview for transport measurements.

2.4.1 Dilution refrigerator (DR)

The dilution refrigerator, first proposed by Heinz London in the early 1950s and experimentally realized in 1964 in the Kamerlingh Onnes Laboratory at Leiden University, is the only continuous refrigeration method for reaching temperatures below 0.3 K. The cooling power is provided by the heat of mixing of the ^{3}He and ^{4}He isotopes. When cooled below approximately 870 millikelvin (mK), the mixture undergoes spontaneous phase separation to form a ^{3}He-rich phase (the concentrated phase) and a ^{3}He-poor phase (the dilute phase). In the mixing chamber of a DR, the concentrated phase (practically 100% ^{3}He) and the dilute phase (about 6.6% ^{3}He and 93.4% ^{4}He), are in equilibrium and separated by a phase boundary. The ^{3}He is diluted as it flows from the concentrated phase through the phase boundary into the dilute phase. The heat necessary for the dilution is the useful cooling power of the refrigerator, as the process of moving the ^{3}He through the phase boundary is endothermic and removes heat from the mixing chamber environment. The working fluid is ^{3}He, which is circulated by vacuum pumps at room temperature.

2.4.2 Electrical transport measurements

The electrical transport measurements methods can be calcified into two main categories, alternating current (ac) and direct current (dc) measurements.

The ac measurements usually involves using lock-in amplifiers. The idea of lock-in detection is applying an ac signal to the device with certain frequency that is away from any noise frequencies, then detect the response signal only at that specific frequency, effectively filtering out the noises. The ac measurements (or lock-in measurements) are used to monitor the resistance (or conductance) of a device as a function of time (during the c-AFM lithography), temperature (cooling down samples), magnetic field (magnetoresistance measurements), or gate voltages (back gate tuning).

The dc measurements are used to obtain the IV curves, which can be numerically differentiated to calculate the differential resistance. The IV curves contain all the electrical transport information. If the dc IV curve is linear, the slope should give the same resistance value as the ac measurements. We can also continuously measure the IV curves while sweeping magnetic field, gate voltage or temperatures.

To exclude the contacting resistance, 4-terminal measurements are routinely performed, which only monitor the resistance between two voltage probes. All the electrical transport measurements are realized using the PXI-card from National Instrument (NI) and programmed using Labview.

3.0 PIEZORESPONSE AT LAO/STO HETEROSTUCTURE

Electromechanical response has been reported in LAO/STO heterostructures [56] with relation to the interface conductance. External stresses can also tune the LAO/STO interface conductance [70], suggesting strong correlation between the interfacial carrier density and the lattice distortions. To further understand the electromechanical behavior in LAO/STO, especially its dependence on carrier density, our group performed non-local piezoresponse force microscopy (PFM) experiments on 3 uc LAO/STO [72]. A hysteretic piezoresponse was observed under a variety of environmental and driving conditions [67]. The hysteresis can be suppressed when either the sample was placed in vacuum or the interface was electrically grounded. The presence of ions also affected the hysteresis. A simple physical model related to surface adsorbates and interface carrier-mediated lattice distortions was presented to account for the observed phenomena. Using the same non-local PFM setup, high-resolution non-destructive imaging of conductive nanostructures was realized [69]. PFM images of conductive and insulating nanoscale features were achieved with feature sizes as small as 30 nm. The measured nanowire width from PFM was well correlated with that obtained from nanowire erasure [49].

To quantify the relation between lattice distortions and carrier density in LAO/STO, two simultaneous measurements, PFM and capacitance spectroscopy, were performed on top-gated LAO/STO [68]. The observed hysteretic PFM responses show strong correlation with the capacitance signals, suggesting an interfacial carrier-mediated structural distortion associated with the gate-tuned MIT. In addition, the frequency dependence of the capacitance enhancement in LAO/STO was also well-matched to local PFM measurements. Our experimental results provide a fuller understanding of the top-gate tuned MIT in oxide heterostructure, which could be helpful for the development of future oxide-based nanoelectronics.

3.1 NON-LOCAL PIEZORESPONSE OF LAO/STO

3.1.1 Hysteretic behavior in LAO/STO

The conductance of LAO/STO interface can be tuned by applying a back gate voltage and this tuning has a hysteretic effect [48]. Positive back gate voltage increases the interfacial conductance and the high conductance remains for a certain time after the gate voltage is reset to zero. Using PFM, Bark *et al.* observed hysteretic electromechanical response at LAO/STO interface [56]. It was demonstrated that the piezoresponse was correlated with the interface conductance and therefore can be tuned by electrical poling. Followed experiments showed that mechanical stress can also tune the interface conductance due to the electromechanical coupling [70].

To investigate the hysteretic piezoresponse at LAO/STO interface, we performed a series of non-local PFM experiments on 3 uc LAO/STO heterostructures. By combining c-AFM lithography technique with PFM detection, we explored the conditions under which PFM hysteresis was observed and help to explain its physical origin.

3.1.2 Sample growth and device fabrication

The samples used for our PFM study are grown by depositing 3 uc LAO on a TiO_2-terminated (001) STO substrates using pulsed laser deposition at temperature 550 ℃ and oxygen partial pressure 10^{-3} mbar. The LAO layer thickness is monitored using *in-situ* reflection high energy electron diffraction (RHEED). Electrically conductive contacts to the interface are prepared by first etching 25 nm deep trenches through the LAO layer via an Ar ion mill and then filling them with 4 nm Ti followed by 25 nm Au bilayer electrodes via sputtering. The electrical contacts are arranged to allow a 30 μm × 30 μm "canvas" (Fig. 3.1a) to be patterned using c-AFM lithography. The back surface of the STO substrate is affixed to a copper substrate using silver epoxy so that a back-gate voltage V_{bg} can be applied.

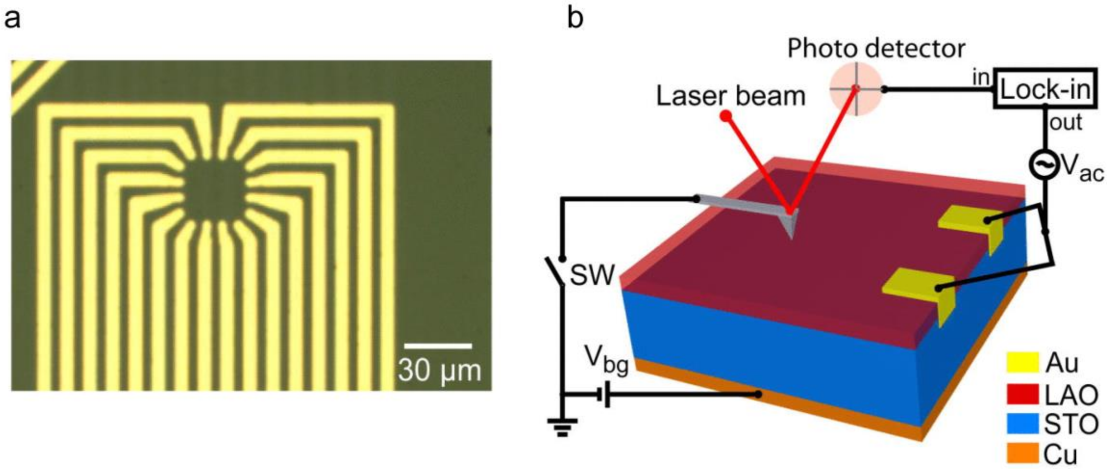

Figure 3.1 Sample image and experiment set-up schematic. a. 30 um × 30 um canvas. **b.** Schematic of non-local PFM set-up.

3.1.3 Non-local PFM setup

A conductive Pt-coated silicon probe contacts the LAO surface. Experiments are performed under one of the two configurations. For some experiments, the conductive AFM tip is connected to ground, while in other configurations the probe is electrically isolated. An ac voltage $V_{ac}\cos(2\pi f t)$ is generated by a lock-in amplifier and applied to two electrodes that make contact to the interface (Fig. 3.1b). The ac voltage can induce a piezoresponse that is measured through the deflection of the AFM cantilever and detected using the same lock-in amplifier. The frequency f ~ 300 kHz is adjusted to take advantage of resonant enhancement and optimize the response before measurements which are performed under a given set of experimental conditions. Large frequency shifts can sometimes occur in these types of measurements. However, such shifts are not observed in our measurements. Because the ac voltage is applied to the conductive electrodes instead of the AFM tip, the PFM response is referred to as "non-local". A dc voltage V_{bg} is applied to the back of the sample. All of the experiments described below are performed at room temperature, under varying conditions of relative humidity (RH) and atmospheric pressure.

The "non-local" PFM (NL-PFM) arrangement is different from typical "local" PFM experiments. In a typical local PFM experiment, a combined ac and dc signal is applied to the conductive AFM tip and the resulting piezoelectric response is detected at the same location. The applied voltage on the tip can affect the sample in many ways. Specifically, surface charge deposition [123] or electrochemical process [71] can happen and both can possibly contribute to the electromechanical response. However, in the non-local geometry, the biased tip effects are avoided since no voltage is applied to the tip; alternatively, the AFM tip can remain electrically isolated. The results described below shows an insensitivity of the PFM response to the electrical connectedness of the tip, suggesting that direct charge transfer from the tip is not responsible for the non-local PFM signal.

3.1.4 PFM response under controlled environment

We performed a series of NL-PFM experiments on 3 uc LAO/STO under four combinations of conditions: with the AFM tip either floating or grounded; and under atmospheric conditions (760 Torr, 40% RH) or in vacuum (10^{-5} Torr). The conductive tip is positioned over 3 uc LAO/STO which has an insulating interface (Fig. 3.2a). NL-PFM amplitude and phase are measured as a function of back gate voltages V_{bg} (Fig 3.2d). V_{bg} is swept in a cyclic manner as: 0 V→10 V→ -10 V→ 0 V and V_{bg} is always on when measuring the piezoresponse. Significant hysteresis is observed at atmospheric conditions for both grounded and isolated AFM tips. The sign of the piezoresponse changes in the range $0\ \mathrm{V} < V_{bg} < 5\ \mathrm{V}$, as can be seen from the change in phase of the response. By contrast, no hysteresis is observed for the experiments performed under vacuum.

A similar series of experiments is performed after lithographic patterning ("writing") a 1 µm × 1 µm square region and subsequently locating the AFM tip at the center of the square (Fig. 3.2b). This writing process is achieved by electrically connecting the AFM tip to a +10 V source and scanning over the square area in a raster fashion. However, the conductive square is still electrically isolated from the conducting electrodes. The results from the NL-PFM measurement show a strong enhancement of the piezoresponse by almost a factor of three under atmospheric conditions (Fig. 3.2e); however, the hysteretic response is still suppressed under vacuum. The chamber is vented to atmosphere (760 Torr, 40% RH), and the square written area is electrically connected to one of the conducting electrodes using the same writing procedure (Fig. 3.2c). During the connection process, the AFM tip does not come into contact with the central area of the 1 µm × 1 µm square; instead only the edge of the conducting square is brought into contact with an "L" shaped conductive region that is connected to the electrode. After writing, the AFM tip is again placed at the same location as for the two previous sets of experiments, and the four types of measurements (tip connected/isolated; atmosphere/vacuum) are repeated. Now in the case with electrical-connected written square pattern, a non-hysteretic piezoresponse is observed for all four conditions (Fig. 3.2f).

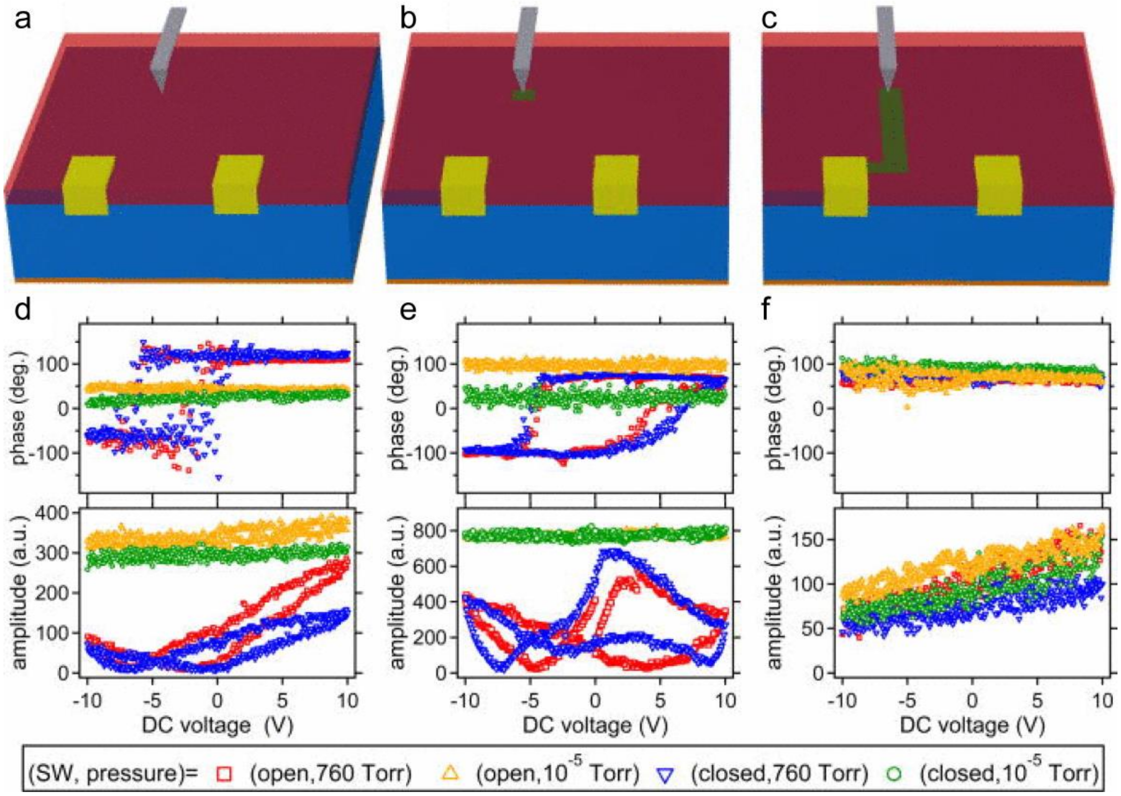

Figure 3.2 Non-local PFM under various conditions. a, AFM tip is engaged 10 μm away from the electrodes. **b,** AFM tip is engaged after writing a 1 μm square. **c,** AFM tip is engaged after writing a L-shape strip that contacts the electrodes. **d, e, f,** Piezoresponse phase signal (upper panel) and amplitude signal (lower panel) as a function of back gate voltage for configuration **a**, **b**, and **c**, respectively.

To further explore the nature of the hysteretic PFM response, we perform a related set of experiments under vacuum conditions with the presence of ions generated from a vacuum ion gauge, which can be controlled to be on or off (Fig. 3.3a). The chamber pressure is estimated to be 10^{-4} Torr based on a pressure reading of the ion gauge prior to the beginning of the experiment. The gauge is left off for 30 minutes before the first measurement. Fig. 3.3b shows the NL-PFM response of 3 uc LAO/STO as a function of V_{bg} under vacuum conditions similar to the case of Fig. 3.2a (i.e., no square or conductive path written); no hysteresis is observed as expected. The ion gauge is turned on and the NL-PFM is measured after 5 minutes (Fig. 3.3c), 15 minutes (Fig. 3.3d), and 30 minutes (Fig. 3.3e). Over time, a wide hysteresis loop appears with increasing width.

Then, the ion gauge is turned off. The width of the hysteresis loop decays significantly after 30 minutes (Fig. 3.3f) and is restored to the original state after 90 min (Fig. 3.3g).

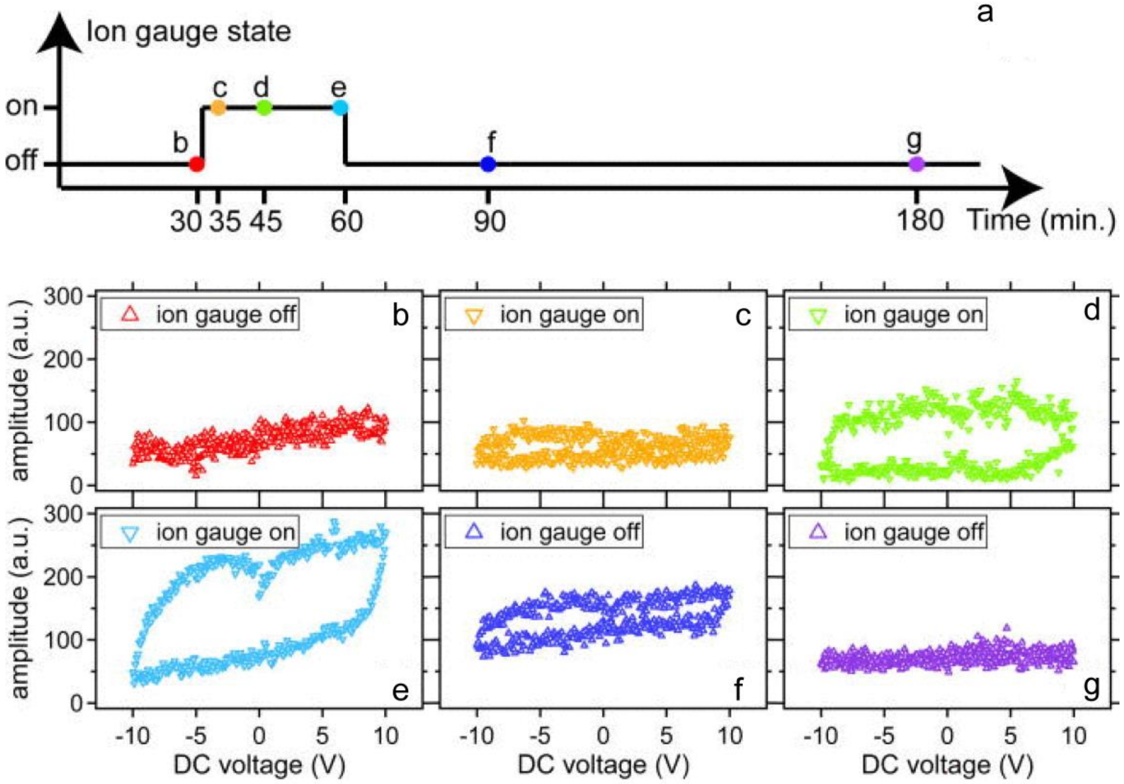

Figure 3.3 Non-local PFM performed with ion source. a, Diagram indicating the state of the ion source versus time. **b-g,** Non-local PFM amplitude versus back gate voltage at various time.

3.1.5 Possible explanations

The experimental results are consistent with a mechanism in which the role of charged adsorbates (i.e., ions) helps to regulate the hysteretic NL-PFM response (Fig 3.4). The experimental results from Fig. 3.2 show that hysteresis is not observed when the experiments are performed in vacuum. However, significant hysteresis is observed under vacuum conditions when ions are generated from a source. Here, we propose one possible mechanism that could produce the PFM response that is related to the LAO surface adsorbates.

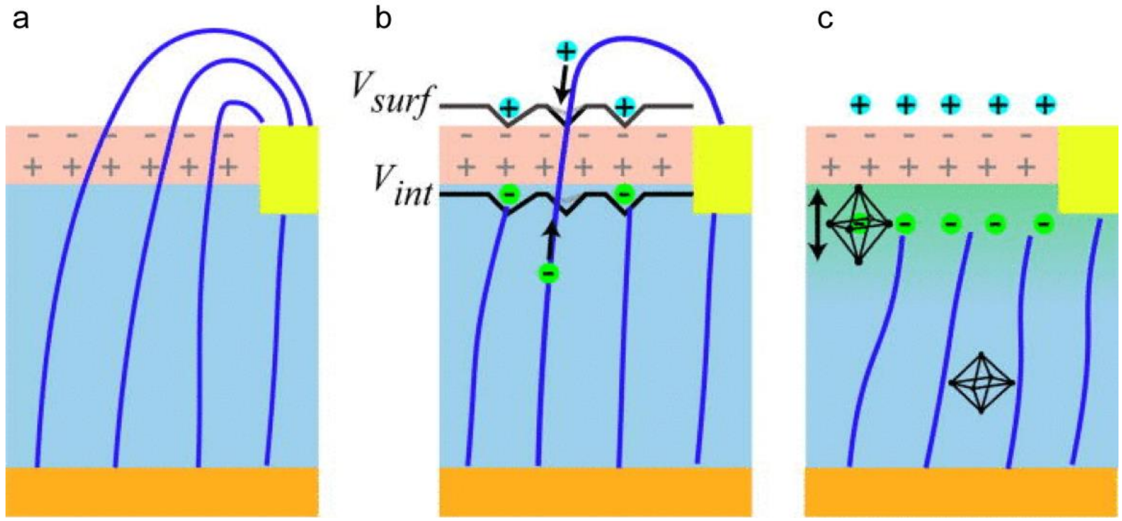

Figure 3.4 Possible mechanism of NL-PFM at LAO/STO. a, Electric field lines (blue) generated between bottom electrode and interface contact. **b,** Surface charges and interface electrons form bound states. **c,** A conducting LAO/STO interface screens the electric field and the hysteretic PFM response is not observed. Electrons at the interface results in a Jahn-Teller distortion of the oxygen octahedral, which is related to the PFM response.

In the absence of charged surface adsorbates, e.g., under vacuum, one expects a small but non-negligible contribution to the NL-PFM signal that originates from coupling of the fringe electric fields across the polar LAO layer (Fig. 3.4a). While LAO is not piezoelectric in the bulk, a thin oriented LAO layer shows electrostrictive effects [124]; no hysteretic response is expected due to the LAO layer in isolation. However, the electric field can attract free ions to the LAO surface (Fig. 3.4b). Such adsorbates may have a small binding energy to the surface, and this binding energy can be greatly increased if the charge is compensated by electron accumulation at the interface. These electrons can come from remote donor sites, or from the nearby conducting electrodes. The surface charge and electron can form an electrostatic bound state (indicated by V_{surf} and V_{int}), which may lead to a hysteretic relation between the surface charge density and the back gate voltage V_{bg}. After c-AFM lithography, the positively biased tip can locally deposits a large amount of H^+ ions on the LAO surface [114] which attract electrons at the LAO/STO interface, therefore the PFM hysteresis is enhanced. However, when the writing area is connected to the electrode (Fig. 3.4c), the interface effectively screens the top LAO surface, and hence adsorption/desorption of ions becomes unlikely as V_{bg} is varied so the hysteresis is suppressed.

The presence of electrons in the STO region near the interface is expected to produce noticeable distortion of the oxygen octahedra (Fig. 3.4c), due to e.g. Jahn-Teller effects. This elongation was first reported for the LAO/STO system by Maurice *et al.* [125] using transmission electron microscopy. Other x-ray techniques also detect lattice distortions at the interface [126,127]. The interfacial lattice distortion can result in the PFM response and is strongly related to the carrier density [128]. It is noted that electrochemical processes have been shown to produce a PFM response in LAO/STO for a local PFM set-up [71]. However, our results show that the hysteretic PFM responses are similar when the tip is either electrically isolated or grounded, therefore, it is unlikely that electrochemical processes play a significant role in our PFM results described here.

3.2 PFM IMAGING OF LAO/STO NANOSTRUCTURES

The NL-PFM technique reported above constitutes a new experimental probe of electron density and interfacial electronic properties for oxide heterointerfaces. In addition, the “written” and “unwritten” areas in LAO/STO exhibit different PFM response amplitude [69], therefore our NL-PFM set-up can be used for real-space imaging of nanoscale devices that are buried in the oxide interface with no topographic features. Determination of the nanoscale dimensions has previously required a destructive readout (e.g., local restoration of an insulating state) [49]. Here we show that high-resolution, non-destructive imaging of conductive nanostructures can be realized using our NL-PFM method. Images of conductive and insulating nanoscale features are achieved with feature sizes as small as 30 nm. The LAO/STO samples and experiment set-up used for PFM imaging are the same as for the NL-PFM measurements.

3.2.1 PFM imaging of nanowires

Here we first use The PFM imaging technique to visualize a single nanowire created by c-AFM lithography. Prior to creation of the nanowire, “virtual electrodes” are created by raster scanning a rectangular-shaped area that overlaps each of the two adjacent Au electrodes with V_{tip} = 8 V. Then a conducting nanowire is created between the two “virtual electrodes” with writing parameters V_{tip} = 8 V and moving speed v_{tip} = 600 nm/s. To compare the wire width measured from PFM method with the wire width measured from the erasing process, the wire is cut at the middle by moving the tip perpendicular to the nanowire with $V_{tip} = -8$ V and speed v_{tip} = 10 nm/s (Fig. 3.5a). The formation of this conducting nanowire and the cutting are confirmed by monitoring the conductance during the lithography with 0.1 V source ac voltage. The conductance drop profile versus position can be fit to the functional formula $\mathrm{G(x)} = G_0 - G_1 \tanh(x/h)$; the wire width is found to be 8 nm as the full-width at half-maximum (FWHM) of the differential conductance profile $dG(x)/dx$ (Fig. 3.5b). After the c-AFM lithography, an ac voltage $V_{ac}\cos(2\pi f t)$ with amplitude V_{ac} = 0.5 V is applied to these two Au electrodes. Frequency tuning is performed to track the resonant frequency f_r before taking PFM images. The excitation voltage amplitude is held at V_{ac} = 0.5 V and the frequency f is fixed at f_r during the PFM image scan. During all the PFM imaging presented here, the resonant frequency f_r is in the range between 275 kHz and 300 kHz for the Pt coated tip we used. PFM imaging at the contact resonance frequency helps to improve the signal-to-noise ratio, but reliable quantitative imaging suffers from possible frequency shifts and quality-factor variations that can take place due to changes in elastic modulus or damping

[129]. In the PFM imaging presented here, the large PFM signal amplitude contrast is not due to resonance frequency shift since the resonance frequency shift under dc bias sweeping is less than 1 kHz [68].

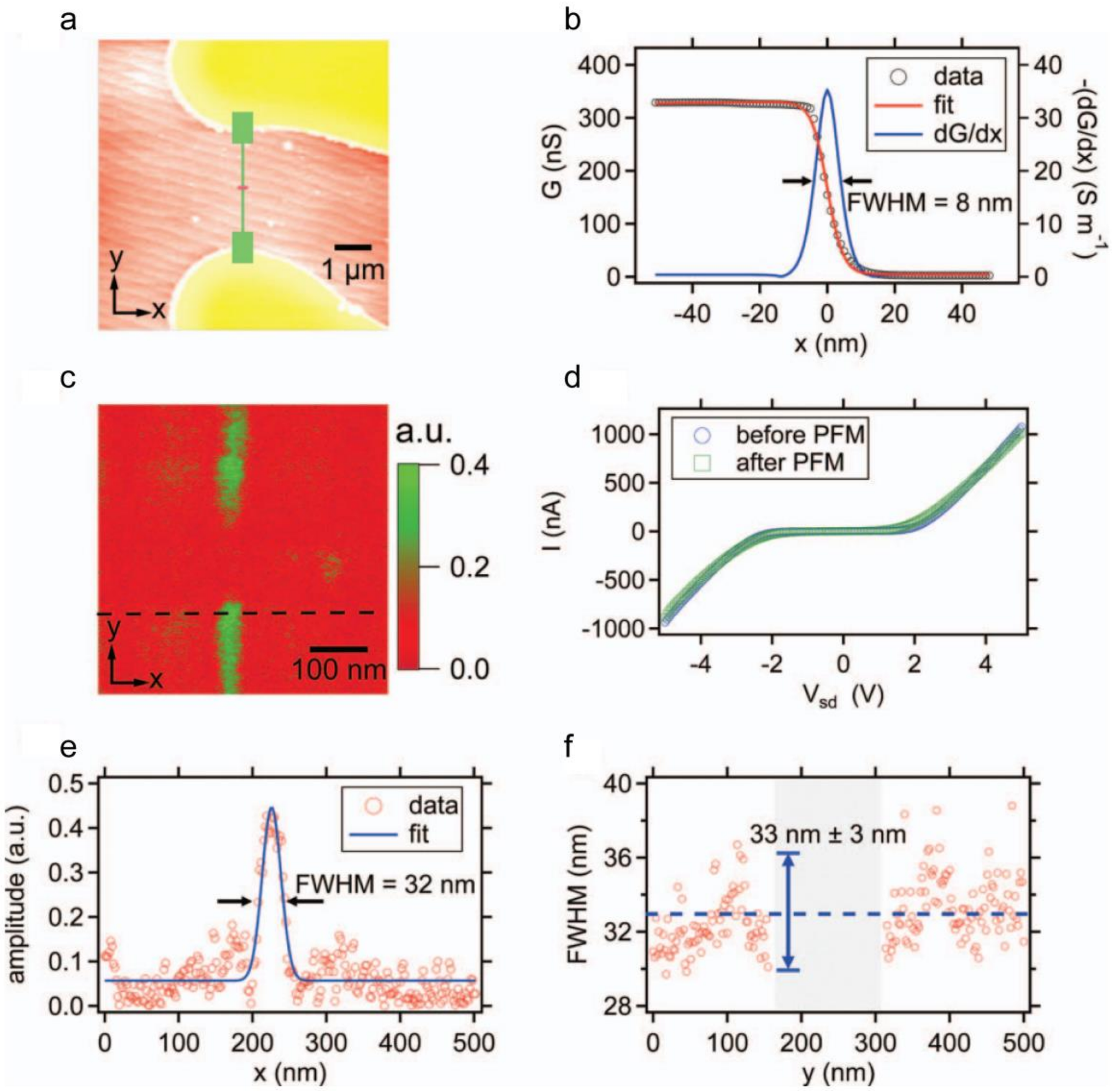

Figure 3.5 PFM imaging of single nanowire. a, c-AFM lithography schematic. **b,** Estimation of the wire width by fitting the conductance drop curve. **c,** PFM amplitude image of the structure shown in **a**, solid line is the Gaussian fitting and its FWHM is indicated**. d,** DC IV curves of the structure before and after PFM imaging. **e,** PFM amplitude of the dashed line shown in **c. f**, Wire width distribution as a function of y axis.

By scanning over the area where the nanowire was written, a PFM amplitude image of the cut single nanowire is observed (Fig. 3.5c). The dc current-voltage (IV) curves of the structure before and after taking the PFM image are also measured (Fig. 3.5d). The two IV curves are highly overlapping, indicating that the PFM process is non-destructive. The nanowire width is obtained by fitting a line cut (Fig. 3.5c, dashed line) of the PFM amplitude signal to a Gaussian function (Fig. 3.5e). The result yields a FWHM of 32 nm. This analysis is repeated along the nanowire (Fig. 3.5f), yielding an average wire width of 33 ± 3 nm.

In c-AFM lithography, the dimensions of the nanostructures produced are influenced by various lithography parameters (e.g., V_{tip}, v_{tip}), environmental factors such as the relative humidity [114] as well as other uncontrolled sample and/or canvas variations. Keeping the controllable parameters fixed, and working with a single canvas, it is possible to examine how the PFM imaging depends on the writing speed. Five parallel wires, each separated by 200 nm, are created with a fixed tip voltage $V_{tip} = 10$ V at writing speeds 200 nm/s, 400 nm/s, 600 nm/s, 800 nm/s, and 1000 nm/s (Fig. 3.6a). The temperature and relative humidity are controlled stable at 72 °F and 34%, respectively. The wires are then cut in the center by using $V_{\text{tip}} = -8$ V and moving the tip perpendicularly to the wires at speed $v_{\text{tip}} = 10$ nm/s. As with all of the other nanowire images, no topographic features or crosstalk is observed in the PFM images (Fig. 3.6b) by comparing the AFM topography image of the same area (Fig. 3.6a, inset). Small features in the PFM images might be due to sample inhomogeneity. The wire widths are measured by fitting the horizontal profile extracted by averaging over the entire imaging region (Fig. 3.6c). This data set shows a consistent trend that for a fixed writing voltage the wire width decreases with increasing writing speed.

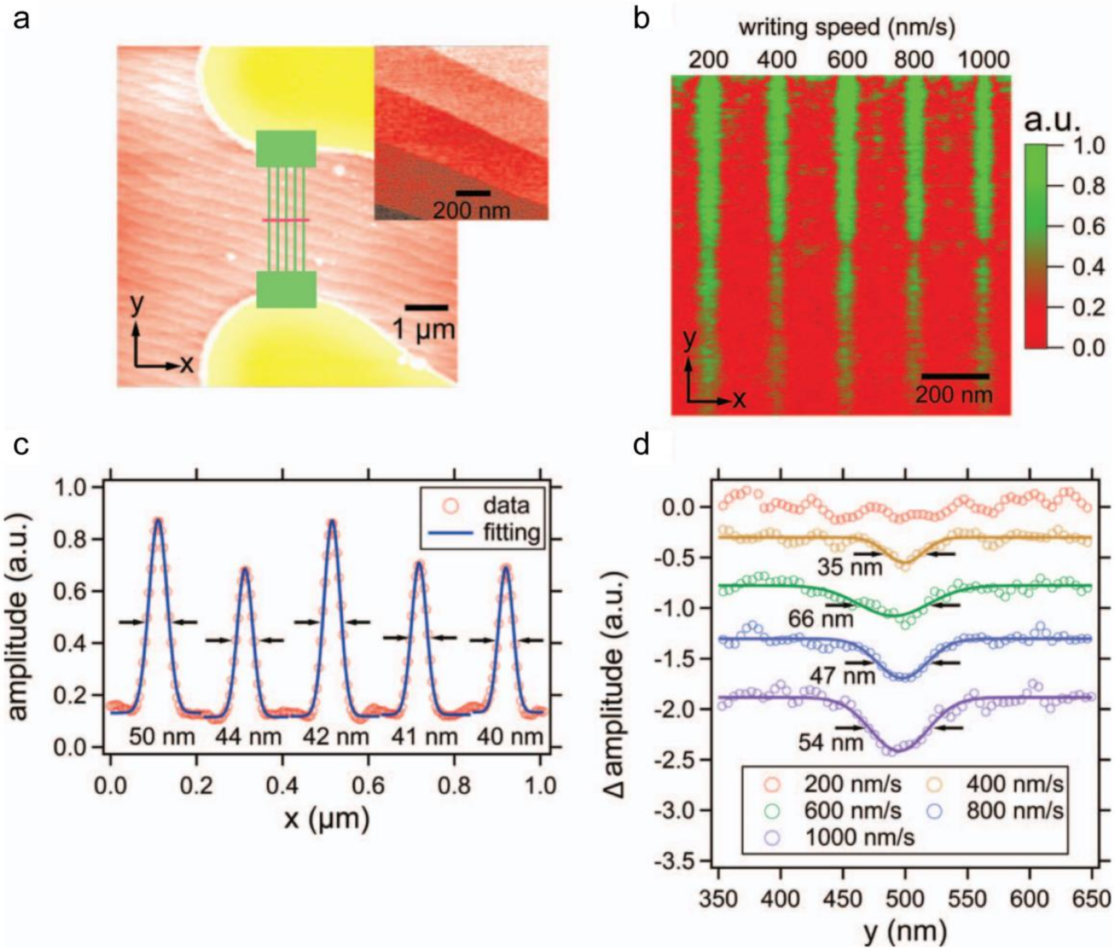

Figure 3.6 PFM imaging of five parallel nanowires. a, Lithography schematic: five wires, separated by 200 nm, are written at speeds of 200 nm/s, 400 nm/s, 600 nm/s, 800 nm/s, and 1000 nm/s with V_{tip} = 10 V; the wires are then cut in the middle using $V_{tip} = -8$ V at speed v_{tip} = 10 nm/s. Inset: topography image of the same area as **b.** PFM amplitude image of the five parallel wires. **c,** PFM amplitude versus x axis after averaging the whole PFM imaging area. Solid line is the Gaussian fitting and FWHM is indicated. **d,** PFM amplitude versus. y axis of five nanowires after subtracting a linear background term. Curves are offset for better viewing**.** Solid line is the Gaussian fitting to the curve with the same color and its FWHM is shown.

The same analysis can be used to measure the insulating gap width from the PFM image (Fig. 3.6d). For each wire, the vertical PFM amplitude profile is extracted by averaging the wire region. A linear background is subtracted, which mainly comes from the slow decay of the nanowires under ambient environmental conditions [114]. This decay is probably the reason for the change in amplitude from the upper and lower half of the PFM image (Fig. 3.6b), since this PFM image is scanned from top to bottom. The wire written at v_{tip} = 200 nm/s does not show an obvious gap in the middle as can be seen in the PFM image. The wire written at v_{tip} = 600 nm/s shows a relatively large gap size from the Gaussian fitting and the gap is also difficult to discern in the PFM image. A possible reason is that after the cutting and before the PFM imaging a frequency tuning is performed at the image center that is also the center of the 10 V, 600 nm/s written wire. Some tuning-induced PFM features can obscure the cutting gap and make the fitting inaccurate. The gap sizes for the wires written at 400 nm/s, 800 nm/s, and 1000 nm/s demonstrate that with all other conditions kept the same, cutting the nanowire created by higher lithography writing speeds tend to produce wider insulating gaps.

3.2.2 Wire width measurement

Generally, the width obtained from PFM measurements is larger than from the erasure method. Most likely, this discrepancy is due to intrinsic resolution for PFM imaging. To help establish a clear relationship between the two available methodologies, the two methods were compared under various writing speeds and tip voltages (Fig 3.7). The width of the same nanowire is obtained by cutting the nanowire (W_{fit}) and measured by PFM (W_{PFM}). A linear fit yields

$$W_{\text{fit}} = 1.02 \times W_{\text{PFM}} - 25.6\ \text{nm} \tag{3-1}$$

The offset between the non-destructive PFM imaging and the destructive erasure-based method (25 nm) is typical of the spatial resolution reported for other piezoelectric thin film materials.

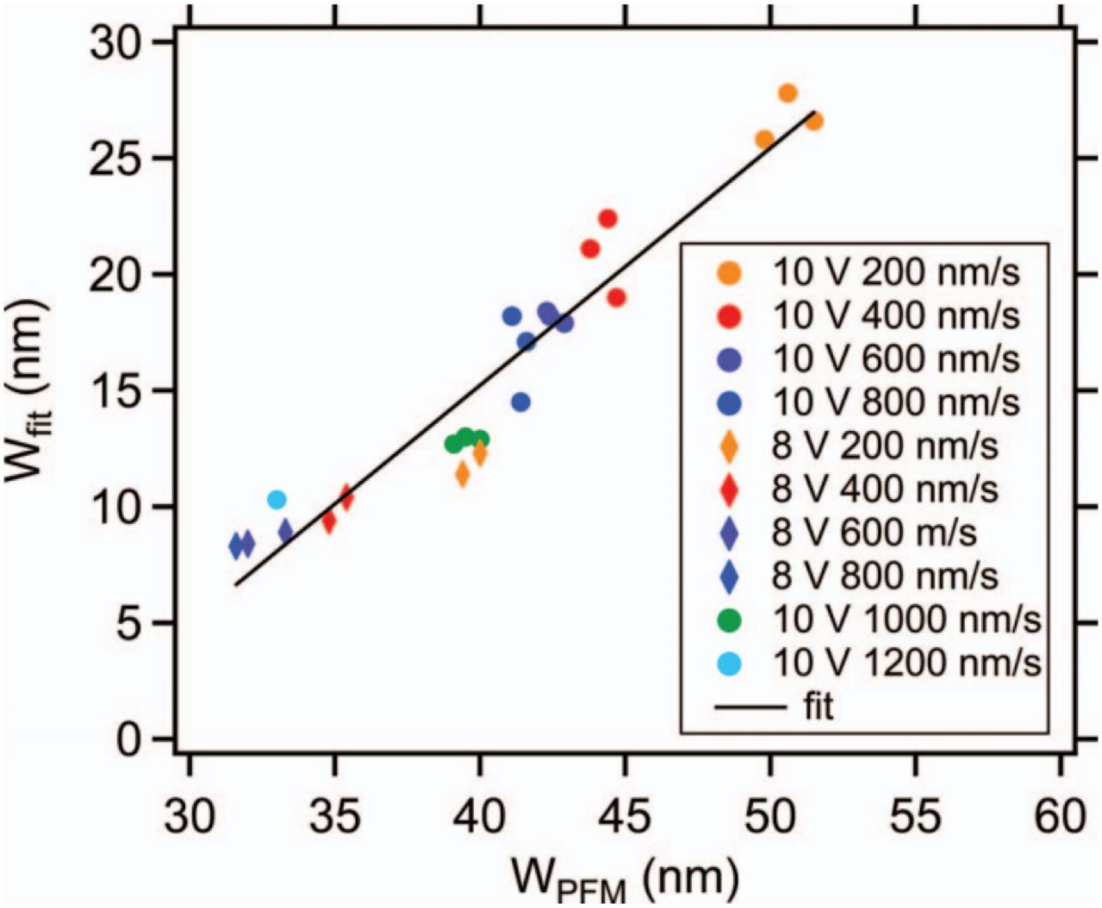

Figure 3.7 Correlation between W_{fit} and W_{PFM}. W_{fit} is calculated from fitting the conductance drop curve, W_{PFM} is the wire width directly measured from the PFM image.Linear fitting (black line) yields $W_{fit} = 1.02 \times W_{PFM} - 25.6$ nm.

3.2.3 PFM imaging of side-gated nanowire structure

We have proposed that the carrier density modulation at the interface, not a direct piezoelectric response produce the PFM signal (Section 3.1) [72]. To further illustrate this, the PFM imaging setup is modified so that instead of grounding the back of the STO substrate, a nearby centrally located electrode is grounded (Fig. 3.8a). A single nanowire and a side gate, located 1000 nm away from the nanowire, are both created with V_{tip} = 10 V. The nanowire is not cut for this experiment, and the side gate is electrically grounded. An ac voltage V_{ac} = 0.5 V at resonant frequency (~ 270 kHz) is applied to the both ends of the single wire; therefore, there is no net current running through the wire. Both the tip and the back gate are electrically floated during the PFM imaging scan. Under these conditions, the applied ac voltage only induces fields within the interface itself, with no electric field applied across the LAO film or STO substrate. These PFM imaging results (Fig. 3.8b) provide evidence in favor of a carrier-mediated lattice distortion as the primary mechanism for our PFM response.

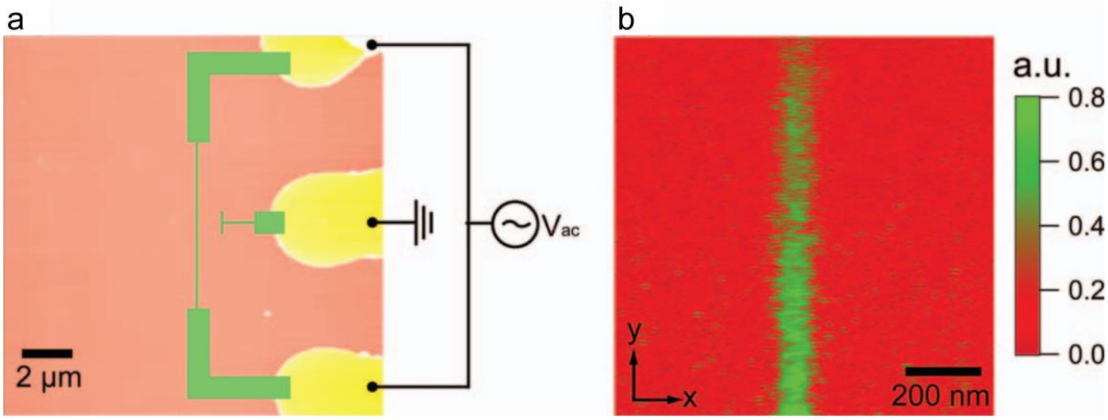

Figure 3.8 PFM imaging of a nanowire near a grounded side gate. a, Lithography and PFM imaging schematic. The same ac voltage with amplitude $V_{ac} = 0.5$ V is applied to both ends of the nanowire and the center gate is grounded. **b,** PFM amplitude image of the wire. Both the tip and back gate are electrically isolated.

3.3 ELECTRO-MECHANICAL RESPONSE OF TOP-GATED LAO/STO

LAO/STO heterostructures are known to exhibit a sharp, hysteretic metal-insulator transition (MIT) with large enhanced capacitance near depletion [130]. Bark *et al.* have characterized gated LAO/STO/LSAT structures using PFM and observed hysteretic behavior near the MIT [56]. However, the intrinsic origin of the top-gate tuned MIT and the mechanism for capacitance enhancement as well as PFM hysteresis are still not well understood. To help clarify the physical origin of the capacitance enhancement and hysteretic piezoresponse, as well as their potential connections to the MIT, simultaneous capacitance-voltage (CV) spectroscopy and PFM measurements are performed on top-gated LAO/STO structures. The CV curves measure the ability of the interface to store electric charge under various top-gate bias conditions. The abrupt change of capacitance is associated with the interfacial MIT. The PFM signals measure the local lattice distortion since it is proposed to arise from a carrier-mediated Jahn-Teller effect at the LAO/STO interface [67]. The observed hysteretic PFM responses show strong correlation with the capacitance signals. In addition, the frequency dependence of the capacitance enhancement is found to be well-matched to local PFM measurements. I and Dr. Feng Bi collaborated on this project. I fabricated all the devices used for the experiments, involved in the experiments, contributed to the data analysis and manuscript writing.

3.3.1 Sample growth, device fabrication and characterization

For this project, LAO/STO heterostructures are fabricated by depositing either 5 uc or 12 uc LAO films on TiO_2-terminated (001) STO substrates using pulsed laser deposition with *in situ* RHEED. Two different growth conditions are used: (1) the substrate growth temperate T = 550 ℃ and chamber background partial oxygen pressure $P = 10^{-3}$ mbar; (2) the substrate growth temperate T = 780 ℃ and chamber background $P = 10^{-5}$ mbar. For samples grown in condition (2), after deposition, they are annealed at 600 ℃ in 300 mbar oxygen pressure environment for one hour to reduce oxygen vacancies. The details of sample growth are introduced in Section 1.4. These samples with the two different LAO layer thickness and grown under the two different conditions produce similar experimental results.

The device geometry is basically a capacitor which is similar to that reported in Ref. [130]. The top-gate electrodes are circular in shape, with a diameter ranging between 100 μm and 600 μm (Fig. 3.9a). The electrodes connecting the interface are arch-shaped with a 20 μm width and fixed separation of 50 μm to the edge of the circular top gates. These arch-shaped electrodes surrounding the top gate are intended to provide an almost isotropic electric field under applied bias.

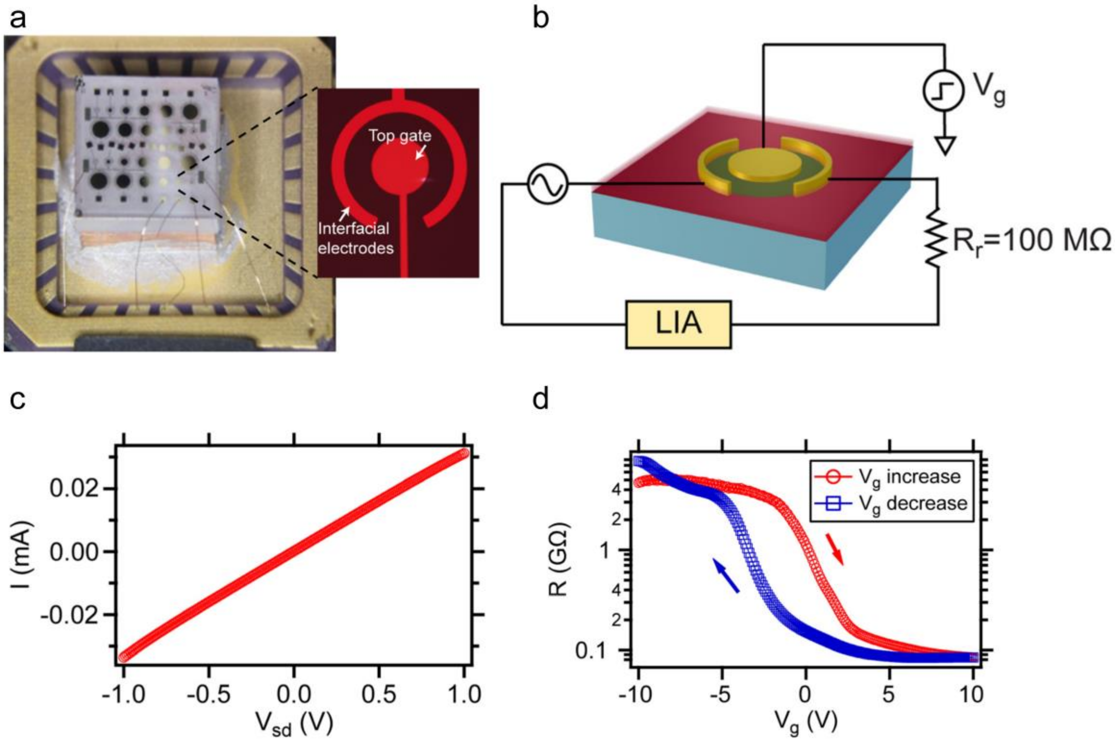

Figure 3.9 Sample geometry and characteristics.a, Photograph of the device geometry. The STO substrate is square with a size 5 mm × 5 mm. The sample is mounted on a ceramic chip carrier. **b,** shematic Schematic diagram showing the interface resistance measurements. **c,** I-V measurement between two separated electrodes that directly contact to the interface. The linear I-V behavior shows that the electrode-interface contact is ohmic. **d**, Resistance of the interface as a function of top gate bias.

The capacitor electrodes are deposited on the LAO/STO samples via DC sputtering. The arc-shaped electrodes are prepared by first creating 25-nm trenches via Ar-ion milling, followed by deposition of 4 nm Ti and 25 nm Au. Then, a series of metallic circular top gates (4 nm Ti and 50 nm Au) are deposited on the LAO surface. The whole sample is affixed to a ceramic chip carrier using silver paint. Electrical contacts to the device are made with an ultrasonic wire bonder using gold wires. The details of device fabrication are introduced in Section 2.1.

To check whether the top gate can effectively tune the carriers at the interface, a simple transport measurement of the interface is performed between two electrodes connected to the interface (Fig. 3.9b). The linear current-voltage (I-V) curve between the arc-shaped electrodes, measured at zero top-gate voltage, indicates that the contacts are ohmic (Fig. 3.9c). Applying top gate voltage (V_g) can tune a nearly two orders of magnitudes change in the interface resistance (Fig. 3.9d). The R vs. V_g curve indicates a MIT near $V_g = 0$. Note that the resistance does not become immeasurably large in the insulating phase because the gate does not extend to the gap region between the two arc electrodes.

3.3.2 Measurements setup

To perform simultaneous PFM and CV measurements, two electrical circuits are connected to one device (Fig. 3.10). A combined dc and "dual-frequency ac signal" is applied to the interface.

$$V_{\text{interface}}(t) = -V_{\text{DC}} - V_{\text{PFM}}\cos(2\pi f_{\text{PFM}} t) - V_{\text{C}}\cos(2\pi f_{\text{C}} t) \tag{3-2}$$

The top electrode is held at virtual ground in order to eliminate possible electrostatic interactions with the AFM probe. Note that the dc component applied to the interface is $-V_{DC}$, so the equivalent top gate bias is V_{DC}. Adjusting V_{DC} tunes the LAO/STO interface between conducting and insulating phases. In order to measure the PFM response, an AFM tip is placed in contact with the top-gate electrode. The AFM tip deflection at the excitation frequency f_{PFM} is detected using a lock-in amplifier.

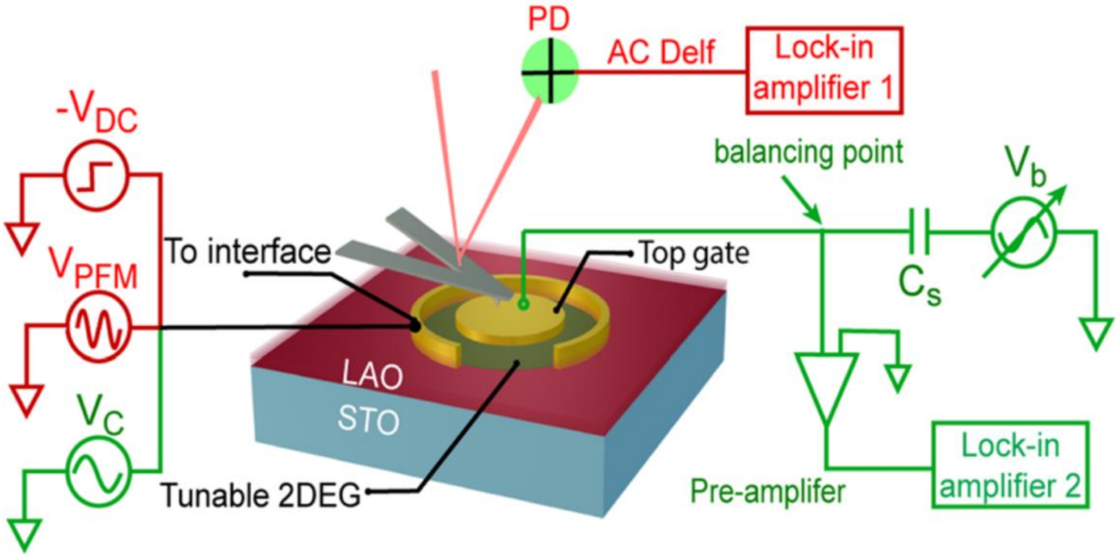

Figure 3.10 Schematic of simultaneous PFM and capacitance measurement set-up. Circuit diagram of PFM measurement (red) is combined with a capacitance bridge (green).

The capacitance C as a function of gate bias V_{DC} is measured simultaneously using a capacitance bridge (the green circuit in Fig. 3.10). The sample is excited with an ac voltage V_{C} in one arm. In another arm, a synchronized ac voltage V_{b} with the same frequency and 180 ° phase shift is applied to a standard capacitor C_{s} (typically 10 pF). The signal at the balancing point is measured by a second lock-in amplifier. During the capacitance measurement, the phase and amplitude of V_{C} are held constant, while V_{b} is adjusted in a feedback loop to null the capacitance channel (90 ° out-of-phase or “Y” channel) at the balancing point. The sample capacitance is calculated from the equation

$$C = C_s V_b / V_c \tag{3-3}$$

Fixed-frequency CV curves can also be acquired using a commercial capacitance bridge (Andeen-Hagerling 2500A) with an ac excitation voltage given by $V_{\mathrm{C}} = 20$ mV, $f_{\mathrm{C}} = 1$ kHz , and V_{dc} is swept at a rate $dV_{dc}/dt = 0.067$ V/s. The capacitance we measured is vertical since our device has a vertical structure of Au/Ti/LAO/2DEG, where Au/Ti is the top gat0e electrode and 2DEG resides at the LAO/STO interface which contacts the arc-shaped electrode. The measured capacitance refers to both the LAO film and the LAO/STO interface. When the interface is conducting (2DEG forms at the interface), the device is similar to parallel plate capacitor, where the 2DEG and the top electrodes are the two conducting plates and the LAO film is the dielectric material. In this case, the measured capacitance is roughly the geometric capacitance. When the interface is insulating (2DEG is depleted), the measured capacitance refers to LAO film combined with the interface. Both capacitance and piezoresponse measurements are performed at room temperature in an enclosed AFM chamber with a small amount of scattered red light ($\lambda \geq 620$ nm), which does not have an observable effect on transport properties.

3.3.3 Capacitance and PFM measurement near MIT

The capacitance measurement results (Fig. 3.11a) indicate a MIT as the gate bias V_{dc} is varied, consistent with the transport measurement (Fig. 3.9d). When V_{dc} decreases ($V_{\mathrm{dc}} < 2$ V), the capacitance signal begins to drop from its saturated value. As V_{dc} decreases further ($V_{\mathrm{dc}} < 0$ V), the capacitance reaches a low and steady base level, indicating that the electron density underneath the circular top gate is substantially depleted by the electric field. The depleted interface can be restored to a conducting state by increasing V_{dc}. As V_{dc} increases and becomes positive ($V_{\mathrm{dc}} > 0$ V), the capacitance increases several-fold, indicating a conducting channel is restored at the interface. The capacitance variation during gate tuning is comparable to that reported in Refs. [130] and [131]. The CV curve also exhibits a stable hysteretic behavior, in agreement with previous studies [131,132].

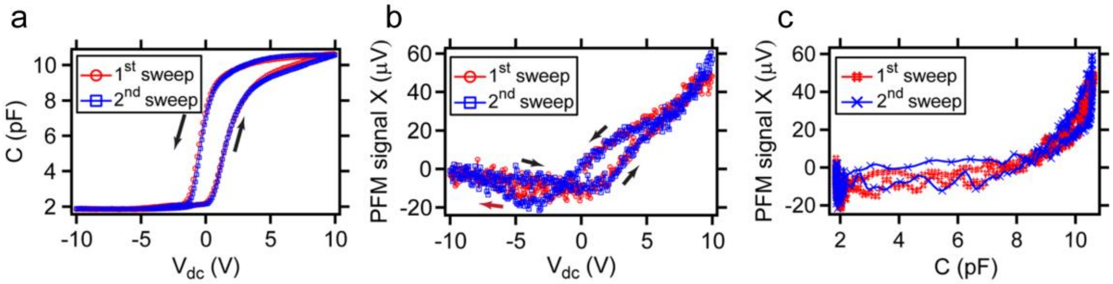

Figure 3.11 Simultaneous CV and PFM measurement results. a, CV curve taken at room temperature at f_C=1 kHz, showing a hysteretic metal to insulator transition as V_{dc} is varied. **b,** Piezoresponse in-phase signals at different values of V_{dc}. The red arrow indicates the initial scanning direction. **c,** Plot showing positive correlation between piezoresponse and capacitance.

Local piezoresponse measurements are performed on the same devices. The piezoresponse signal is measured at a fixed location on the top electrode as a function of V_{dc} (Fig. 3.11b). The ac excitation voltage is given by V_{PFM} = 20 mV and f_{PFM} = 293 kHz, with a voltage sweep rate $|dV_{dc}/dt|$ = 10 mV/s. Far from resonance, any piezoresponse of the sample should be either in phase or out of phase by 180 °with respect to the V_{PFM}. The in-phase PFM signal (X channel) contains most of the essential information of a PFM measurement [133], while the 90 °out-of-phase PFM signal (Y channel) is negligibly small. The X-output (in-phase) piezoresponse signal is correlated with the capacitance signal (Fig. 3.11b): as V_{dc} decreases, the piezoresponse signal is suppressed and when V_{dc} increases, the piezoresponse signal is enhanced. Both hysteresis loops of CV and PFM measurements (Fig. 3.11a and b) are stable as V_{dc} swept forward and backward for successive cycles. Parametric plotting of the piezoresponse versus capacitance (Fig. 3.11c) shows that the hysteresis near V_{dc} = 0 V is highly correlated, however, there are significant deviations at both low and high values of the capacitance. Although the piezoresponse measurements are performed at a single location, this behavior is typical of measurements performed at other locations or devices (Fig 3.12).

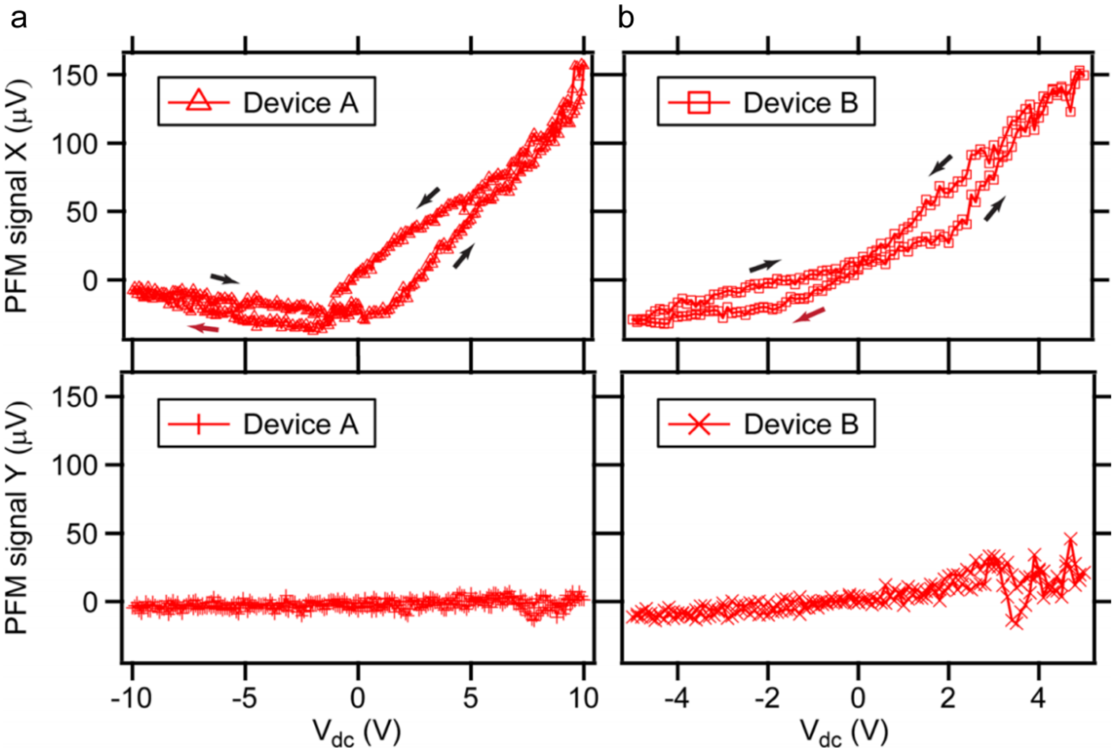

Figure 3.12 Piezoresponse under electric field. a, Piezoresponse signals on device A at a different tip location. **b,** Piezoresponse measurements on device B. X, Y output represent the in-phase and 90 ° out-of-phase piezoresponse signal, respectively. The red arrow indicates the initial scanning direction.

3.3.4 Quantitative PFM and CV analysis

A non-zero piezoresponse implies that there is a lattice distortion as a result of the applied voltage. Therefore, a quantitative analysis of the PFM measurement [133-137] is performed. A series of piezoresponse spectra (Fig. 3.13a) is acquired with V_{PFM} = 20 mV and f_{PFM} from 285 kHz to 305 kHz under a sequence of bias conditions V_{dc} = 0V → -10V → +10V → 0V. The open circles in the intensity graph highlight the contact resonant frequency trajectory as V_{dc} is modulated. For better illustration, the contact resonant frequency is plotted with respect to V_{dc} (Fig 3.13b). The prominent resonant frequency change as well as the hysteretic behavior suggests a change in the height as well as the restoring force of the LAO surface as applied V_{dc} varies.

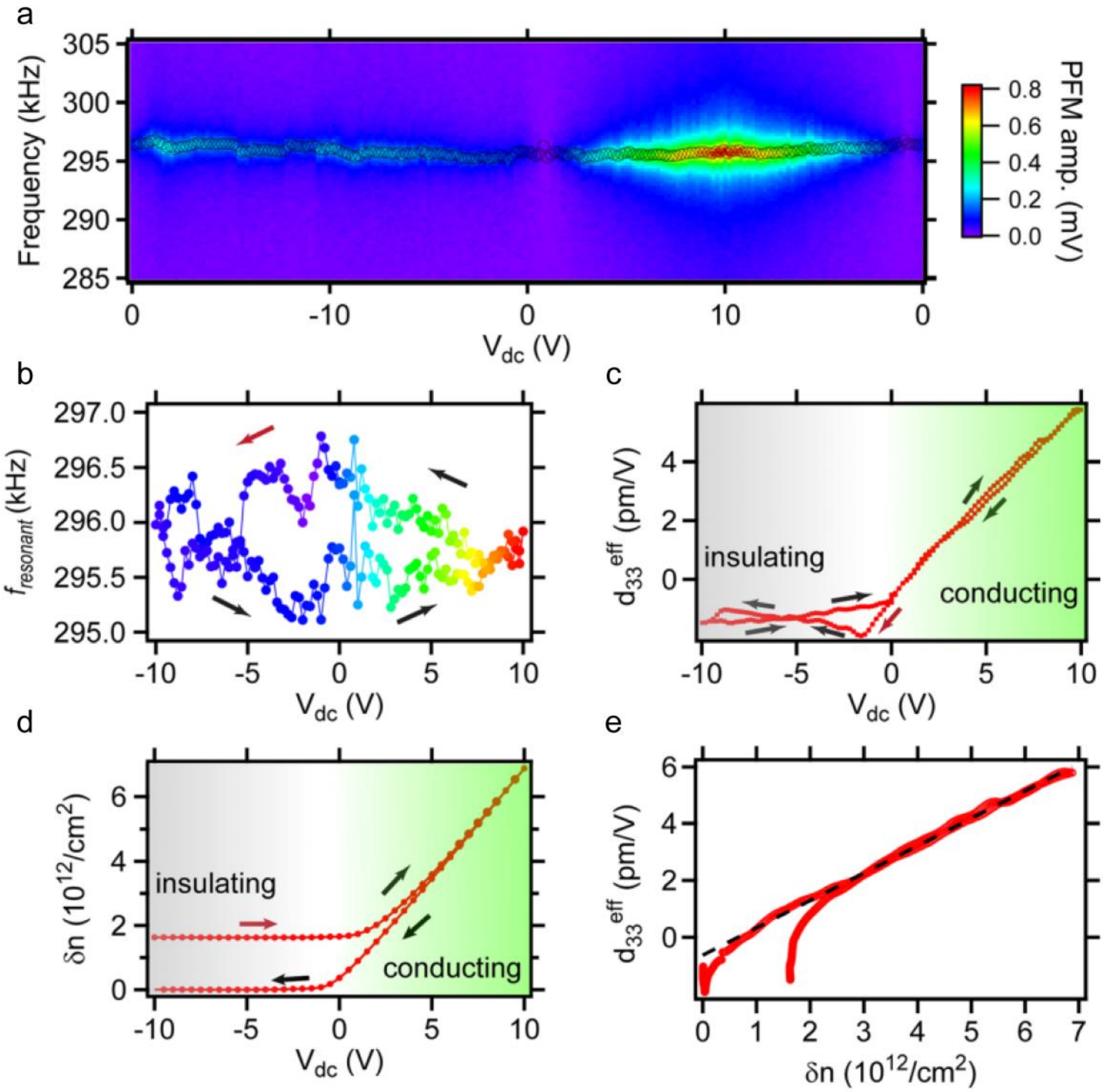

Figure 3.13 Quantitative analysis of PFM spectra on device A. a, Piezoresponse within the frequency band 285 kHz to 305 kHz under various dc bias conditions**.** The open circles in this intensity graph represent the contact resonant frequency peak under each dc bias. **b,** Contact resonant frequency is extracted from **a** and plotted as a function of V_{dc}. The color of each data point represents the piezoresponse amplitude at each resonant frequency. **a** and **b** share the same color legend**. c,** $\boldsymbol{d_{33}^{eff}}$ is acquired from the piezoresponse spectra in **a** using simple harmonic oscillation (SHO) model fitting**. d,** Carrier density change: δn at the interface as a function of V_{dc}**. e,** Plot of $\boldsymbol{d_{33}^{eff}}$ with respect to δn. The red arrows in **b**, **c**, **d**, **e** indicate the initial scanning direction.

To quantify the lattice displacement along z direction, the bias-dependence of the effective piezoelectric strain tensor element d_{33}^{eff} (V_{dc}) (Fig 3.13c) is calculated by first fitting the piezoresponse spectra (Fig 3.13a) to a simple harmonic oscillator (SHO) model as a function of V_{dc}:

$$A(\omega) = \frac{A^{\mathrm{max}}\omega_0^2}{\sqrt[2]{(\omega^2 - \omega_0^2)^2 + (\omega\omega_0/Q)^2}} \tag{3-4}$$

where ω_0 is the resonant frequency, A^{max} is the amplitude and Q is the quality factor. Due to the contact resonant enhancement, the surface deformation will be amplified by Q times, the quality factor of the tip-surface contact resonant system. The X channel signal measured by the lock-in amplifier is denoted by $X(\omega_0, V_{\mathrm{dc}})$, then we have the following equation to relate measured signal $X(\omega_0, V_{\mathrm{dc}})$ to the effective tensor element $d_{33}^{\mathrm{eff}}(V_{\mathrm{dc}})$:

$$d_{33}^{\mathrm{eff}}(V_{\mathrm{dc}})V_{\mathrm{PFM}}Q = X(\omega_0, V_{\mathrm{dc}})\alpha \tag{3-5}$$

where the sensitivity α = 67.75 nm/V, which is obtained from the AFM force curve.

The net vertical surface displacement (Δz) as a function of V_{dc} at the location of the AFM tip can be obtained by integrating $d_{33}^{\mathrm{eff}}(V_{\mathrm{dc}})$ with respect to the applied voltage V_{dc}:

$$\Delta z = z_{\mathrm{dc}}(V_{\mathrm{dc}}) - z_{\mathrm{dc}}(0\ V) = \int_0^{V_{dc}} d_{33}^{\mathrm{eff}}\,(V_{\mathrm{dc}})dV \tag{3-6}$$

In the end, the simplified equations for the effective piezoelectric strain tensor element $d_{33}^{eff}(V_{\mathrm{dc}})$ and lattice distortion $\Delta z_{dc}(V_{\mathrm{dc}})$ are:

$$d_{33}^{eff}\,(V_{\mathrm{dc}}) = \frac{\alpha X\,(V_{dc})}{QV_{PFM}} \tag{3-7}$$

$$\Delta z_{dc}(V_{dc}) = \int_0^{V_{dc}} \frac{\alpha X\,(V_{dc})}{QV_{PFM}}dV \tag{3-8}$$

Therefore now we can obtain the lattice distortion via calculating the effective piezoelectric strain tensor $d_{33}^{\mathrm{eff}}(V_{\mathrm{dc}})$ from the measured PFM signals. The 2D carrier density change at the interface (Fig. 3.13d) is calculated from the CV curves using the equation:

$$\delta n = n(V_{dc}) - n(-10\,V) = (1/eA)\int_{-10\,V}^{V_{dc}} (C(V) - C(-10V)dV \qquad (3\text{-}9)$$

By plotting parametrically $d_{33}^{\mathrm{eff}}(V_{\mathrm{dc}})$ versus δn (Fig. 3.13e), a linear relationship between the strain tensor and carrier density change is revealed:

$$d_{33}^{\mathrm{eff}} = d'_{33}\,\delta n + d''_{33} \qquad (3\text{-}10)$$

where d'_{33} = 0.96 (10^{-12} pm cm^2/V) and d''_{33} = −0.63 pm/V. In this manner, the effective piezoelectric strain tensor $d_{33}^{\mathrm{eff}}(V_{\mathrm{dc}})$ also provide a direct measure of local carrier density, and the local carrier density and lattice distortion is connected by $d_{33}^{\mathrm{eff}}(V_{\mathrm{dc}})$.

The calculated surface displacement (Equation 3-6) shows the lattice distortion under dc bias, which is due to both LAO polarization and the interface distortion. The displacement in both sides of the MIT (Fig. 3.14a) is qualitatively different: for negative V_{dc}, the displacement is linear, which means that there is a constant piezoresponse, plausibly from LAO polarization; for positive V_{dc}, the displacement is quadratic, which implies the distortion is associate with the charge accumulation at interface. The contribution from the LAO layer can be estimated by a linear fit in the insulating regime (Fig 3.14a). The interface distortion is obtained by subtracting the LAO contribution (Fig. 3.14b). The calculated dilation $\Delta d'$(V_{dc} = 5V) − $\Delta d'$(V_{dc} = -5V) = 0.11 Å is consistent with previous experimental [125] and theoretical reports [36,84,92].

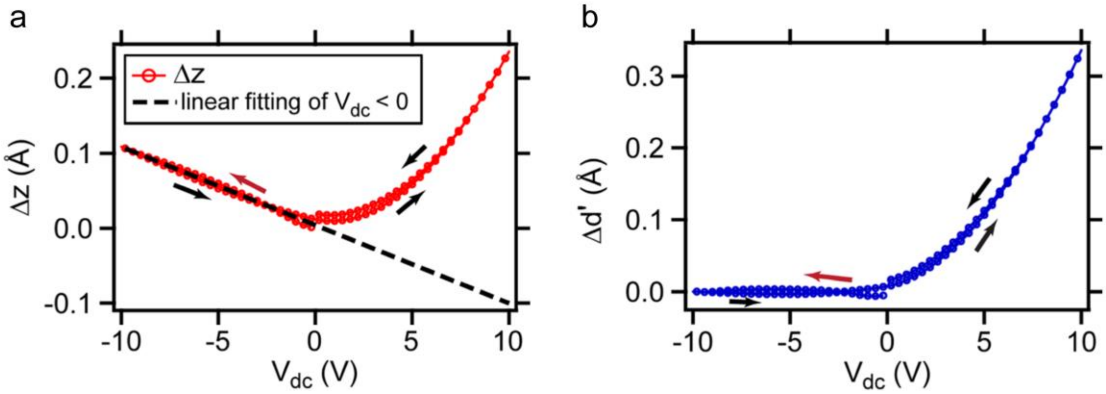

Figure 3.14 Surface displacement calculation. a, Surface displacement (Δz) is calculated and plot as a function of V_{dc}, For $V_{\mathrm{dc}} < 0$ region, the displacement is linear with respect to V_{dc}. The linear response is fitted as the black dashed line. **b,** $\Delta d'$ as a function of V_{dc} acquired from **a** subtracting the linear fitting, which is interpreted as the interface distortion. The red arrow indicates the initial scanning direction.

3.3.5 Simultaneous time-dependent PFM and capacitance measurement

To better understand the relationship between the capacitance and piezoresponse signals, the two signals are measured simultaneously with V_{dc} abruptly changing into or out of the MIT region (Fig 3.15). The piezoresponse is integrated over a frequency band centered on the contact resonance frequency (~270 kHz), while the capacitance is monitored in parallel. Strong correlations exist between the PFM and capacitance signals for each of the voltage ranges explored, further supporting the hypothesis that PFM can be employed as a sensitive local probe of the gate-tuned carrier density.

The capacitance measurement gives us the averaged carrier density of 2DEG under the top gate (~ µm scale). The PFM probes the local (~nm scale) lattice distortions that strongly correlates with the local carrier density. Therefore, the PFM signal (local measurement) shows the similar qualitative trend as the capacitance measurement (averaged results) but not a perfect point-to-point match. To calibrate precisely the conversion between PFM signal and carrier density, local capacitance measurement or transport measurement can be a reliable method but fabricating such small size (~nm scale) device and making electrical contact will be challenging. Although the carrier density is not precisely calibrated, the PFM can still serve as a sensitive and non-volatile way to spatially mapping out the carrier density buried at the oxide interface, e.g., imaging the conductive and insulating nanoscale features at LAO/STO interface with feature sizes as small as 30 nm [69].

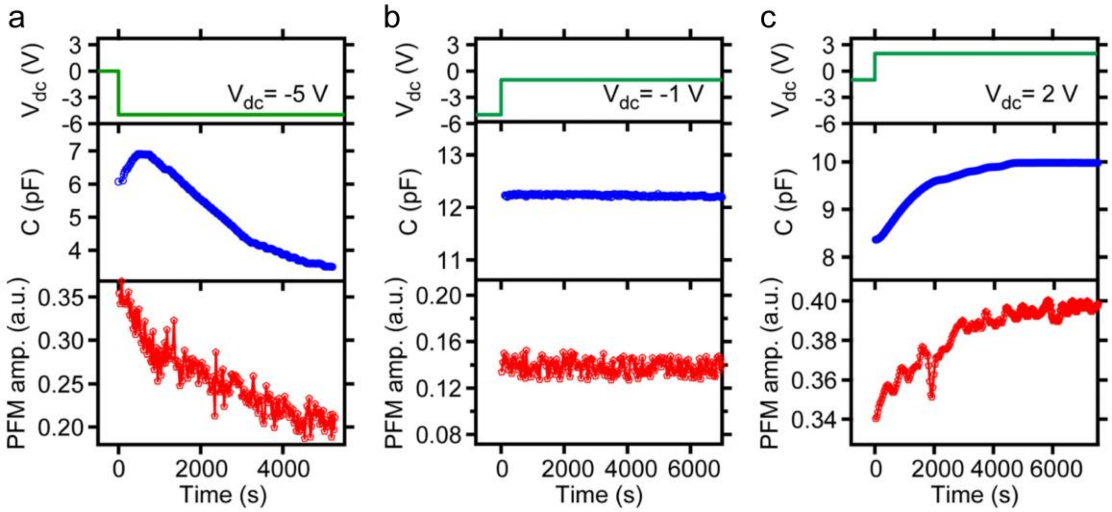

Figure 3.15 Simultaneous time-dependent PFM and capacitance measurements. a, $V_{dc} = -5$ V. **b,** $V_{dc} = -1$ V. **c,** $V_{dc} = 2$ V. Top graph shows the V_{dc} bias history. V_C and V_b are applied at the capacitance bridge frequency 14 Hz. PFM response is measured at a frequency band centered on the contact resonant frequency between 290 kHz and 310 kHz with 200 Hz steps. To avoid the influence of resonance frequency changes, the PFM response is integrated in the frequency band from 290 kHz to 310 kHz.

3.3.6 Time-resolved PFM measurements

A large capacitance enhancement on LAO/STO near the MIT was first reported by Li *et al.* [130]. A strong frequency dependence was observed, with enhanced capacitance values observed for frequencies below ~50–100 Hz. We also perform CV measurements at frequencies ranging from

7 Hz – 100 Hz with an ac excitation voltages V_C = 20 mV and V_{dc} varying from 1 V to −6 V in steps of 0.1 V. When the device is depleted of electrons (V_{dc} decreasing from 0 V to -2 V), a capacitance upturn is observed. AT its peak, the capacitance enhancement is significantly beyond the geometric limit. The capacitance enhancement also shows a frequency dependence (Fig 3.16a). At excitation frequencies above f_C ~70 Hz, the capacitance enhancement decays and vanishes completely by f_C = 1 kHz. This enhancement is not present for positive gate sweeps (Fig 3.16b) and such sweeps were not reported in Ref. [130].

To gain insight into this phenomenon, time-resolved PFM measurements are performed at different tip locations on the devices using a lock-in amplifier with time constant t_c = 1 ms and frequency rolloff 6 dB/oct. An ac excitation voltage V_{PFM} = 20 mV at the resonant frequency together with a step-function pulse (V_{dc} switches between −2 V and +2 V) are applied to the LAO/STO interface. As a reference, the lock-in amplifier response to a sudden amplitude-modulated test wave is shown (bright pink diamond curve in Fig 3.16c and d), confirming that the bandwidth of the instrumentation exceeds that of the sample response by approximately one order of magnitude. Time-resolved piezoresponse (note as $R_{(amp)}$) is turned on and off as a function of the V_{dc} = ±2V pulse (Fig 3.16 c and). Fitting the piezoresponse to an empirical expression:

$$R_{(\mathrm{amp})} = a_1 \times \tanh\left(\frac{t - t_0}{t_1}\right) + a_2 \tag{3-11}$$

yields a characteristic response time $t_c = 1.76t_1$, defined as the full width at half maximum (FWHM) of $dR_{(amp)}/dt$, and corresponding frequency $1/t_c$. The response times in Fig 3.16c and Fig 3.16d are 11 ms and 12 ms respectively, corresponding to $1/t_c$ = 90 Hz and 84 Hz, respectively. These frequencies agree well with the observed frequency response in the CV experiments.

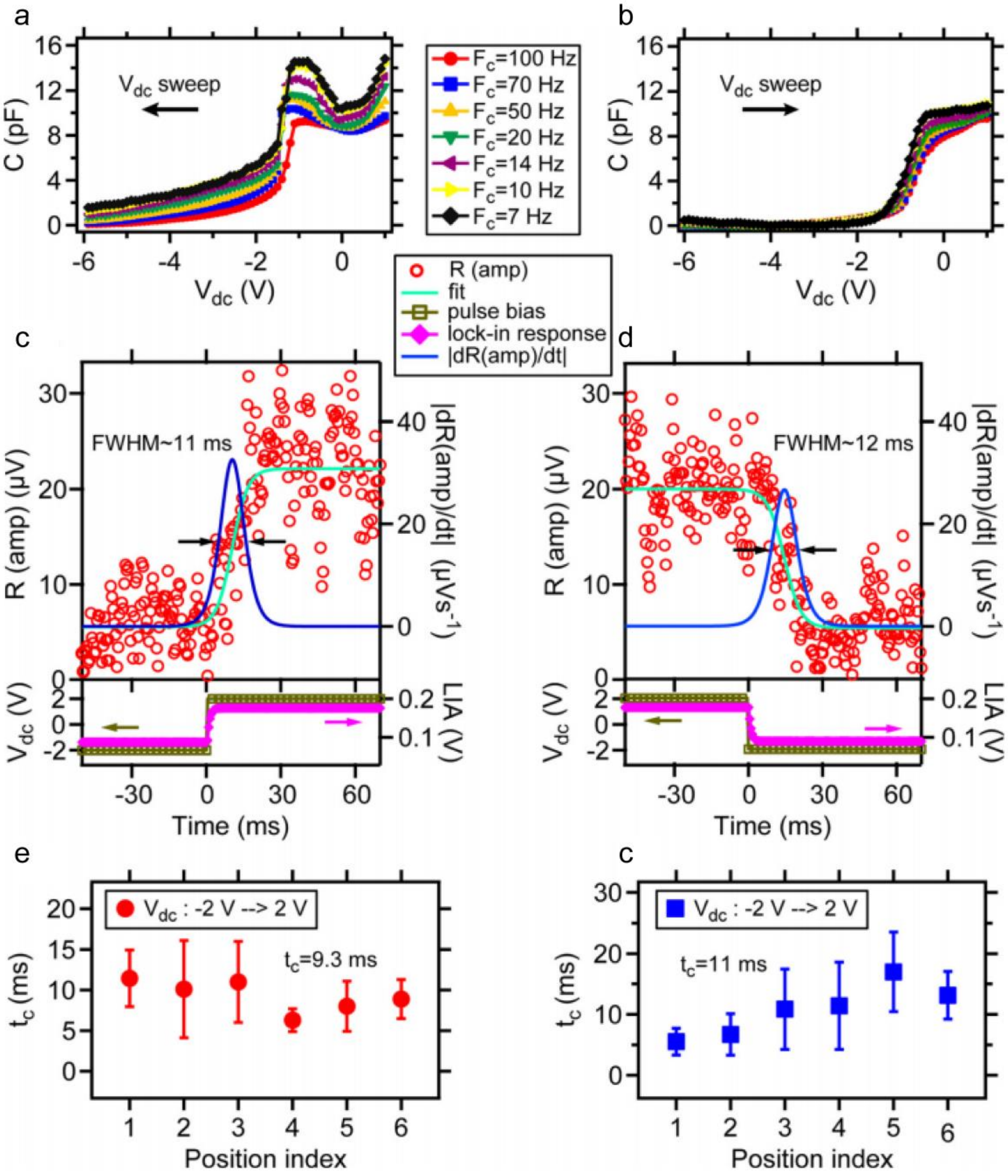

Figure 3.16 Capacitance enhancement and time-resolved PFM analysis. a and **b,** Capacitance is measured as dc bias decreases increases. **c,** Time resolved piezoresponse during an applied step-function dc bias. **d,** Piezoresponse as the V_{dc} bias is removed. Red circles are data and the green line shows a fit to an empirical expression. The lock-in amplifier equipment response time is around 1 ms, obtained from fitting the diamond curves. **e** and **f,** Time resolved piezoresponse analyses at different locations. At each location, measurements are repeated several times, and the mean value and standard deviation are calculated.

The time-resolved piezoresponse measurements are reproducible at different locations on the device. At each location, measurements are performed 5-10 times and the mean value is computed as well as the standard deviation. The mean time for all these investigated locations is 9.3 ms (Fig 3.16e) and 11 ms (Fig 3.16f), which corresponds to ~108 Hz and 91 Hz respectively. Such results also agree with the frequency dependence of capacitance enhancement. Similar results are observed for the other devices.

3.4 CONCLUSION AND DISCUSSIONS

We have performed nanoscale investigations of the hysteretic piezoelectric response at LAO/STO heterostructures using a NL-PFM set-up [67]. The observed PFM response and its sensitivity to both ambient atmospheric conditions and the conductivity of the interface suggest that hysteresis arises from bound states between electrons at the interface and surface adsorbates. The piezoresponse itself most likely originates from Jahn-Teller distortions. The NL-PFM technique constitutes a new experimental probe of electron density and interfacial electronic properties for this class of materials, enabling electronic and structural distortions to be correlated at nanoscale dimensions.

We also use the NL PFM set-up to provide high-resolution and nondestructive imaging of conductive nanostructures at the LAOS/TO interface [69]. These high-resolution PFM images of the nanodevices help to confirm the nanoscale dimensions which are important for further investigations. For example, in transport measurements performed on LAO/STO, the transport channel typically involves nanowire segments created by c-AFM lithography. Correctly measuring the nanowire width can provide important information to help understand the transport properties.

The PFM images consistently show a sub-50 nm width and are well correlated with prior method involving nanowire erasure. The width of a single wire is measured as small as 30 nm before deconvolution. Influence of various c-AFM lithography parameters on the dimensions of nanostructures is also investigated by the PFM imaging. This PFM setup can be used to image a variety of nanoscale devices created by c-AFM lithography, which are buried in the oxide interface with no topographic features.

There are several possible mechanisms that can give rise to the observed electromechanical response. Ferroelectric layers are known to give rise to PFM signals [138] and addition of LAO layers results in ferroelectric-like structural distortions in STO [92,125,126,139]. In addition there are electrochemical processes that should be considered. During c-AFM lithography, surface charging as well as ionic dynamics, both at the surface and in the bulk [56,71,140,141], can take place. This process, alone or coupled with electrostrictive effects of LAO layer [124], can also lead to a measurable PFM response. In previous studies on the electromechanical response of LAO/STO using PFM [56] or electrochemical strain microscopy (ESM) [71], the ac excitation voltage is usually applied on the tip. In that case, surface charging and/or oxygen vacancy formation or migration can produce a PFM response. In Our PFM experiments, the tip is biased only while creating nanostructures. After the c-AFM lithography procedure, the tip is electrically isolated during PFM measurements or imaging. In this regard, it is challenging to imagine a scenario involving electrically induced oxygen vacancy migration or electrostriction in the LAO layer plays a significant role in the observed piezoresponse. In addition, our NL-PFM experiments demonstrate that in air the piezoresponse hysteresis exists even under a complete lack of local driving but vanishes in vacuum [72], which cannot be fully explained by the oxygen vacancy mechanism. Our PFM imaging results are consistent with a carrier-mediated lattice distortion at the LAO/STO interface as the likely origin of the piezoresponse. Furthermore, our combined PFM and capacitance measurements performed on top-gated LAO/STO devices reveal strong correlations between electron and structure degree of freedom [68]. The PFM is performed at relatively high frequencies (~ 290 kHz), whereas oxygen vacancies have too small of a mobility ~10^{-13} cm^2/Vs [142] for the piezoresponse signal to be attributed to oxygen vacancy motion.

Therefore we propose that the piezoresponse is attributed to the carrier-density modulated lattice distortions at the interface, e.g. due to Jahn-Teller effects [128,143]. The electron accumulation on the Ti-3d band at the LAO/STO interface can induce oxygen octahedral distortion, which is supported by both transmission electron microscopy [125] and X-ray [126] measurements. Such lattice distortions at the interface result in a biaxial strain and a strain gradient that can induce ferroelectric [15] and flexoelectric [144] polarization in STO near the interface. Theoretical calculations [36,84,92] of LAO/STO system also reveal carrier-mediated distortions at the interface. The calculated dilation at the interface of about δz = 0.15 Å is consistent with what is calculated from our PFM measurements. Large ferroelectric-like distortions of the TiO_6 octahedra, which substantially affect the Ti d-electron density, are also reported in a theoretical study for $LaTiO_3/SrTiO_3$ superlattices [145].

The Jahn-Teller mechanism also helps to explain the strong correlation between capacitance signal and piezoresponse (Fig 3.13 and Fig 3.15). In the insulating phase (large negative V_{dc}), the capacitance is small and approximately bias-independent. The piezoresponse is similarly small and independent of V_{dc}. As V_{dc} increases, electrons will eventually be introduced to the interface, leading to an enhancement of capacitance signal. These electrons can occupy/evacuate the Ti-3d band at the interface under V_{PFM} modulation, which gives rise to a stronger oxygen octahedra distortion as well as an enhanced piezoresponse signal that scales with the local carrier density [146]. The observed frequency dependence of capacitance enhancement may be understood in terms of an intrinsic time scale for island charging-discharging dynamics. Our PFM experiments on LAO/STO provide a fuller understanding of the interplay between electrons and lattice degrees of freedom, and may help to find more potential applications of oxide-based nanoelectronics.

4.0 ELECTRIC FIELD EFFECTS AND TRANSPORT STUDY IN GRAPHENE/LAO/STO HETEROSTRUCTURES AND NANOSTRUCTURES

We report the development and characterization of graphene/LAO/STO heterostructures. Complex-oxide heterostructures (e.g. LAO/STO) are integrated with graphene using both mechanical exfoliation and transfer from chemical-vapor deposition on ultraflat copper substrates. Nanoscale control of the metal-insulator transition at the LAO/STO interface, achieved using conductive AFM lithography, is demonstrated to be possible through the graphene layer [147]. LAO/STO-based electric field effects using a graphene top gate are also demonstrated. The ability to create functional field-effect devices provides the potential of graphene-complex-oxide heterostructures for scientific and technological advancement.

Integrating graphene into a new substrate can bring us new phenomena of the graphene layer. Here we report clear signatures of weak antilocalization (WAL), a consequence of pseudospin quantum interference, in our graphene field-effect devices on LAO/STO. The WAL signature persists up to room temperature. The pseudospin quantum degree of freedom is one of the most remarkable properties of graphene that distinguishes it from ordinary two-dimensional metals and semiconductors. Pseudospin quantum interference leads to WAL and is influenced strongly by point defects and thermal perturbations that break chirality and destroy phase coherence. Preserving and manipulating quantum transport properties up to room temperature is key to realizing practical pseudospin-based graphene devices. Model fitting of WAL data reveals its origin, as dominant contribution of intra-valley scattering over inter-valley scattering and consistent long scattering lengths up to room temperature, suggesting critical role of the LAO/STO substrate to screen charged impurity scattering and suppress electron-phonon coupling. The observation of quantum transport signatures at room temperature is unique to this system and presents new opportunities for the development of pseudospin-based devices and novel multifunctional devices that couple to the complex-oxide interface.

4.1 BACKGROUND AND MOTIVATION

Two-dimensional graphene and complex-oxide interfaces possess properties that are of tremendous interest for fundamental science and future applications. Single-layer graphene (SLG) is a two dimensional (2D) material with celebrated properties [148-152]. The quasi-two-dimensional interface between two insulating perovskite oxide semiconductors, LAO and TiO_2-terminated STO, has also attracted intense interest in recent years due to its unique electric-field-tunable properties (see Section 1.3). Recent reports have demonstrated that a variety of surface perturbations on LAO/STO, including polar adsorbates [94,103], metal layers [95], metallic nanoparticles [96] and other oxide layers [98,99] can modulate the conductance at the interfacial two-dimensional electron gas (2DEG) between LAO/STO, indicating strong sensitivity of the conducting interface to the surface environment.

The rich properties of both SLG and LAO/STO motivate efforts to create functional hybrid materials that combine the properties of both systems. Graphene has already been integrated with complex oxides [153] to create, for example, graphene/ferroelectric field effect transistors [154] and terahertz plasmonic devices [155]. Proximal coupling of graphene with LAO/STO heterostructures has the potential to create new functionality in each layer due to the small separation between the two layers (less than 2 nm for 3 uc LAO). Novel correlations are expected to develop between the coupled layers, possibly observable through transport. In addition, the unique magnetic and superconducting properties of LAO/STO may interact in new and unexpected ways with the nearby graphene layer. Many practical devices may also be enabled by functional integration of these two materials. For example, LAO/STO interface can potentially serve as an ac ground plane capable of tuning the electrical properties of graphene and potentially reach a quantum-pressure driven regime of 2D plasmonic circuits [156] with potential applications in biosensing, large-molecule spectroscopy, and precision modulation.

One distinctive property of LAO/STO is the existence of a sharp metal-insulator transition (MIT) at a critical thickness of LAO ~ 4 uc, above which the interface becomes conducting. Just below this thickness, ~3 uc, the LAO/STO interface can be locally and reversibly switched between conductive and insulating phases using c-AFM lithography, allowing the fabrication of reconfigurable nanoscale electronic devices. We demonstrate that this technique can also be used to create field effect devices on graphene/LAO/STO heterostructures. Using CVD-grown SLG, combined with lithography method, we can pattern the graphene layer into arbitrary geometry (e.g. Hall bar structure for transport measurement). Our high mobility CVD-grown SLG on LAO/STO exhibits quantum Hall effect and weak antilocalization (WAL) behavior over a broad temperature range, revealing chiral electronic character of CVD-graphene.

4.2 SAMPLE GROWTH AND DEVICE FABRICATION

4.2.1 Exfoliated graphene on LAO/STO

3 uc LAO layers are grown on TiO_2-terminated STO (100) substrates by pulsed laser deposition. The LAO layer thickness is monitored using *in-situ* high pressure reflection high energy electron

diffraction (RHEED) is used to control the LAO thickness. Details of the growth conditions and electrical contacting to the LAO/STO interface are described in section 2.1. SLG layers can be deposited by mechanical exfoliation. After exfoliation, multi-layer and single layer graphene are distributed on the 5 mm × 5 mm LAO surface (Fig. 4.1a). Unlike graphene on SiO_2, graphene on LAO/STO is barely visible under an optical microscope, and it is extremely hard to distinguish single-layer graphene from multi-layer graphene just using optical microscope. Raman microscopy is used to identify SLG candidates by recording the characteristic G and 2D peaks (Fig. 4.1b). Once an area containing SLG is identified, the region is subsequently imaged using non-contact mode AFM (Fig. 4.1c) prior to c-AFM lithography. The height of SLG on LAO/STO is measured to be 0.6 nm from the AFM images, which is generally consistent with AFM results reported by other groups [157,158].

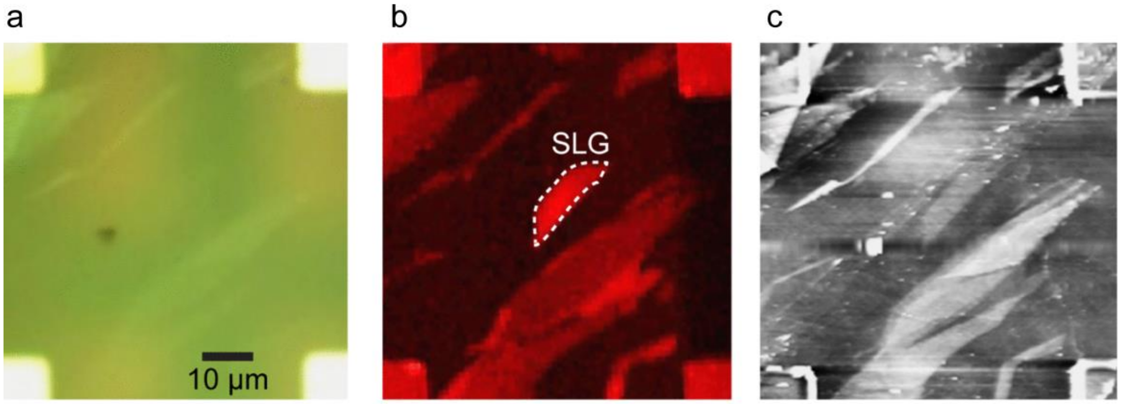

Figure 4.1 Mechanical exfoliation of SLG on LAO/STO. a, Optical image. The four bright corners are Ti/Au electrodes contacting the LAO/STO interface. Multilayer graphene flakes can been seen but barely single layer. **b,** Raman image at G-peak wave length, showing several SLG regions, one of which is identified by a white dashed boundary. **c,** Non-contact AFM topography image of the same area.

4.2.2 CVD-grown graphene on LAO/STO

Although mechanical exfoliation is a simple way to transfer SLG onto LAO/STO, there are many limitations to this approach. SLG on LAO/STO lacks optical contrast, forcing the use of time-consuming Raman mapping to identify suitable regions. Mechanical exfoliation is hard to control the position and uniformity of graphene layers. To overcome these limitations, mm-scale, SLG can also be synthesized using atmospheric pressure chemical vapor deposition (APCVD) growth method [159] on ultra-flat Cu wafers [160] and subsequently transferred onto pre-patterned LAO/STO substrates. Following the synthesis, graphene layer of approximately 4 mm × 4 mm size is transferred assisted by PMMA onto pre-patterned LAO/STO substrates using a wet-transfer procedure, in which the Cu substrates was removed by etching in ~1M ammonium persulphate solution. Prior to the graphene transfer process, the surface of the LAO/STO substrate was cleaned in an oxygen plasma to minimize possible contamination between graphene and LAO surface. Deep-UV lithography and oxygen plasma cleaning were used to selectively remove unwanted graphene. After removal, the remaining circular graphene piece was aligned with the LAO/STO canvases with gold electrodes that independently contact the graphene on the surface and LAO/STO at the interface.

4.2.3 Graphene patterning using negatively biased c-AFM tip etching

After transferring CVD-grown graphene onto LAO/STO, the SLG can be patterned into Hall bars using c-AFM lithography (selectively removing graphene area by a biased c-AFM tip in contact mode). We used an AFM system (Asylum Research MFP-3D) with an environmental closure with controlled humidity (~ 30 %). A conductive Si tip was used for both imaging and lithography.

Imaging was performed in non-contact (tapping) mode and lithography was performed in contact mode. Electrically isolated graphene layer is etched out or cut by using a c-AFM lithography (Fig. 4.2a). A negative bias voltage (amplitude ~ − 25 V) was applied to the tip to sufficiently locally etch out the graphene surface. Graphene conductance (between the electrodes) is monitored during lithography process, which provides confirmation of electrical isolation once patterning was done across the graphene. In a test of the lithography process performed on a graphene/LAO/STO sample, the graphene stripes are patterned on LAO/STO connecting with gold electrodes. The conductance drops sharply (Fig. 4.2b) as soon as graphene is detached or etched away as shown by the arrow (Fig 4.2c).

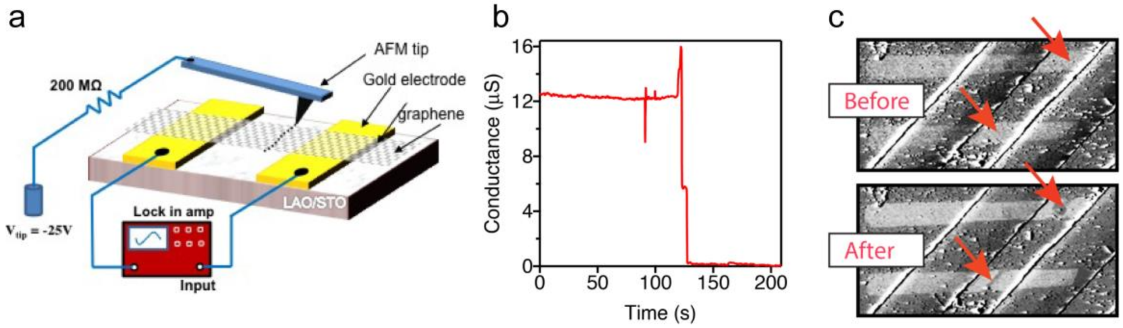

Figure 4.2 Graphene patterning by c-AFM lithography. a, Schematic view of a test sample for c-AFM lithography in which graphene is contacted by top-gated gold electrodes on an LAO/STO heterostructure. **b** and **c**, Experimental demonstration of graphene patterning by c-AFM lithography on a graphene/LAO/STO sample. Conductance between the two electrodes drops to zero as soon as graphene is etched out. Tapping mode AFM images acquired before and after the lithography process show complete breaking of graphene along the written path, as indicated by the red arrows.

The AFM lithography method was applied to pattern several Hall bar devices (Fig. 4.3). Since this method can be automated to create a variety of shapes such as lines, rectangles, circles, and also a single dot via pulsed voltage, it is very useful to fabricate various types of nanostructures or quantum devices without undergoing additional processing steps such as electron-beam lithography and/or etching. The channel width of the Hall bar devices can be controlled by manipulating the tip movement. A nominal channel length of *L* = 3 μm and width of *W* = 5 μm, as measured from the center of the voltage probe, is used for transport measurements.

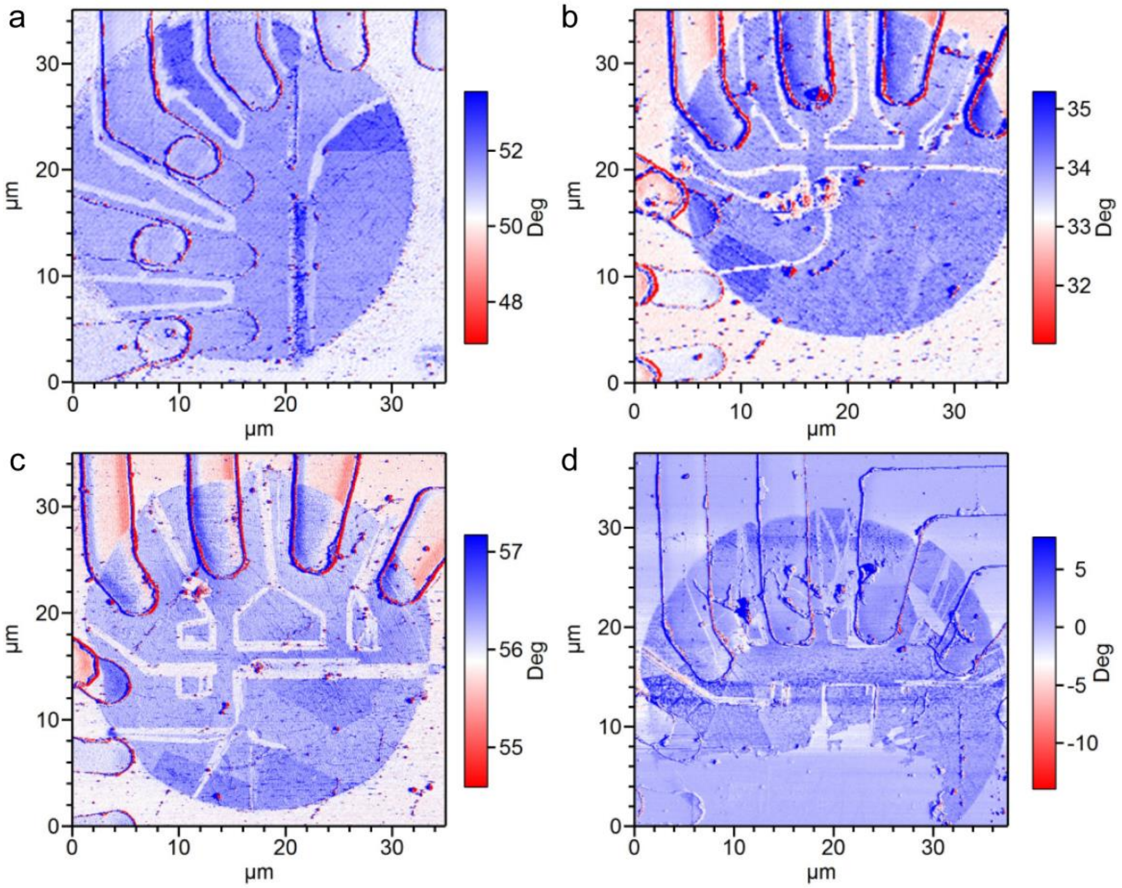

Figure 4.3 AFM patterned Hall bar devices on graphene/LAO/STO. a to **d,** Tapping mode AFM phase images of patterned graphene/LAO/STO hall bars of different widths and lengths. Because of high contrast between graphene/LAO/STO and bare LAO/STO surface, phase images are chosen to show here. Brighter region is LAO/STO surface where graphene is etched out by using c-AFM lithography. We can also recognize multilayer graphene (dark blue regions), which is otherwise difficult to recognize in height images. Device **c** has multilayer graphene directly on the device channel, demonstrating that this technique is equally applicable for multilayer graphene devices.

4.3 GRAPHENE/LAO/STO CHARACTERIZATION

4.3.1 Surface roughness

The surface morphology of graphene/LAO/STO is characterized by AFM in tapping mode. The vertical resolution of our AFM is sub-angstrom, which is estimated by resolving the uniform atomic steps on a pristine LAO/STO sample. A doped Si tip with tip radius of 5 nm was used for AFM imaging therefore the lateral resolution has lower limit around 5 nm. To avoid any differences caused by the scanning process, identical scanning parameters are used to acquire AFM scans on both surfaces. The AFM images are corrected by third order plane subtraction to compensate for the scanning drift.

Surface morphology of graphene/LAO/STO and bare LAO/STO is compared by calculating the standard deviation of the height distribution [161]. Height analysis is performed within a scan size of 2 μm. Although both surfaces show uniform atomic steps, the LAO/STO region covered by graphene (Fig. 4.4b) has a reduced RMS roughness compared with the bare LAO/STO surface (Fig. 4.4a). Height histograms obtained from both surfaces were fitted using Gaussian distributions and standard deviations σ_{std} were determined from best-fit conditions (Fig. 4.4c). To avoid any influence from the surface roughness on pristine LAO/STO surface, we have also plotted histograms after masking the regions covered by the atomic steps (inset of Fig. 4.4c). Both results are summarized in Table 1. It is to be noted that σ_{std} of our graphene/LAO/STO samples (with masking) is appreciably lower than σ_{std} estimated on good quality graphene/SiO_2 samples [161,162], confirming improved surface corrugation in our graphene/LAO/STO samples.

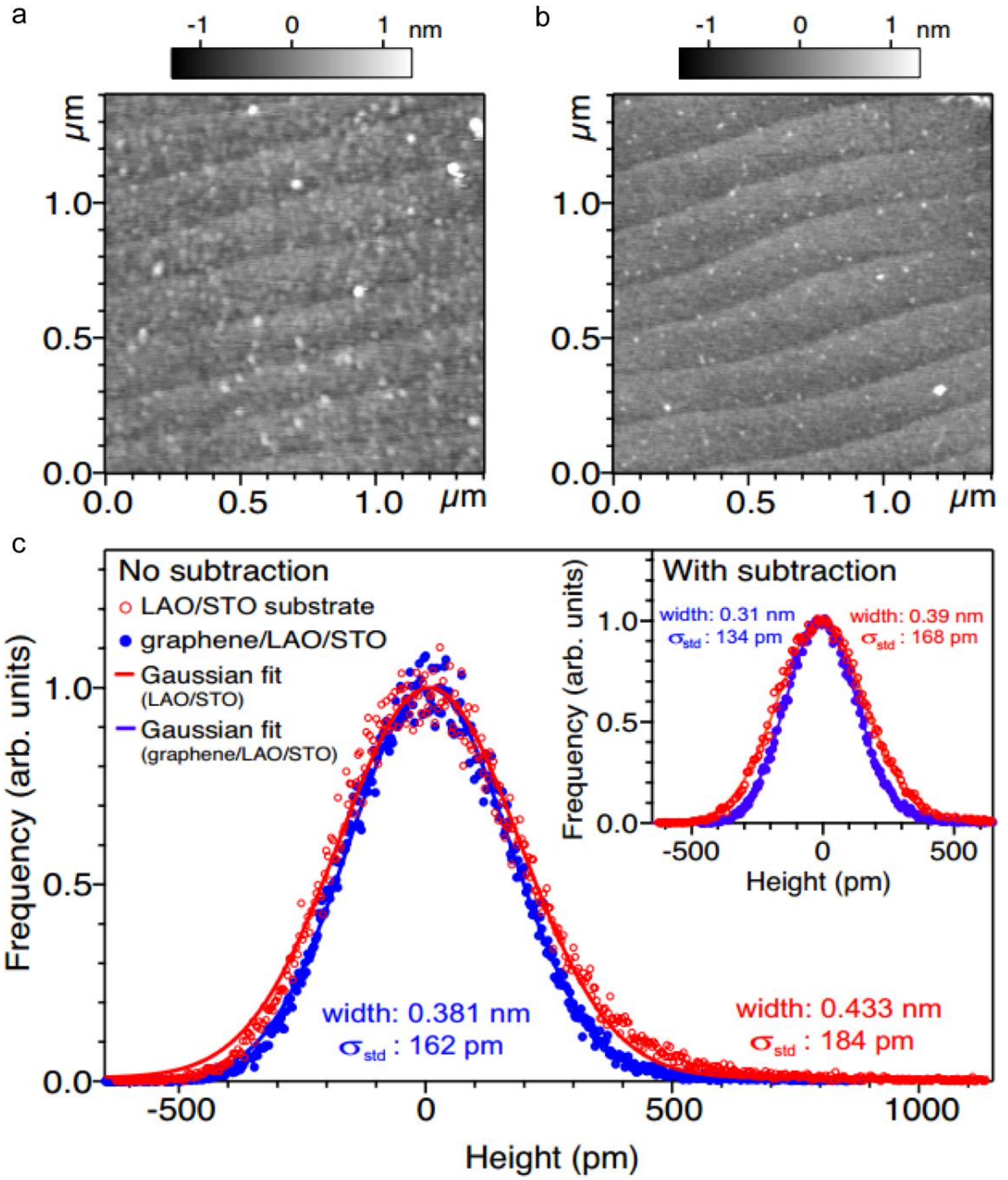

Figure 4.4 Comparison of surface morphology of bare LAO/STO and graphene/LAO/STO. Tapping mode AFM height images of **a** bare LAO/STO and **b** graphene/LAO/STO surfaces. Both images are presented with the same height scale. **c,** Height histograms of the data in **a** as red open circles and in **b** as blue filled circles. Inset shows the respective histogram data after masking the regions covered by atomic steps of underlying LAO/STO substrate.

Table 4-1 Standard deviation and width of the height histogram for different surfaces.

	LAO/STO (with steps)	Graphene/LAO/STO (with steps)	LAO/STO (no steps)	Graphene/LAO/STO (no steps)
σ_{std}	184 pm	162 pm	168 pm	134 pm
Γ_{width}	0.43 nm	0.38 nm	0.39 nm	0.31 mm

4.3.2 Raman spectroscopy

Raman measurements are performed on graphene/LAO/STO and bare LAO/STO using a commercial Raman microscope (Renishaw InVia) with 633 nm laser excitation under ambient conditions. The spectral resolution of the instrument is approximately 1 cm^{-1}. We use a 50× microscope objective (numerical aperture NA = 1.4) and laser power of ~7 mW. Slightly higher laser power is necessary to collect better spectra because of the transparent substrate. Raman spectra are acquired at different positions on the sample and several acquisition cycles are repeated at each spot to check possible damage caused by laser-induced heating effects. No drastic change in Raman intensity of prominent peaks confirmed negligible heating effect in our samples. Surface morphology was re-examined around the laser exposure region by using non-contact AFM scanning and found no evidence of surface degradation.

Typical Raman spectra (Fig. 4.5) are consistently reproduced at each region on the sample. On the graphene/LAO/STO regions, sharp G- and 2D-peaks are visible in addition to broad peaks at 1320 cm^{-1} and 1610 cm^{-1}. Those broad peaks are also reproduced in the spectrum recorded on bare LAO/STO, indicating that their origin is purely coming from LAO/STO. Those peaks are indeed second-order Raman peaks of STO, as expected from its cubic perovskite structure [163].

To separate the Raman peaks arising only from the graphene layer (net spectrum), the spectrum recorded on bare LAO/STO is subtracted from the spectrum recorded on graphene/LAO/STO, assuming no interaction between them (black solid line Fig 4.5). The net spectrum displays prominent phonon modes of graphene, i.e., G- and 2D-modes. The absence of a D-mode peak at 1350 cm^{-1} indicates very low defect density in our samples. Both G-mode and 2D-mode peak positions and their widths are analyzed by fitting with a Lorentzian function. G-mode peak appears at around 1586 ± 1 cm^{-1} with a FWHM = 7.5 ± 1 cm-1 and 2D-mode peak appears at 2645 ± 1 cm-1 with a FWHM = 24.5 ± 1 cm^{-1}. The error bars are estimated by averaging different spectra acquired from different positions on the sample. The intensity ratio between G-mode and 2D-mode peaks is estimated to be $I_{2d}/I_G \sim 3.8$ and is even higher for some samples. The G-mode peak is upshifted by ~ 6 cm^{-1} and 2Dmode is down shifted by ~ 35 cm^{-1} as compared to the Raman modes from undoped pristine graphene; an opposite shift of the G and 2D peaks corresponds to electron doping of the graphene [164,165]. Since the ratio between G and 2D peak intensities is relatively larger than typical CVD-grown graphene on SiO_2 samples, we can qualitatively estimate very low doping density. In addition, the intensity variation is always $I_{2d}/I_G > 3$ and the 2D-mode shows a single Lorentzian profile, providing confirmation of single layer graphene in our samples.

We observe an asymmetric line shape of the G-mode peak in the subtracted spectrum. The observation of a Fano-like asymmetric line shape could be due to phonon renormalization via coupling with photo induced rapid polarization fluctuations in underlying substrate [166]. This observation also provides interesting prospects for future investigations in this system.

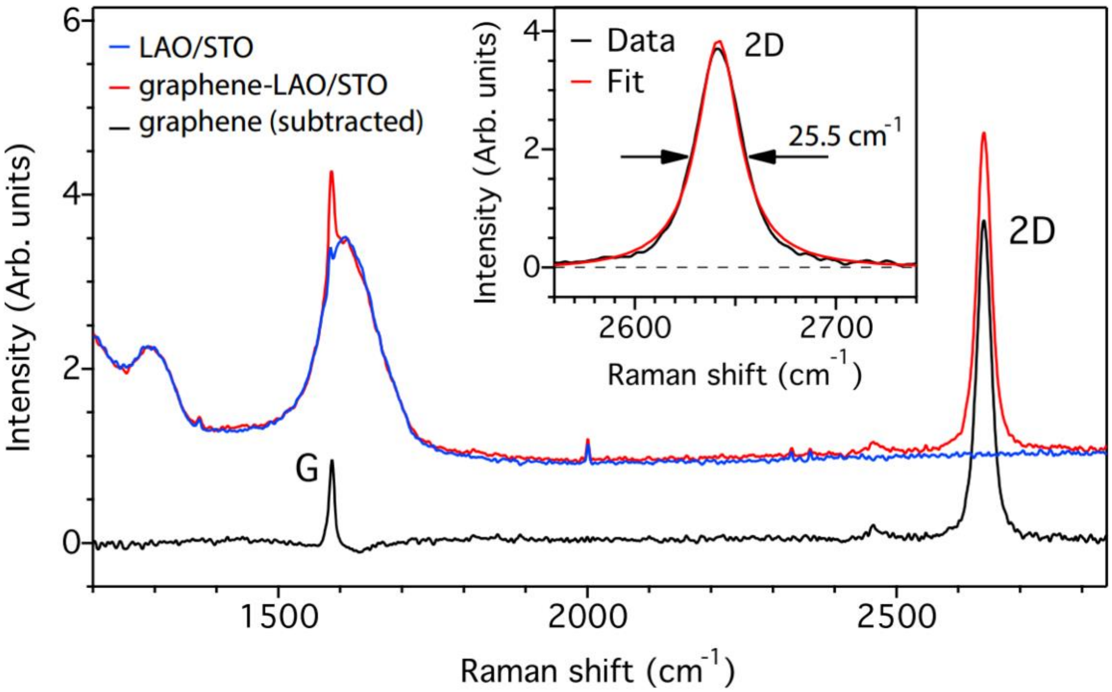

Figure 4.5 Raman spectra of graphene/LAO/STO. Raman spectra measured on graphene/LAO/STO and bare LAO/STO regions on the sample surface for an excitation wavelength of 633 nm. Sharp peak at 1586 cm^{-1} and a single Lorentzian peak at 2645 cm^{-1} on graphene/LAO/STO region correspond to the typical G-mode and 2D-mode optical phonon in graphene. Additional two broad peaks at around 1320 cm^{-1} and 1610 cm^{-1} correspond to the second-order Raman modes of STO. Net graphene spectrum, extracted by subtracting two spectra, is shown with solid black line. It is clear from the subtracted spectrum that there is no measurable D peak, indicating low defect density in graphene.

4.4 C-AFM LITHOGRAPHY ON GRAPHENE/LAO/STO

C-AFM lithography is performed on the SLG/LAO/STO structures. “Virtual electrodes” are created using a tip voltage V_{tip} = 15 V to form robust electrical contact to the oxide interface, followed by a straight line from one electrode to another (V_{tip} = 15 V, tip speed v_{tip} = 1000 nm/s) and intersecting the electrically isolated SLG region (Fig. 4.6a). All of the AFM lithography procedures described in this paper are performed under ambient environmental conditions with a highly doped Si tip (spring constant k = 3 N/m). When the positively biased tip reaches the second electrode, the conductance abruptly increases (Fig. 4.6b), indicating that the c-AFM written area that overlaps the SLG is conductive. After writing, the nanowire is "cut" over the SLG region by applying a negative voltage to the tip ($V_{tip} = -15$ V) and slowly traversing the nanowire ($v_{tip} = 10$ nm/s) (Fig. 4.6c). As the tip passes over the nanowire, the conductance drops sharply to zero (Fig. 4.6d). By fitting the conductance profile, an estimate for the nanowire width $w = 18$ nm is obtained. The conductance increase (~ 75 nS), non-exponential decay after writing, and estimated wire width are comparable to the results of c-AFM lithography on regular LAO/STO that does not contain graphene. C-AFM lithography with $V_{tip} = 15$ V is also performed on multilayer graphene (~ 4 nm thickness) covered area (Fig. 4.6e); however, no conductance jump (Fig. 4.6f) is observed.

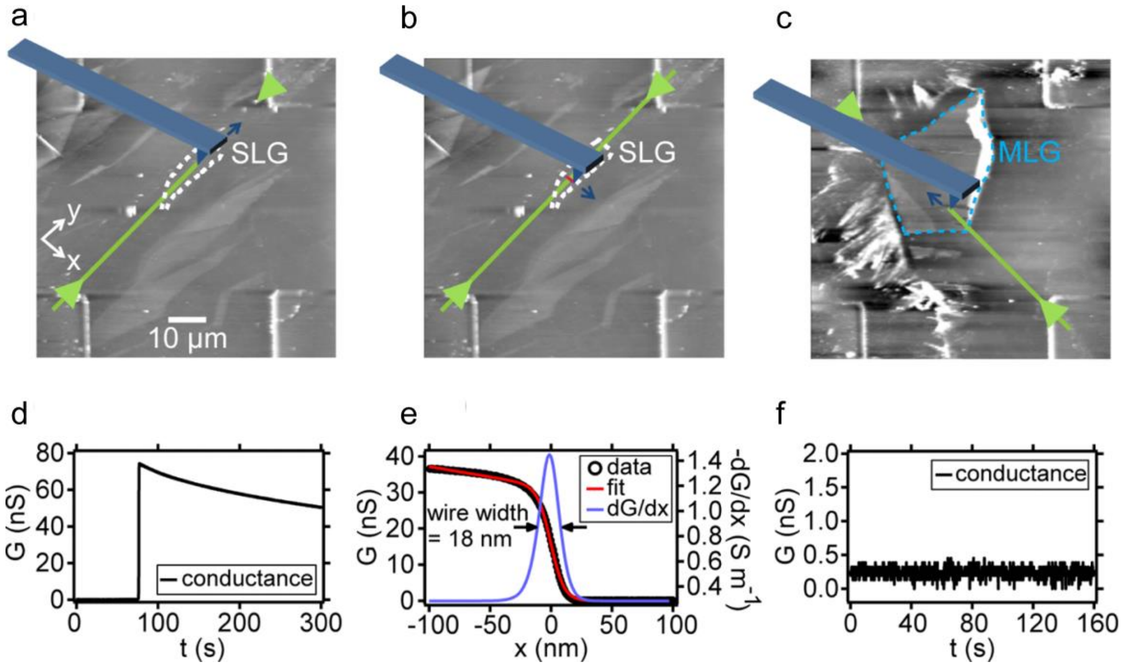

Figure 4.6 C-AFM lithography on mechanically exfoliated SLG/LAO/STO. a, written nanowire across the SLG region with $V_{\text{tip}} = 15$ V and $v_{\text{tip}} = 1000$ nm/s. **b,** Conductance versus time between the two Ti/Au electrodes during the writing. The conductance abruptly increases when the positively biased tip reaches the second Au electrode. After writing, the conductance decays non-exponentially. **c,** The existing wire is "cut" through the SLG region with $V_{\text{tip}} = -15$ V and $v_{\text{tip}} = 10$ nm/s. **d,** Conductance versus position during the cut. The conductance drops to zero when the

negatively biased tip moves across the wire. The conductance profile is fit using $G(x) = G_0 - G_1\tanh(x/h)$. The deconvolved differential conductance dG/dx shows a full-width at half-maximum (FWHM) of 18 nm, which is used to quantify the width of the written wire. **e,** Attempt to write through multilayer graphene (MLG) with V_{tip} = 15 V and v_{tip} = 1000 nm/s, along with **f.** conductance profile during writing. No conductance increase is observed.

One potential concern is that the c-AFM lithography may damage or chemically modify the graphene layer. To address this question, Raman spectroscopy is performed over regions that have been exposed to c-AFM lithography and compared with unexposed regions. The excitation laser (wavelength λ = 633 nm) is focused using a lens with numerical aperture NA = 1.4 to a spot size of $d \approx 550$ nm. The focused laser spot is scanned across the graphene region (Fig. 4.7a). The step size between adjacent scans is 200 nm. Graphene and STO share spectral features in the range of 1200-1800 cm^{-1}, so subtraction from a region not containing graphene is required (Fig. 4.7b). A Lorentzian fit is performed to retrieve the peak position. A clear G peak at 1580 cm^{-1} and 2D peak with much stronger intensity at 2630 cm^{-1} is observed with no discernable D peak, supporting the claim that the SLG on LAO/STO is not measurably damaged by c-AFM lithography. A sequence of Raman spectra is taken over the path (Fig. 4.7a). The G and 2D peak intensities decrease and eventually become zero as the laser spot moves out of the graphene layer (Fig. 4.7c). The spectra taken over the c-AFM exposed and unexposed areas are indistinguishable, and neither shows a measurable D peak, which is a sensitive measure for alteration of sp2 carbon bonding.

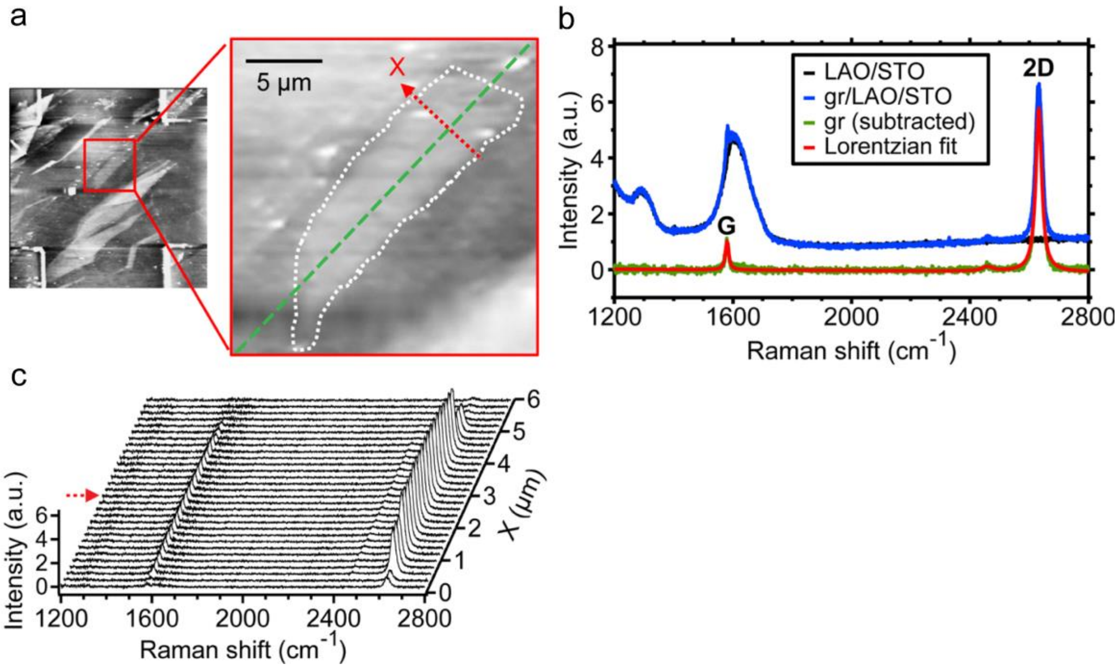

Figure 4.7 Raman spectroscopy of exfoliated SLG/LAO/STO after c-AFM lithography. a, Schematic showing the written wire (green dashed line) and the path (red dashed line with arrow) of the scanned Raman laser spot. **b,** Representative Raman spectra data when the laser spot overlaps the wire previously created by c-AFM lithography. **c,** Raman spectra at different positions along the path "X" (indicated **a**). The red arrow points out the representative data shown in **b**.

C-AFM lithography is also performed on CVD-grown SLG covered LAO/STO. The nanoscale control of the MIT through the SLG covered region works in a manner similar to mechanically exfoliated SLG. Fig. 4.8a shows a region of a LAO/STO canvas that contains CVD-grown SLG. Unlike the experiments performed on exfoliated graphene, here, the graphene is electrically connected to an Au electrode. The two-terminal conductance, tip voltage, and graphene gate voltage are recorded as a function of time during the entire lithography procedure (Fig. 4.8b). While writing the wire, the c-AFM tip is positively biased (V_{tip} = 20 V) and the graphene is grounded (V_g = 0 V). A conductance jump is observed when the wire path is finished. After writing, the graphene is kept grounded (V_g = 0 V) and the tip is held at V_{tip} = −15 V to cut the wire on graphene ("cut 1"). The conductance drops to zero as the tip crosses the written nanowire.

Afterwards, tip voltage is kept at 0 (V_{tip} = 0 V), and increasingly, positive gate voltages are applied to the graphene (V_g = 2 V, 5 V, 8 V). The two-terminal conductance shows a discrete jump associated with the graphene voltage steps, demonstrating that the LAO/STO nanowire junction conductance can be modulated using the SLG top gate. At the end of the experiment, the nanowire circuit is cut ("cut 2,") outside the graphene region, verifying that the conductance measured is taking place through the nanowire and not a distinct parallel path. Fig. 4.8c shows the channel conductance of a similar nanowire device written over the same canvas only after cutting on the graphene region (similar to "cut 1"). The two-terminal conductance of the graphene/complex oxide field effect transistor (GCO-FET) channel as a function of graphene gate voltage shows a "turn-on" near V_g = 6 V (Fig. 4.8c inset). The observation that the subsequent gate sweeps do not overlap reflects the time-dependent decay of the conductance of the LAO/STO nanowires.

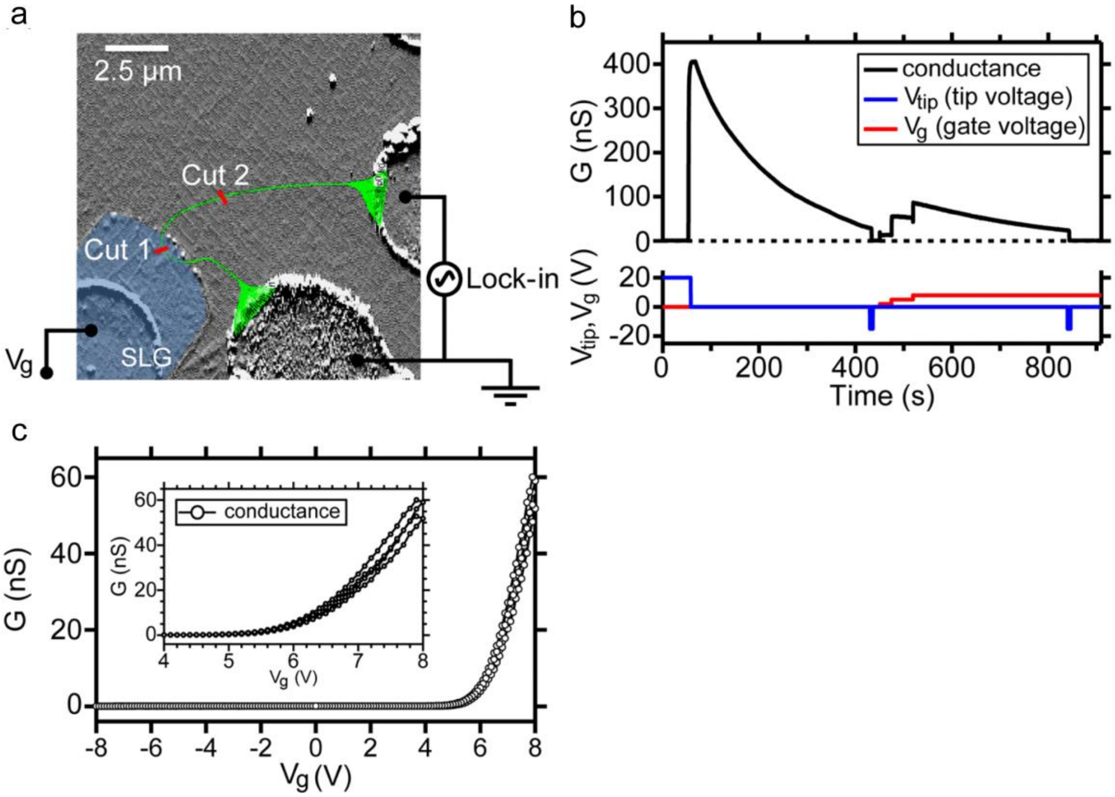

Figure 4.8 C-AFM lithography on CVD-grown SLG/LAO/STO. a, Schematic of lithography pattern overlaid on non-contact AFM image. A path connecting two electrodes crosses the SLG region. Two cuts, one on the graphene region and the other outside the graphene are executed after writing the nanowire. The SLG contacts a third Ti/Au electrode, which is used to bias the SLG. **b,** Monitored conductance G, tip voltage V_{tip}, and gate voltage V_g versus time during the c-AFM lithography process. **c,** Conductance G of the resultant GCO-FET action as a function of V_g.

4.5 ROOM-TEMPERATURE QUANTUM TRANSPORT SIGNATURES IN GRAPHENE/LAO/STO HETEROSTRUCTURES

Integrating graphene with various functional materials provides opportunities to develop multifunctional devices as well as to explore intrinsic graphene quantum transport phenomena. Among multi-functional materials, the complex-oxide heterostructure LAO/STO has attracted great interest because of the intriguing physics discovered at the interface. Since the coexistence of multiple phases in oxide heterostructures is largely associated with a manifold of electronic degrees of freedom and strong correlations between them, unique interactions with the nearby graphene layer may be expected.

We have demonstrated that the c-AFM lithography technique can be used to create devices on graphene/LAO/STO, e.g. Hall bar structures (Fig. 4.3). These devices exhibit quantum transport signatures such as anomalous quantum Hall effect and weak antilocalization (WAL) behavior over a broad temperature range. Remarkably, the mobility is only weakly dependent on temperature (up to 300 K), suggesting weak coupling with optical modes in the substrate. The unique interaction with the oxide heterostructure is associated with direct observation of pseudospin chirality via WAL at room temperature in CVD-grown graphene. We investigate WAL via magnetotransport measurements as a function of carrier density and temperature. We will restrict our focus to transport in the graphene, which is electrically isolated from the LAO/STO interface.

I collaborated with Dr. Giriraj Jnawali on this project. I fabricated the devices, evolved in the device characterization and the transport measurements. I also contributed to the data analysis and manuscript writing.

4.5.1 WAL in graphene

Weak localization (WL) and weak antilocalization (WAL) are quantum interference effects [167-170] resulting from electron phase coherence and spin-orbit interactions in 2D electron systems. WL results from constructive interference between pairs of time-reversed closed-loop electron trajectories and provides a positive correction to the magnetoresistance [168,170]. Spin-orbit coupling (SOC) breaks time-reversal symmetry of scattered electrons and results in destructive interference, leading to WAL and a negative correction to the magnetoresistance [169].

The intrinsic SOC of graphene is weak [171]; however, the electron wave function in graphene carries a pseudospin quantum degree of freedom with π-Berry phase at each Dirac cone [149,157] due to the honeycomb lattice being comprised of A and B sublattices (Fig. 4.9a and b). Because of the pseudospin symmetry, destructive interference between electron wave functions in a closed quantum diffusive path suppresses backscattering, which is analogous to the role of SOC (Fig. 4.9c and d). WAL is theoretically expected in graphene if the intervalley scattering is sufficiently weak [172]. Most studies have not presented clear evidence of WAL [173-175], most likely due to point defects that locally break the sublattice degeneracy and smooth out π-phase contribution. Experimental signatures of WAL observed in high quality epitaxial graphene samples are attributed to suppressed point defects [176]. Interestingly, a WL to WAL transition is also achieved in exfoliated samples [177] by decreasing the carrier density and slightly increasing the temperatures.

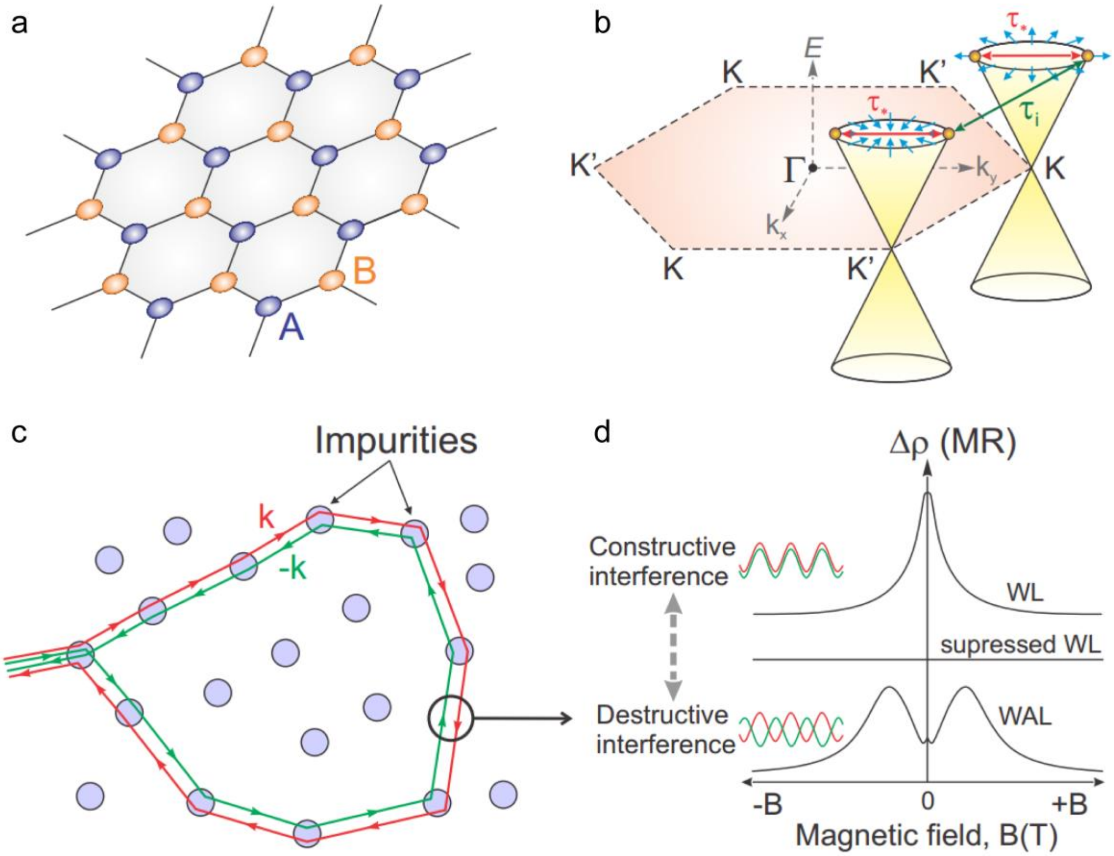

Figure 4.9 Schematic illustration of quantum interference mechanism in graphene. a, The honeycomb lattice of graphene is composed of two equivalent triangular carbon sub-lattices denoted by "A" and "B" with two different colors. **b,** Graphene Fermi surface and low-energy band structure at each sub-lattice in the vicinity of K and K' points of Brillouin zones. Blue arrows directing inward and outward on the Dirac cones are denoted as pseudospin symmetry at each equivalent point. Solid green (red) lines indicate intervalley (intravalley) scattering with scattering rates τ_i (τ_*). **c,** Schematic view of two time-reversed electron trajectories in a closed quantum diffusive path. **d,** Typical magnetoresistance behavior in graphene due to the interplay of intervalley and intravalley scattering processes and the resulting interference effects. Suppressed backscattering via destructive interference will lead to weak antilocalization (WAL) in high quality graphene. In the presence of point defects, chirality-breaking intervalley scattering contribution dominates, which results in suppressed or usual weak localization (WL) in moderate-quality graphene samples.

Pseudospin degrees of freedom observed in graphene can be utilized to store and manipulate information, which is analogous to the spin degree of freedom in spintronics [178-181]. Preservation of pseudospin quantum interference up to room temperature is of fundamental importance for a variety of proposed applications, but thermal perturbations typically suppress the phase coherence and hinder practical use of the devices. Room temperature operation can be achieved if the high graphene mobility is consistently maintained over a broad temperature range by suppressing intervalley scattering (i.e., point defects) and phonon scattering contributions. The mobility of graphene field-effect devices fabricated on SiO_2/Si substrates is typically reduced at room temperature due to scattering with surface polar modes [175,182,183]. A significant improvement in quality was achieved by fabricating graphene devices on hexagonal-boron nitride (hBN) due to the extremely flat surface and strong in-plane bond of hBN [184]. Similarly, high quality graphene field-effect devices were realized using high-κ ferroelectric substrates [185], which also resulted in novel graphene-based non-volatile memory devices. To our knowledge, WAL is not observed at RT in these hybrid structures.

4.5.2 Device structure and field-effect gate tuning.

Graphene samples are patterned into Hall bars with nominal channel lengths of L = 3 μm and widths of W = 5 μm (Fig. 4.10a) by anodic etching using c-AFM lithography [186,187]. Four-terminal longitudinal and transverse resistances are measured simultaneously using low frequency (1-10 Hz) lock-in detection. The carrier density is tuned by either side gate voltages (V_{sg}) or back gate voltages (V_{bg}) applied through the interface or back of the oxide substrate, respectively. The gate dependence of longitudinal resistivity (ρ_{xx}) exhibits standard ambipolar characteristics (Fig. 4.10b), with resistivity modulation ratio more than five at 300 K and twenty at 2 K.

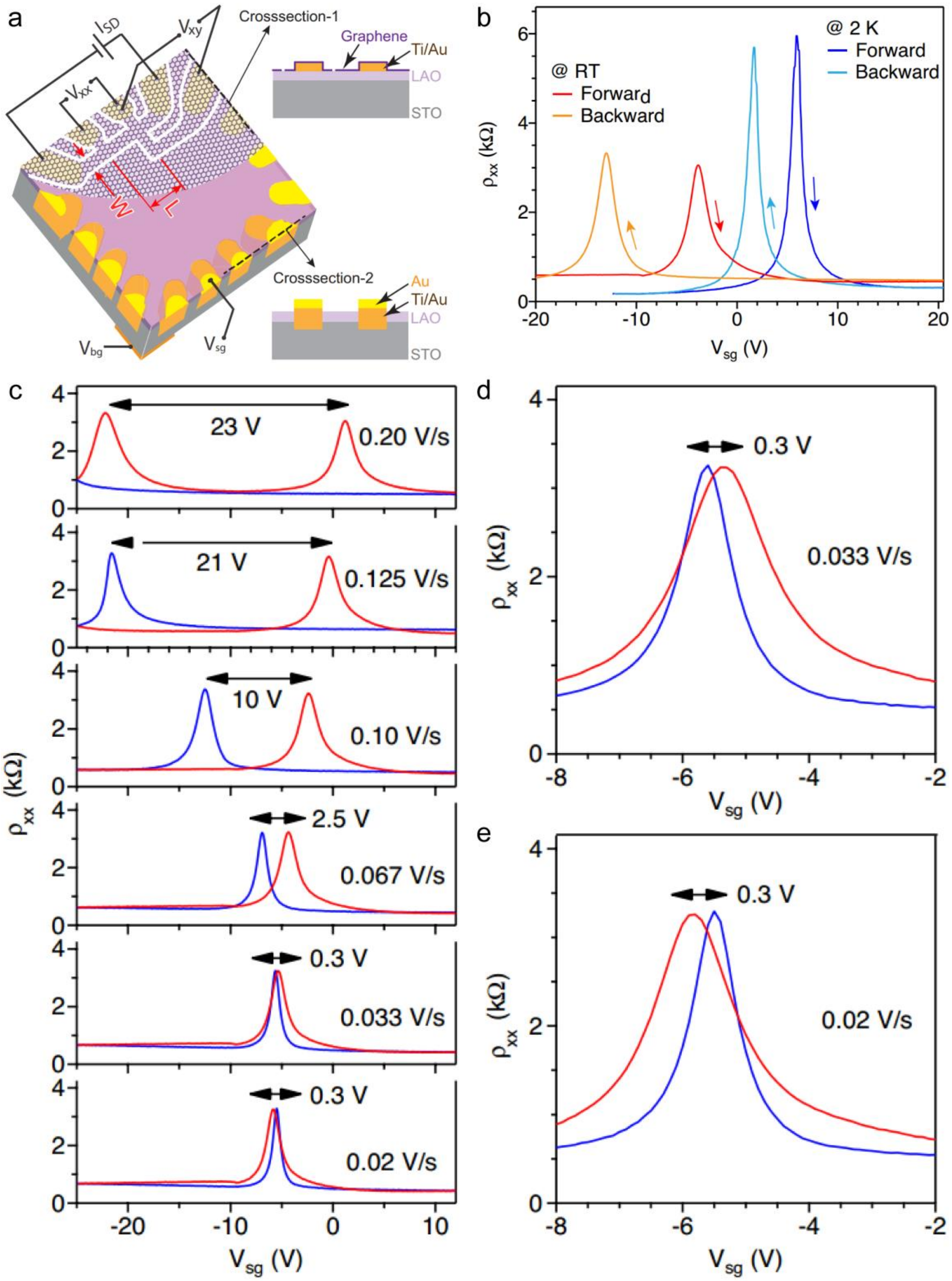
a
I_{SD}
V_{xy}
V_{xx}
W
L
Crosssection-1
Graphene
Ti/Au
LAO
STO
Crosssection-2
Au
Ti/Au
LAO
STO
V_{bg}
V_{sg}
b
@ 2 K
Forward
Backward
@ RT
Forward
Backward
ρ_{xx} (kΩ)
V_{sg} (V)
c
23 V
0.20 V/s
21 V
0.125 V/s
10 V
0.10 V/s
2.5 V
0.067 V/s
0.3 V
0.033 V/s
0.3 V
0.02 V/s
ρ_{xx} (kΩ)
V_{sg} (V)
d
0.3 V
0.033 V/s
ρ_{xx} (kΩ)
V_{sg} (V)
e
0.3 V
0.02 V/s
ρ_{xx} (kΩ)
V_{sg} (V)

Figure 4.10 Device schematic and side gate tuning of longitudinal resistivity.a, Schematic view of graphene/LAO/STO field-effect device and transport measurement. A Hall bar geometry is fabricated by selective removal of the graphene (indicated by white regions) using c-AFM lithography. Graphene is connected only with top-gated Au-electrodes on LAO/STO (upper-half, crosssection-1). Lower-half Au-electrodes are connected with interface (crossection-2), which allow gating graphene through side-gate V_{sg}. **b,** Graphene sheet resistivity ρ_{xx} as a function of V_{sg} at room temperature (RT) and 2 K. **c,** Change of Dirac point shift as a function of sweep rate. As the sweep rate is decreased, the Dirac point shift decreases significantly and even goes to negative shift. **d** and **e,** Close-up plots for two lowest sweep rates, 0.033 V/s and 0.02 V/s, respectively. Negative shift of dual Dirac points can be identified from their asymmetric shape as they shift from positive to negative.

We observe a ferroelectric-like hysteresis in which the Dirac point shifts after reversal of the gate sweep direction. The voltage hysteresis at the Dirac point varies with sweeping parameters such as sweep range and rate. In general, the hysteresis increases as the sweeping range and the rate increase (Fig 4.10 c-e). At a fixed sweep rate and sweep range, the hysteresis stays unchanged and is reproduced consistently during the measurements.

A similar hysteretic effect was previously observed in graphene devices on ferroelectric substrates [188] and was attributed to the response of ferroelectric polarization switching. Graphene devices on STO also exhibited identical hysteresis behavior and it was argued that the surface dipole moment associated with a puckered oxygen layer on the STO surface was responsible for the hysteresis [189,190]. Since our graphene devices are fabricated on top of LAO, both scenarios are unlikely to apply to our samples. Direct electrochemical doping due to charged polar molecules (e.g., H_2O and O_2) on graphene [191,192] also has a minimal effect in our devices because our samples are annealed electrically by passing large currents (~150 nA) for several hours at 350 K under moderate vacuum (1 − 10 Torr) before performing transport measurements. In addition, AFM analysis shows a clean graphene surface without any layers or clusters of water molecules (Fig 4.4). More evidence comes from Raman data and Hall measurements at room temperature, which show slight electron doping in our samples in contrast to the expected hole doping from adsorbed water molecules. Therefore, based on experimental observations, it is reasonable to associate the observed hysteretic behavior in graphene with previously reported field-induced hysteretic conductance of critical thickness LAO/STO interfaces [48]. A clearer understanding of the origin of the observed hysteresis will require more detailed investigations.

4.5.3 Magnetotransport properties and Quantum Hall effect

In a magnetic field applied perpendicular to the graphene basal plane, the device exhibits characteristic oscillations in longitudinal resistivity ρ_{xx} and quantization of Hall conductance σ_{xy} (Fig. 4.11a). The quantization is described by $\sigma_{xy} = \pm \frac{e^2}{h}\nu$, where $\nu = \pm 4(N + 1/2)$ is the filling factor (number of filled Landau levels (LL)), N is a non-negative integer, e is the elementary charge, h is the Plank constant, and ± stands for electrons and holes. Observation of half-integer quantized Hall plateaus accompanied by vanishing ρ_{xx} is a clear signature of the quantum Hall effect (QHE) in single layer graphene devices [149,157]. The quantization appears for both sweeping directions with identical QH plateau (Fig. 4.11c and d) and for clarity, only backward sweeping ρ_{xx} and σ_{xy} data are plotted together in Fig. 4.11a. Here the Hall measurements were taken at 2 K.

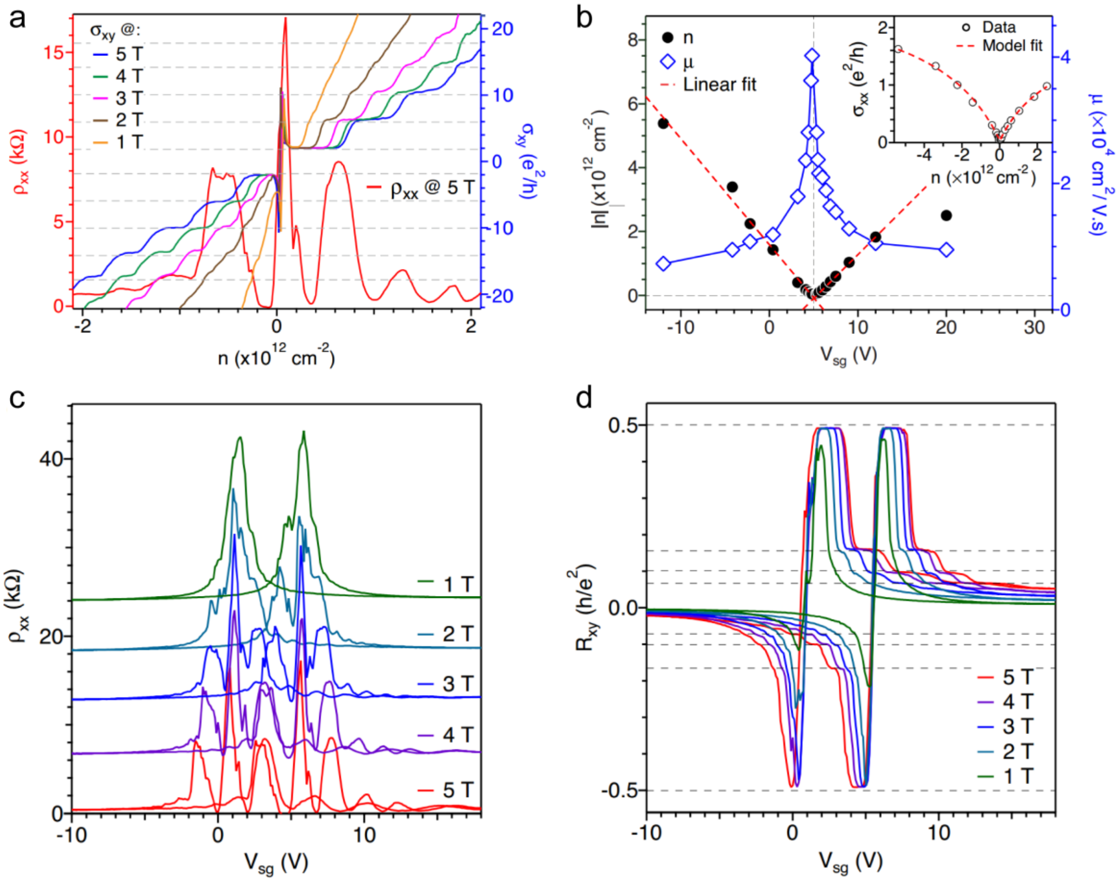

Figure 4.11 Side gate dependent transport properties. a, Longitudinal resistivity ρ_{xx} and Hall conductance σ_{xy} as a function of carrier density n with perpendicular magnetic fields, showing half-integer quantum Hall effect in graphene. **b,** Carrier density n and Hall mobility μ as a function of V_{sg}. Dashed red line represents a linear fit along positive and negative directions. Inset shows the sheet conductivity σ_{xy} as a function of carrier density n and red dashed line is a fit to the model described in the text. **c,** V_{sg} dependence of graphene resistivity. Hysteresis appears when gate sweeping is reversed. Pronounced SdH oscillations develop as the field is increased and the oscillations are equally visible at both sides of hysteresis. **d,** V_{sg} dependence of Hall resistance, simultaneous measured as the data in **c**. Hall plateaus develop at each minimum of SdH oscillations at high fields, showing QHE equally appears at both sides of hysteresis. All the measurements were taken at 2 K.

From the measured field-dependent sheet resistivity ρ_{xx} and transverse resistance R_{xy}, we can extracted carrier density n and the Hall mobility μ at different V_{sg} (Fig. 4.11b). At low magnetic fields the linear slope $s = dR_{xy}/dB$ determines the carrier density $n = 1/(s \cdot e)$. The Hall mobility μ is calculated through the expression $\mu = 1/(n \cdot e \cdot R_{xy})$. The carrier density n has a linear dependence with V_{sg} towards both electron and hole sides of the Dirac point (red dashed lines), demonstrating efficient field-effect gating behavior through the complex oxide heterostructure. The density saturates near the Dirac point to a minimum density of $n_{min} \sim 4 \times 10^{10}$ cm^{-2}, which is also apparent from the crossing point of linear fits that lies below zero at $V_{sg} = V_{Dirac} \sim 5$ V. Below n_{min} the Hall resistance becomes significantly nonlinear due to the inhomogeneous landscape of carriers in electron-hole puddles [193] and therefore determination of carrier density from the Hall coefficient becomes non-trivial. The relatively low saturation density n_{min} we observe indicates low disorder in our samples. The density dependence of Hall mobility shows sharp peak near the Dirac point and slowly approaches saturation at either sides of electron and holes around Dirac point. Such a sharp profile of mobility is a direct consequence of strong dielectric screening of charged impurity scattering, as reported previously in graphene devices supported on different high-κ materials [190,194,195]. The mobility of our device varies in the range $\sim 1 - 4{\times}10^4$ cm^2/V$\cdot$s over the entire gate voltage region, which is comparable with the best CVD-grown graphene devices reported to date [196,197]. Since the Hall mobility depends strongly on the carrier density, it is natural to examine the density-independent mobility μ_c, which is associated with long-range Coulomb scattering and excludes the effects of various other sources of disorders. Therefore, we estimate μ_c by fitting the sheet conductivity σ_{xx} data using the commonly employed self-consistent diffusive transport model [183]. The model fits the data well with $\mu_c \sim 2 \times 10^4$ cm^2 /V$\cdot$s (Fig. 4.11b, insert), further confirming the high quality of these samples.

Beside side gate V_{sg}, back gate V_{bg} can also tune the transport properties of the graphene layer. Similar results, for example, hysteresis and half-integer quantum Hall effect as a function of V_{sg} were observed (Fig 4.12).

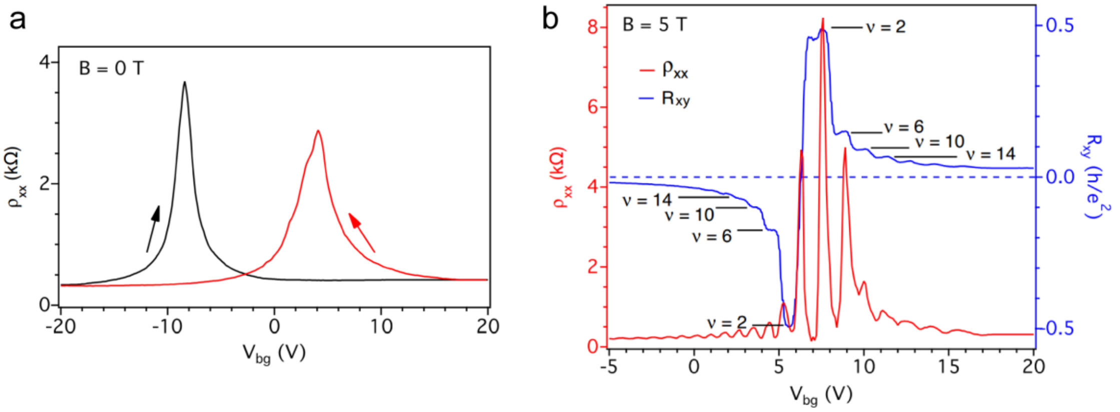

Figure 4.12 Tune graphene transport properties using back gate through LAO/STO. a, Back gate dependence of longitudinal resistivity ρ_{xx} measured at zero field B = 0 T and at 2 K. Hysteresis is observed when the gate tuning direction is reversed. **b,** Simultaneously measured back gate dependence of longitudinal resistivity ρ_{xx} and Hall resistance R_{xy} measured at fixed field of B = 5 T and at 2 K. Since all features are identical at each side of hysteresis only the right side of gate tuning is shown.

4.5.4 Temperature dependent transport

We examine the temperature dependence of transport properties by measuring ρ_{xx} and the Hall resistance R_{xy} simultaneously at zero field and a fixed field of B = 5 T, during warming up the sample (Fig. 4.13a). Surprisingly, ρ_{xx} at zero field rapidly increases from ~ 350 Ω as the sample starts getting warmed up from 2 K, peaks at ~ 3.5 kΩ near 130 K, and then slowly decreases to ~1.5 kΩ at 300 K. This behavior has been reproduced for both warm-up and cool-down cycles, with minor shift that may be attributed to slight differences in actual sample temperature during each thermal cycle. At B = 5 T, ρ_{xx} exhibits pronounced oscillations and R_{xy} shows well-defined plateaus at each oscillation minimum up to 100 K (red arrows in Fig. 4.13a). Above 100 K, the slope of the Hall resistance changes sign from negative to positive, showing change of polarity from hole-doped at low temperature to electron-doped at high temperatures. The oscillation minima and the Hall quantization matches with the LL filling factors for single-layer graphene, revealing the half-integer QHE in graphene measured as a function of temperature. These features, however, are smeared out above 100 K (towards the electron-doped side), which is caused by thermal broadening of LLs. The zero-field resistivity obtained from field sweeping measurement is plotted out in Fig. 4.13b. Note that the zero-field resistivity peak is shifted 20 K lower as compared to the resistivity measured by continuously ramping the temperature, which may be caused by actual temperature variation on the sample.

The observed resistivity behavior is consistent with temperature-dependent transport parameters such as carrier density n and Hall mobility μ (Fig. 4.13c). The carrier density, estimated by using the period of SdH oscillations, falls to the lowest value of $n \sim 1.15 \times 10^{11}$ cm^{-2} at around 110 K where the zero-field resistivity peaks to its maximum. The Hall mobility also increases from $\mu \sim 1 \times 10^{4}$ cm^{2}/V • s in the low-density regime. The two temperature dependent resistivity measurements at 0 ant 5 T confirm that changing temperature can also tune graphene Fermi level across the Dirac point, similar to the electric field tuning of the graphene Fermi-level. It is interesting to note that, taking into account the shift in n with temperature, the mobility away from the Dirac point is almost completely independent of temperature up to room temperature.

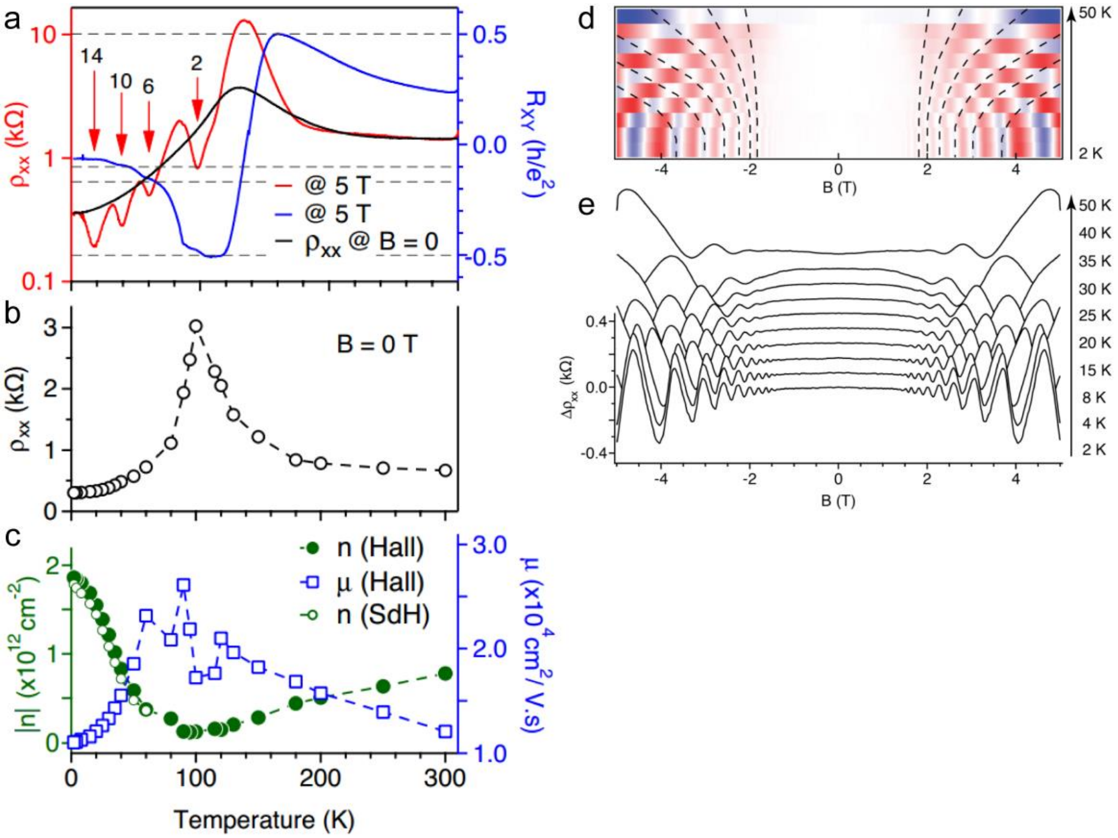

Figure 4.13 Temperature-dependent transport properties. a, The sheet resistivity ρ_{xx} and the Hall resistance R_{xy} of the graphene device at B = 5 T while ramping the temperature from 2 K to 300 K. **b,** Zero-field ρ_{xx} obtained from the magnetoresistance data. The peak is slightly shifted compared to continuously ramping the temperatures. **c,** Extracted carrier density n and Hall mobility μ at different temperatures. n was estimated from the slope of the Hall coefficient and also from the period of the SdH oscillations (up to 60 K). **d** and **e,** ρ_{xx} measured during sweeping of out-of-plane magnetic field from +5 T to −5 T at different temperatures from 2 K to 50 K. The SdH oscillation amplitude gradually decreases as the sample is warmed up, due to thermal broadening of LLs. The oscillation period also gradually increases with increasing sample temperature, as indicated by the black dashed lines in the 2D color plot. This shift suggests a gradual change of the Fermi level towards the Dirac point as the sample temperature increases.

We argue that the unusual temperature dependence of the transport behavior in our device is caused by the unique interaction between graphene and LAO/STO; residual traps cannot induce a nearly one order of magnitude change in carrier density in graphene, otherwise the sample would have been more p-doped than n-doped at room temperature. The unique interaction is attributed to the modulation doping in graphene due to induced change of carrier density at the LAO/STO interface as a function of temperature. Early studies showed that the 2DEG carrier density changes by ~ 1×10^{12} cm^{-2} when a semi-insulating 3.5 uc LAO/STO sample is cooled from 300 K to 20 K. [198]. The density increases sharply up to 2-orders of magnitude when the LAO coverage is increased only half a unit cell from 3.0 uc to 3.5 uc [48]. It should be pointed out that the maximum change of carrier density in graphene is about ~ 2×10^{12} cm^{-2}, which is almost the same order of magnitude as in the case for oxide interface. Similarly, the conductance and the mobility also change significantly at around 100 K, providing strong support of observed temperature dependent transport behavior in our samples. Besides that we also observed a shift of the Fermi level towards the Dirac point at V_{sg} = 12 V when temperature increased from the low temperature side toward 100 K (Fig. 4.13d and e). The interface carrier density is also very sensitive to any modifications on the surface and lattice structure, therefore the carrier density in graphene may change correspondingly. Signatures of those modifications are also reflected by our results, in which graphene resistance shows slight anomaly at around 100 K due to the phase transition of STO from tetragonal to the cubic phase [9]. Such anomaly of resistance behavior has been also reported in previous work on graphene/STO [189].

4.5.5 Density-dependent magnetotransport and scattering

Now we investigate the carrier scattering behavior in our graphene devices via magnetotransport measurements. Magnetoresistance (MR) is calculated by using the expression: $\Delta\rho_{\text{xx}}(B) = \rho_{\text{xx}}(B) - \rho_{\text{xx}}(B = 0)$ and magnetoconductance (MC) is calculated by $\Delta\sigma_{xx}(B) = \rho_{xx}^{-1}(B) - \rho_{xx}^{-1}(B = 0)$. Carrier density is estimated by simultaneously recorded Hall coefficients. Our series of MR data of the graphene device were measured at 2 K over a broad range of carrier densities near the Dirac point (Fig. 4.14a). The MR behavior can be divided into two regimes, i.e., high-field ($|B| > 1$ T) and low-field ($|B| < 1$ T) regimes. At high-fields, pronounced SdH oscillations and corresponding Hall plateaus at each oscillation minima are observed. A clear change of period (or frequency) is visible with changing V_{sg} (i.e., carrier density). An analysis of the minima of the SdH oscillations (Fig. 4.14d to f) for a carrier density of $n = -1.6 \times 10^{12}$ cm^{-2} yields the expected Berry phase of π for single-layer graphene [149,157]. At low-fields, the MR is almost unchanged except for some random fluctuations, which might be attributed to universal conductance fluctuations [199]. Such a flat MR behavior around zero-field is an indication of suppressed WL. As the carrier density is further reduced by tuning the Fermi level towards the Dirac point, the MR gradually increases near $B = 0$ T, showing a cusp-like dip. Observation of positive magnetoresistance is a clear signature of WAL in our samples. The positive MR increases faster as the carrier density approaches $n_{\min}$, where the mobility is the highest, showing noticeable correlation with density and the mobility.

To further explore the scattering mechanism, the results were fitted with a model of WL correction for graphene [172], where three dominant scattering processes have been considered: usual inelastic (phase breaking) scattering, elastic intervalley scattering, and intravalley scattering. According to this model, the correction to the magnetoconductance (MC) is expressed as:

$$\Delta\sigma(B) = \frac{e^2}{\pi h}[F\left(\frac{B}{B_\phi}\right) - F\left(\frac{B}{B_\phi + 2B_i}\right) - 2F\left(\frac{B}{B_\phi + B_i + B_*}\right)] \tag{4-1}$$

Where $\mathrm{F}(\mathrm{Z}) = \ln(Z) + \Psi\left(\frac{1}{2} + \frac{1}{Z}\right)$, where Ψ is the digamma function and $B_{\phi,i,*} = \frac{\hbar}{4eD} L_{\phi,i,*}^{-2}$ demotes characteristic magnetic fields associated with the diffusion constant D. Here, L_ϕ is the phase coherence length, L_i is the elastic inter-valley scattering length, and L_* is related to the intra-valley scattering length L_{iv} and trigonal warping length L_w via $L_*^{-2} = L_{iv}^{-2} + L_w^{-2}$. From these scattering lengths we can extract corresponding scattering rates using $L_{\phi,i,*} = \sqrt{D\tau_{\phi,i,*}}$. The first term in equation (1) corresponds to the usual WL observed in typical 2D systems where the electron mean free path is shorter than the phase coherence length, while the second and third terms lead to WAL. The shape of the MC curves varies because it results from the interplay between all scattering processes involved.

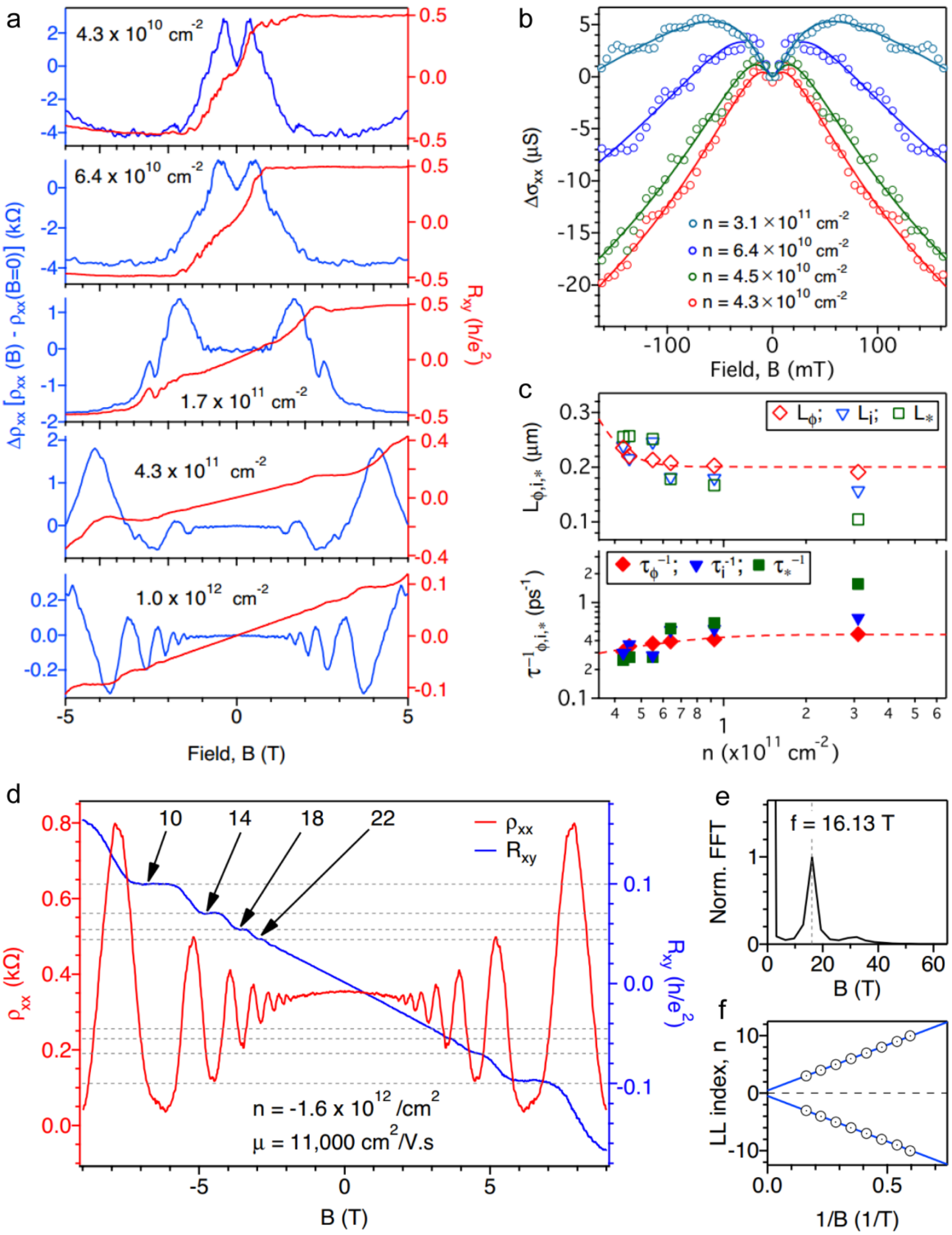
a
4.3 x 10^10 cm^-2
6.4 x 10^10 cm^-2
1.7 x 10^11 cm^-2
4.3 x 10^11 cm^-2
1.0 x 10^12 cm^-2
Δρxx [ρxx (B) - ρxx(B=0)] (kΩ)
Rxy (h/e^2)
Field, B (T)
b
n = 3.1 × 10^11 cm^-2
n = 6.4 × 10^10 cm^-2
n = 4.5 × 10^10 cm^-2
n = 4.3 × 10^10 cm^-2
Δσxx (μS)
Field, B (mT)
c
Lφ; Li; L*
Lφ,i,* (μm)
τφ^-1; τi^-1; τ*^-1
τ^-1φ,i,* (ps^-1)
n (x10^11 cm^-2)
d
10
14
18
22
ρxx
Rxy
n = -1.6 x 10^12 /cm^2
μ = 11,000 cm^2/V.s
ρxx (kΩ)
Rxy (h/e^2)
B (T)
e
f = 16.13 T
Norm. FFT
B (T)
f
LL index, n
1/B (1/T)

Figure 4.14 Carrier density dependent magnetotransport. a, Magnetoresistance (MR) and R_{xy} data at different carrier densities *n*. At high-fields ($|B| > 1$ T), the MR shows well-defined SdH oscillations and corresponding Hall plateaus at each oscillation minimum, characteristic of half-integer quantum Hall effect. At low-fields ($|B| < 1$ T), the MR is almost flat at high carrier densities and it becomes positive at low densities as the Fermi level is tuned close to the Dirac point, showing a clear transition from suppressed WL to WAL. **b,** Modeling of low-field magnetoconductance (MC) data in the vicinity of the Dirac point, showing a clear transition to WAL below $n \sim 6\times10^{10}$ cm^{-2}. **c,** Extracted scattering lengths $\boldsymbol{L_{\phi,i,*}}$ and corresponding scattering rates $\boldsymbol{\tau_{\phi,i,*}^{-1}}$ obtained from the fitting, which show a rapid change as the carrier density *n* falls below 6×10^{10} cm^{-2}. Red dashed lines correspond to the exponential fits as guide to eyes. **d,** ρ_{xx} and R_{xy} as a function of out-of-plane magnetic field up to ±9 T at $V_{sg} = 0$, measured at 0.1 K . **e,** Frequency of the SdH oscillations $f = 16.13$ T is extracted for the fast Fourier transform of the ρ_{xx} versus 1/B plot. **f,** Plot of Landau level (LL) index as a function of 1/B. The solid lines correspond to a linear fit with a slope of 16.13 T, in which the intercept of 0.45 estimates a Berry's phase of π in graphene.

Equation (4-1) fits well with the low-field MR data I the vicinity of the Dirac point using the free parameters B_ϕ, B_i and B_* (Fig. 3.14b). To extract the scattering lengths $L_{\phi,i,*}$, we estimated the diffusion constant by using the relation $D = \frac{v_F l}{2} = \frac{v_F}{2}\ (h/2e^2\ k_F R_{xx})$, where v_F is the Fermi velocity, k_F is the Fermi wave vector, and *l* is the carrier mean free path. The Fermi wave vector k_F in graphene is related to the carrier density *n* by $k_F = \sqrt{\pi n}$. We determine k_F from the carrier densities measured by Hall measurements at 6 positions in the vicinity of the Dirac point. We calculate diffusion constants using the typical Fermi velocity in graphene, $v_F = 1\times10^8$ cm/s, which also allow us to convert scattering rates using the expression described earlier. The inelastic scattering length L_ϕ exceeds 200 nm and monotonically increases as the carrier density is further reduced (Fig. 4.14c). The corresponding scattering rates exhibit similar trends, i.e., the rate decreases as the carrier density decreases. The inelastic scattering rate τ_ϕ^{-1} becomes as small as 0.3 ps^{-1} at the lowest density region. Although the elastic scattering lengths $L_{i,*}$ (or rates $\tau_{i,*}^{-1}$) are comparable to L_ϕ (or τ_ϕ^{-1}), there is a noticeable gradual transition at a carrier density of $n_t \sim 6\times$

10^{12} cm^{-2}, below which $L_{i,*}$ exceeds L_{ϕ} (or τ_{ϕ}^{-1} exceeds $\tau_{i,*}^{-1}$). The observation of a sharp change of both scattering lengths and rates near the Dirac point (Fig. 4.14b) agrees well with the density dependence of mobility of our samples (Fig 4.13b). Due to strong screening of charged impurity scattering close to the Dirac point, chirality breaking intervalley scattering process is suppressed and dominated by intravalley scattering, therefore WAL shows up. This observation qualitatively agrees also with theoretically predicted favorable WAL regime in graphene because ratio of scattering times τ_{ϕ}/τ_{*} and τ_{ϕ}/τ_{i} are smaller than 1 when $n < n_c$. In contrast to previous observations [174,200], in which the dephasing length decreases as the carrier density decreases, our results suggest significant screening of intervalley scattering processes, further highlighting the essential role of the LAO/STO substrate.

4.5.6 Temperature-dependent magnetotransport and scattering

We now investigate the temperature dependence of the magnetotransport properties and scattering parameters. MC is measured while sweeping the magnetic field from -5 T to 5 T at different temperatures (Fig. 4.15a). For better visibility, each curve except the 40 K curve is vertically shifted. Data below 40 K shows almost flat MC around zero field and pronounced SdH oscillations at higher fields (Fig. 4.13e). At 50 K, a broad peak near $B = 0$ T and subsequent negative MC show up. The width and the relative change of the peak increases with temperature and reaches a maximum at ~ 100 − 120 K where the carrier density reaches the lowest value and the mobility is highest. Above 120 K, the dip decreases and widens again as the carrier density increases and the mobility slowly decreases. Interestingly, it turns out that the negative MC persists up to 300 K, providing strong evidence that the chiral nature of the carriers survives even at room temperature.

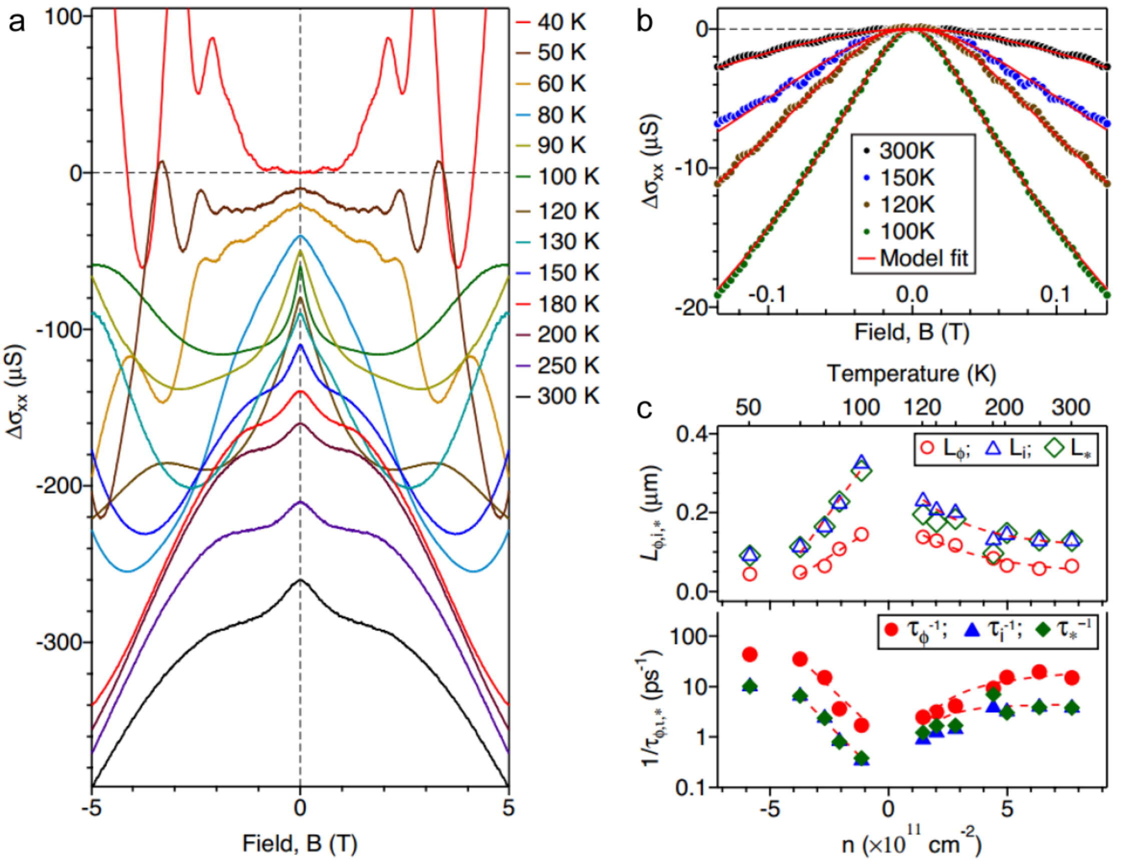

Figure 4.15 Temperature dependent magnetotransport. a, Magnetoconductance (MC) data measured at different temperatures. Each curve (except 40 K data) is shifted equidistance (−10 μS/10 K) vertically for clarity. **b,** Weak antilocalization model fittings of the low-field MC data shown in **a**. **c,** Extracted scattering lengths $\boldsymbol{L_{\phi,i,*}}$ and rates $\boldsymbol{\tau^{-1}_{\phi,i,*}}$ as a function of temperature and carrier density. Red dashed lines are guides to eye.

To examine the WAL further, low-field MC data is fitted using Equation (1) and scattering lengths and rates are extracted (Fig. 4.15b). The model fits quite well for all temperatures and we also plot these extracted scattering parameters as a function of temperatures as well as carrier densities (Fig. 4.15c). The overall trend shows that both elastic and inelastic scattering lengths increases up to 100 K where carrier density is minimum, and slowly smooths out as the temperature approaches 300 K. Similarly, the scattering rates decrease in the low-density regime near the Dirac point and slowly increases up to 300 K. The maximum dephasing length L_ϕ = 190 nm and maximum inelastic length $L_{i,*}$ = 350 nm are achieved near 100 K. L_ϕ decreases to 75 nm and $L_{i,*}$

decreases to 120 nm as temperature increase to 300 K. Due to the large scattering lengths (small scattering rates) at room temperature, the ratios of $\tau_\phi/\tau_*$and τ_ϕ/τ_i turn out to be much smaller (< 0.5) than the values at 2 K, which is consistent with the observation of strong WAL at high temperature and the predicted WAL regime in graphene [172]. In addition, the overall temperature dependence of the WAL data resembles the density-dependence data (Fig. 4.14c) and supports our explanation of greatly suppressed short-range scattering due to enhanced dielectric screening in our sample.

4.6 CONCLUSION AND DISCUSSIONS

In summary, it has been demonstrated that the metal-insulator transition of LAO/STO heterostructures can be controlled by c-AFM lithography in the presence of exfoliated or CVD-grown SLG. These hybrid materials are expected to produce a variety of novel phenomena owing to the rich behavior of each constituent system and the nanoscale control over the complex-oxide properties. Novel correlations, tunable THz plasmonic properties, and superconducting proximity effects are just a few of the possible new directions which are enabled by graphene/LAO/STO heterostructures.

We have achieved high mobility graphene field-effect devices by integrating CVD-grown graphene with LAO/STO. These devices show anomalous quantum Hall effect and suppressed backscattering of quantum interference signature, as expected from high quality graphene samples. Unique features of this system are (1) the sharp rise of carrier mobility close to the Dirac point attributed to screening by the LAO/STO interface and (2) temperature independent high mobility up to 300 K due to weak coupling with substrate optical modes. Therefore, assisted by unique interaction with oxide substrate, we observed first direct observation of suppressed-backscattering as WAL quantum interference signature in CVD-grown graphene at both low temperatures (~2 K) and high temperatures (~ 300 K).

WAL is predicted in pristine and defect-free single layer graphene [201,202] and is attributed to the signature of pseudospin symmetry of electronic states caused by sub-lattice degeneracy in the graphene band structure. In multilayer graphene or graphite, such a degeneracy is lifted and therefore WAL is not expected nor observed. Despite the theoretical prediction, WAL has been reported only in exfoliated and epitaxial graphene samples [176,177]. WL has been routinely observed in graphene samples [174,203], and is attributed to presence of disorder. In contrast to previous studies of CVD-grown graphene on SiO_2, our results demonstrate the first direct evidence of WAL observed in CVD-grown graphene samples and point to the critical role of the ultraflat surface and conducting interface of the LAO/STO substrate in suppressing short-range inter-valley scattering. In addition, we have observed a crossover from WL to WAL regimes near the Dirac point at 2 K as the carrier density is reduced and mobility is increased, a consequence of enhanced dielectric screening of short-range charge impurities close to the Dirac point thereby increasing the intra-valley scattering contributions. WAL is completely suppressed in the high-density regime (Fig. 4.14a), where graphene's own screening ability is activated due to abundant carriers and consequently intervalley scattering dominates. Therefore, the interplay of short range and long range scattering contributions and the role of substrate dielectric screening qualitatively supports our observation of a systematic transition from WL to WAL as the Fermi level is tuned towards the Dirac point.

A similar situation was also observed in the temperature-dependent magnetotransport measurements. Our devices show ambipolar tuning of carrier density and mobility with temperature (Fig 4.13), which is correlated with the field-effect gating behavior. Extracted scattering lengths (rates) increase (decrease) around the Dirac point at ~110 K and decrease towards low temperatures and high temperatures, showing a correlation with carrier density and the mobility. The inelastic scattering length varies between 150 nm at 2 K and ~300 nm at 110 K, whereas elastic scattering lengths range between 150 nm and 300 nm at respective temperatures. Observation of almost identical scattering parameters at 2 K and room temperature is quite surprising, suggesting weak coupling with surface phonons. Similar work performed on exfoliated graphene samples on SiO_2 shows WAL effect up to 200 K and beyond that it disappears due to rapid dephasing of interference between time-reversed electron trajectories [177]. The strong dielectric screening of charged impurity scattering, minimal surface corrugation, and suppression of phonon scattering have all played a crucial role for the long dephasing length over a broad temperature range in our samples, which allows the preservation of charge carrier chirality up to room temperature

The persistence of WAL to RT is an important step forward to the realization of pseudospin based graphene devices, and presents an opportunity to explore novel physics that might result from proximal coupling with oxide interface multifunctional devices that combine graphene with a complex-oxide heterointerface.

5.0 ANISOTROPIC QUASI-ONE-DIMENSIONAL SUPERCONDUCTIVITY AT (110) LAO/STO INTERFACE

The interplay of electronic, magnetic, and superconducting phenomena at the (001)-oriented LAO/STO interface is highly sensitive to the occupancy of Ti *d*-orbital bands. Recent reports of two-dimensional conductivity and superconductivity at the (110) LAO/STO interface have introduced new anisotropic character to electronic transport at oxide interfaces. Here we investigate transport of conducting nanowires at the (110) LAO/STO interface along distinct in-plane crystallographic directions. Nanowires undergo superconducting transitions that are gate-tunable, with an upper critical field exhibiting non-monotonic "dome-like" dependence similar to what is observed for bulk STO and (001) LAO/STO heterostructures. Significantly, the dome is shifted to higher gate voltages along the [001] direction compared with the $[1\bar{1}0]$ direction. The results demonstrate how superconductivity is profoundly affected by lateral quantum confinement and crystallographic orientation.

5.1 BACKGROUND AND MOTIVATION

Intensive investigations of the 2DEL at the interface of LAO and TiO_2-terminated STO have revealed a rich palette of physical phenomena. Initial experiments used heterostructures grown on (001)-oriented STO substrates. Recently a conducting interface between LAO and (110)-oriented STO has been reported [31,32] with a hierarchy of band structures [38] and superconductivity with anisotropic character [39]. Crystallographic orientation is now firmly established as an additional discrete tuning parameter that influences the rich physical properties at the LAO/STO interface.

We are interested in exploring how the crystal orientation influence the quasi-1D superconducting properties of the nanowires. Our results can provide insight into fundamental mechanisms for electron pairing, to create quantum-confined nanostructures with strongly attractive pairing interactions [59], and serve as a design choice in a solid-state quantum simulation platform.

5.2 EXPERIMENT APPROACHES

A thin LAO layer (3 uc) is deposited on atomically smooth (110)-oriented STO substrates using pulsed laser deposition under oxygen pressure $P_{O_2} = 1 \times 10^{-3}$ Torr and temperature 720 ℃. Electrical contact to the interface is established by etching down 25 nm from the surface of LAO into the STO and depositing 5 nm Ti and 25 nm Au to fill the trench. The electrode pattern allows a 30 μm × 30 μm region to be accessed for the creation of nanostructures. Electrical measurements confirm that these heterostructures have initially insulating interfaces. A six-terminal device composed of nanowire segments (Fig. 5.1a) is created to study anisotropic quasi-1D transport at the LAO/(110)STO interface. For accurate comparison between the [001] and $[1\bar{1}0]$ directions, transport properties are measured simultaneously across the two nanowire segments of same channel length $L = 6.5\ \mu\mathrm{m}$. The nanowires have a very close width, which is determined by writing parameters such as tip voltage, writing speed, and relative humidity in the AFM chamber. A typical nanowire width $w \sim 10$ nm is used for the (110) LAO/STO interface, which comparable to nanowires written at (001) LAO/STO interfaces as determined by erasure experiments [120].

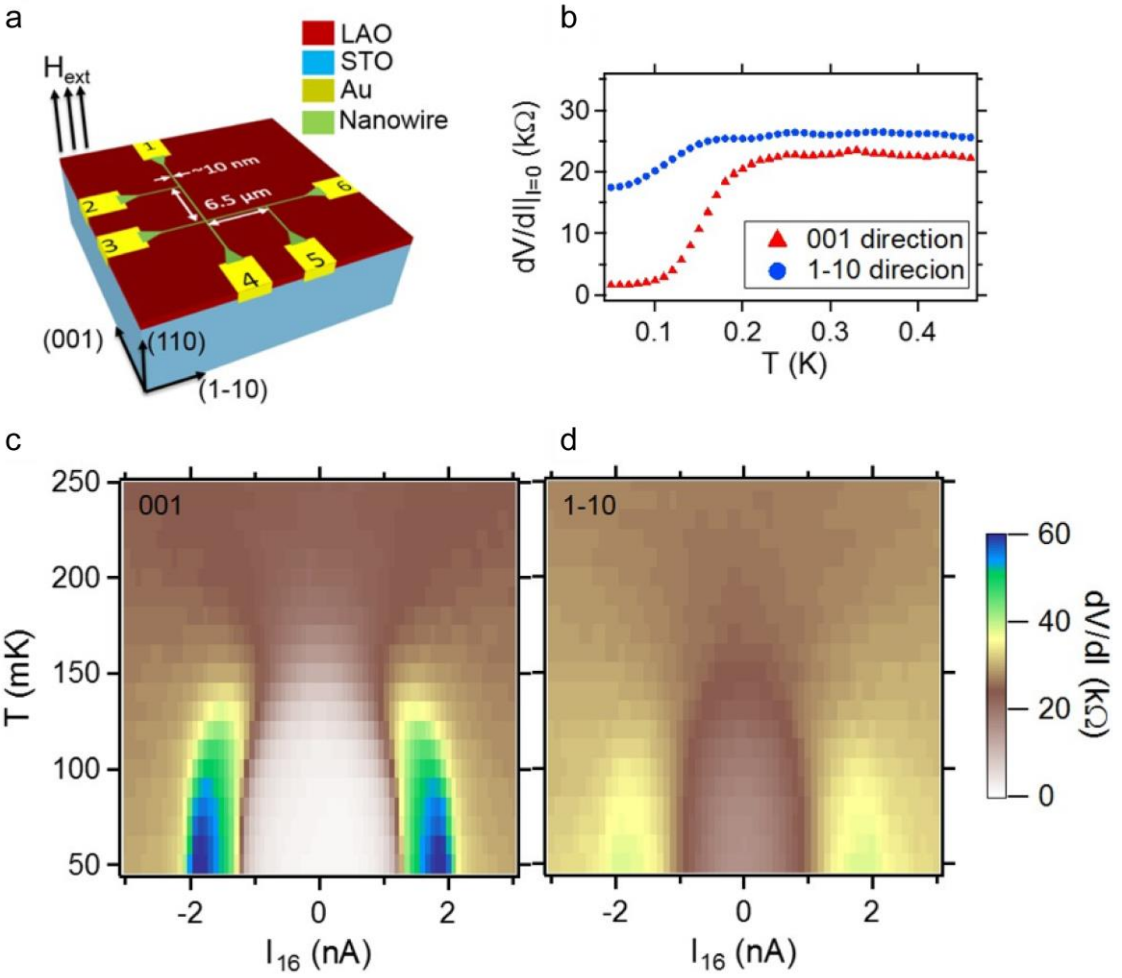

Figure 5.1 Device schematic and temperature dependence of normal to superconducting transition. a, Device schematic. A six-terminal nanostructure is created at (110) LAO/STO interface using c-AFM lithography technique. Nanowire width is around 10 nm, and the two sections for 4-terminal voltage measurement have the same length 6.5 um. **b,** Differential resistance around zero bias versus temperature at zero magnetic field. **c** and **d,** Intensity graph of the differential resistance for [001] direction and $[1\bar{1}0]$ direction, respectively. Temperature is swept between 50 mK and 500 mK.

After writing, the device is cooled to millikelvin temperatures (base temperature ~ 50 mK) using a dilution refrigerator. A current applied between terminals 1 and 6 (I_{16}) passes through both the [001] and $[1\bar{1}0]$ segments. The voltage drop across each nanowire segment is measured between terminals 2 and 3 or 4 and 5 (labeled V_{23} and V_{45} respectively). DC I-V curves are measured along both directions and the four-terminal differential resistance is calculated numerically ($R_{[001]} \equiv dV_{23}/dI_{16}$ and $R_{[1\bar{1}0]} \equiv dV_{45}/dI_{16}$).

5.3 EXPERIMENT RESULTS

We first plot an intensity graph of the four-terminal differential resistance versus current and temperature while slowly changing the temperature from 50 mK to 450 mK at zero applied magnetic field represented (Fig. 5.1c and d). Along both crystallographic directions, a resistance drop associated with superconductivity is observed, with a critical current ~1 nA. The temperature dependence of the zero-bias differential resistance shows that along both directions, the superconducting transition takes place below 200 mK, albeit with the residual resistance in superconducting state being significantly higher along the $[1\bar{1}0]$ direction (Fig. 5.1b). The transition for these nanowires is broad along both directions, and qualitatively similar to the behavior of superconducting nanowires at the (001) LAO/STO interface [120].

Measurements performed in an out-of-plane magnetic field show a marked anisotropy in the superconducting upper critical field H_{c2}. At each magnetic field, the temperature is swept in the range T = 50-450 mK. We plot the extracted differential resistance near zero bias along each direction as a function of temperature (Fig. 5.2a and b). The directional anisotropy in H_{c2} is explored in more detail by measuring the differential resistance versus current and magnetic field well below the superconducting transition temperature ($T = 70$ mK). The R_{001} and $R_{1\bar{1}0}$ versus source current and external magnetic field show a clear transition between normal and superconducting states (Fig. 5.2c and d), with a significantly higher upper critical field (H_{c2}) along the [001] direction compared with the [1$\bar{1}$0] direction which is also evident from waterfall plots (Fig. 5.2e and 5.2f).

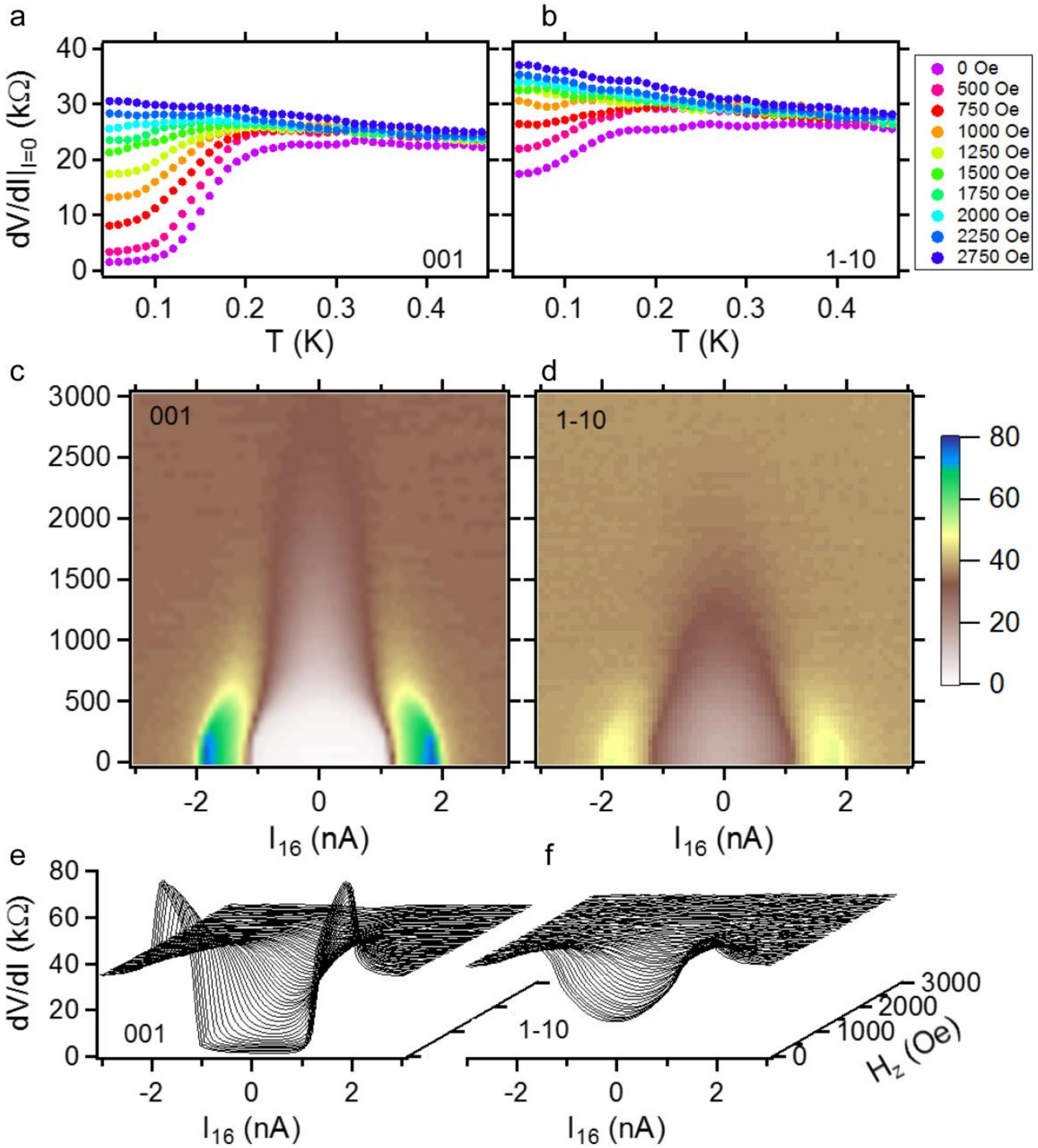

Figure 5.2 Magnetic field dependence of normal to superconducting transition. a and **b,** Differential resistance around zero bias versus temperature at out-of-plane magnetic field from 0 Oe to 3000 Oe, for [001] and [1$\bar{1}$0] direction respectively. **c** and **d,** Intensity graph of the differential resistance for direction [001] and [1$\bar{1}$0] as a function of bias current and out-of-plane magnetic field. **e** and **f,** waterfall plot of differential resistance versus current and out-of-plane magnetic field for direction [001] and [1$\bar{1}$0].

Back-gate tuning is performed to further explore the H_{c2} of nanowires along different crystallographic orientations. In order to achieve reproducible results, the back gate voltage (V_{bg}) is cycled between the extremal gate voltage range (-1.4 V to 0 V) more than 20 times before performing the actual experiments. Acquired at T = 50 mK, The intensity graphs of the differential resistance R_{001} and $R_{1\text{-}10}$ versus current and magnetic field are plotted for selected values of V_{bg} (Fig. 5.3a and b). Along both the directions, the extracted H_{c2} exhibits a "dome-like" shape as a function of V_{bg} (Fig. 5.3c). The vanishing of superconductivity for either side of V_{bg} can be related to the back-gate tuned electron density change (over-doped and under-doped regime), similar to other reports for (001) LAO/STO [3]. A pronounced upward shift ΔV_{bg} ~ 200 mV for the [001] direction nanowire is observed, compared with the $[1\bar{1}0]$-oriented nanowire.

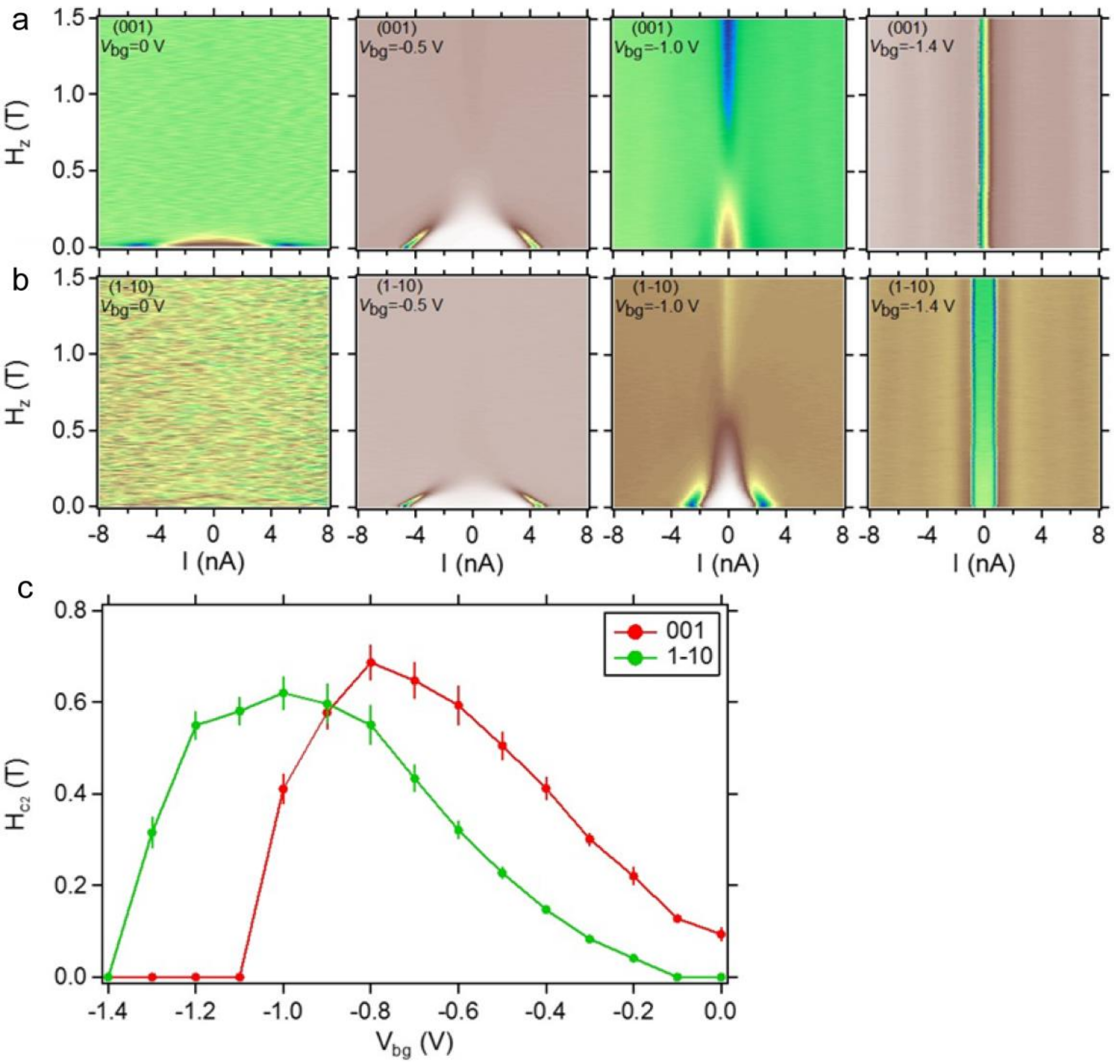

Figure 5.3 Back gate voltage V_{bg} tuning of superconductivity. a and **b,** Intensity graph of the differential resistance of nanowires along [001] and [1$\bar{1}$0] as a function of bias current and out-of-plane magnetic field at selected back gate voltage V_{bg}. **c** extracted upper critical field H_{c2} versus V_{bg} of nanowires along (001) and [1$\bar{1}$0] direction.

To get more insight in to the directional dependence on Hc_2, we have performed a control experiment with a modified device geometry with four nanowires of similar dimensions created along (001), (1-10), (1-1-1) and (1-11) directions. In addition to the [001] and [1$\bar{1}$0] directions, nanowires of similar dimensions are created along [1$\bar{1}\bar{1}$] and [1$\bar{1}$1] directions that are related by reflection about the [1$\bar{1}$0] direction with 45 ° angle. The gating and transport experiments are simultaneously performed for all the four nanowire directions, which helps to rule out systematic variations in measurement conditions (e.g., temperature, magnetic field, gate voltage). A characteristic "dome-like" behavior is reproducible and evident for all the directions. Significantly, the shift in "dome-like" structure is clearly evident for [001] and $[1\bar{1}0]$ directions (Fig. 5.4a), and such structure is fairly overlapped for $[1\bar{1}\bar{1}]$ and $[1\bar{1}1]$ directions (Fig. 5.4b) as expected under general symmetry considerations. The results infer that the crystallographic orientation indeed plays a predominant role in superconductivity.

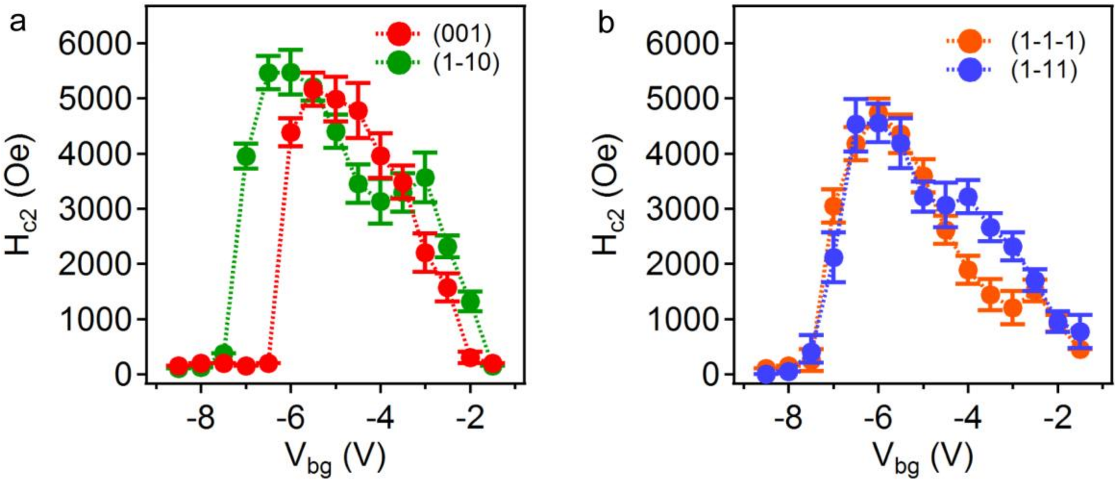

Figure 5.4 Directional dependence of upper critical magnetic field. a, Schematic of device geometry for nanowires written along various crystallographic directions. **b,** Extracted upper critical field H_{c2} versus V_{bg} of nanowires along (001) and (1-10) directions, showing a shift in dome-like shape. **c,** Extracted upper critical field H_{c2} versus V_{bg} of nanowires along isotropic (1-1-1) and (1-11) directions, showing fairly overlapped dome shape.

5.4 POSSIBLE EXPLANNATIONS

In the case of (001) LAO/STO, the gate tuning of superconductivity is shown to be sensitive to the orbital occupancy associated with a Lifshitz transition between the lower d_{xy} and higher d_{xz}/d_{yz} bands [204]. The hierarchy of orbital occupancy can also be crucial in the quasi-1D nanowires, since lateral confinement is expected to alter the energy level spectrum further. Here we are arguing that crystallographic orientations can significantly affect the band structures and orbital occupancy in the quasi-1D nanowires thus result in the anisotropic superconducting behavior.

Starting from the 2DEL at LAO/STO interfaces, it is already established that vertical confinement at the (001) and (110) LAO/STO interfaces produces a ~50 meV energy splitting between the different *d*-orbitals which is inversely proportional to their effective masses along the confinement directions [39,41]. Considering the confinement along the vertical as well as in-plane directions, we present a schematic view of the orbital hierarchy for the (001) and (110) cases (Fig. 5.5a). For interfacial confinement in (001) orientation, d_{xy} orbitals overlap with a π-type bonding that results in a larger effective mass than the d_{xz}/d_{yz} (Fig. 4a), i.e. $m_{xy,(001)} > m_{xz/yz,(001)}$, resulting in an energy landscape as depicted in Fig. 5.5d. Whereas for interfacial confinement in (110) orientation, σ-like bonding between d_{xy} orbitals when projected in a straight line leads to a smaller effective mass than the d_{xz}/d_{yz} (Fig. 4b), i.e. $m_{xz/yz,(110)} > m_{xy,(110)}$. The d_{xz}/d_{yz} orbitals can also bond along (1-10) direction in a "zig-zag" way, as described in Ref. [40], which still gives $m_{xz/yz,(110)} > m_{xy,(110)}$. Thus the (110) LAO/STO interface is expected to possess an inverted orbital hierarchy compared to (001) one with relatively larger energy spacing between dxy and d_{xz}/d_{yz} orbitals [38].

In addition to the vertical confinement discussed above, quasi-1D nanowires created along [001] and $[1\bar{1}0]$ in-plane directions at the (110) LAO/STO interface offer additional lateral confinement that is expected to alter the energy shifts based on crystal symmetry. Lateral confinement along the [001] direction, as shown in Fig 4c, reduces orbital overlap and therefore increases the effective mass of d_{xy} states compared with the d_{xz}/d_{yz} states: i.e., $m_{xy,[001]} > m_{xz/yz,[001]}$. The d_{xy} band of electrons in nanowires along the $[1\bar{1}0]$ direction will be driven toward the d_{xz}/d_{yz} bands, resulting in a reduced energy splitting between the d_{xy} and d_{xz}/d_{yz} bands. For the lateral confinement along the $[1\bar{1}0]$ direction, bonding between d_{xy} orbitals is σ-like, leading to much smaller mass than the d_{xz}/d_{yz} orbitals, and the condition $m_{xy,\,[1\bar{1}0]} < m_{xz/yz,\,[1\bar{1}0]}$. As a result, for nanowires along the [001] direction, an increased energy splitting forms between d_{xy} and d_{xz}/d_{yz} bands (Fig. 5.5f). Note that due to the shape and orientation of d_{xz}/d_{yz} orbitals at the (110) LAO/STO interface, lateral confinement along [001] and $[1\bar{1}0]$ direction does not lift the degeneracy between d_{xz} and d_{yz}.

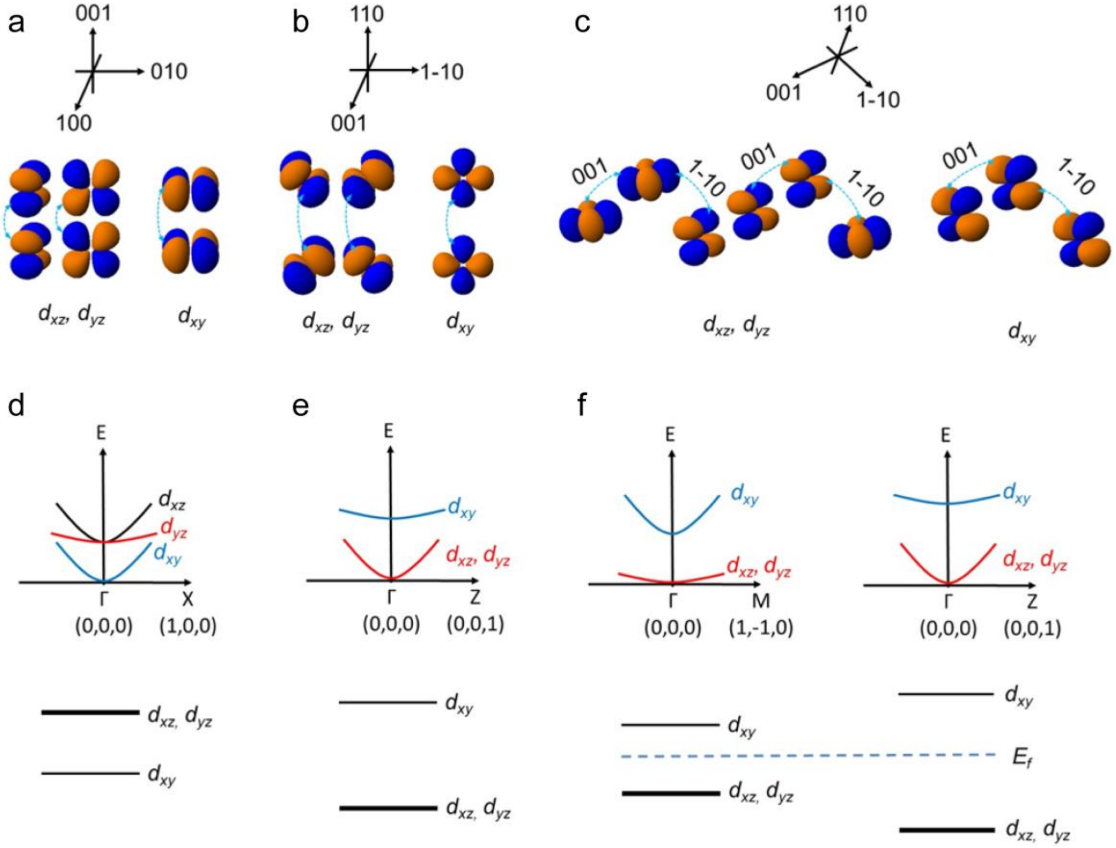

Figure 5.5 Schematic of band structures of nanowires at (110) LAO/STO. a and **b,** Schematic of Ti d-orbitals (d_{xy}, d_{xz}, d_{yz}) at (001) LAO/STO and (110) LAO/STO interface (2D). **c,** Schematic of Ti d-orbitals (d_{xy}, d_{xz}, d_{yz}) of nanowires along [001] and $[1\bar{1}0]$ directions at (110) LAO/STO. **d** and **e,** Band structures of Ti d-orbitals (d_{xy}, d_{xz}, d_{yz}) at (001) LAO/STO and (110) LAO/STO. **f,** Band structures Ti d-orbitals (d_{xy}, d_{xz}, d_{yz}) of nanowires along [001] and $[1\bar{1}0]$ directions at (110) LAO/STO.

The key result from the above analysis is that the energy splitting between d_{xy} and d_{xz}/d_{yz} bands is anisotropic, and smaller for nanowires along $[1\bar{1}0]$ direction compared with the [001] direction (Fig. 5.5f). Interfacial confinement at (110) LAO/STO leads to an energy splitting between d_{xy} and d_{xz}/d_{yz} bands, with the d_{xz}/d_{yz} bands being lower in energy [38,39]. Further lateral confinement along [001] direction suppresses the energy splitting. While lateral confinement along $[1\bar{1}0]$ direction, corresponding to nanowire along [001] direction, increases the energy splitting. Thus, we attribute the dome-like shift in H_{c2} to the relative alteration in energy splitting of bands. Moreover, the maximum H_{c2} and the maximum superconducting transition temperature is suggested to happen near the Lifshitz transition in (001) LAO/STO interfaces [204]. Such Lifshitz transition can also be expected in the case of (110) interfaces, however with a different orbital hierarchy d_{xz}/d_{yz} being lower orbitals.

5.5 CONCLUSION AND DISCUSSIONS

In summary, the 1D superconductivity of (110) LAO/STO interface is investigated by transport measurements performed on nanowires along different crystalline orientations. The intrinsically anisotropic band structure is shown to influence strongly the quasi-1D superconducting properties of the nanowires. The anisotropic band structure is also expected to influence other properties which have been reported and intensively studied in (001) LAO/STO but are relatively unexplored for (110) LAO/STO, e.g., spin-orbit interactions and magnetic properties. The sizeable in-plane anisotropy reported here could be used to provide insight into fundamental mechanisms for electron pairing, to create quantum-confined nanostructures with strongly attractive pairing interactions [59], and serve as a design choice in a solid-state quantum simulation platform.

6.0 GIANT CONDUCTIVE SWITHING OF LAO/STO HETEROINTERFACES GOVERNED BY SURFACE PROTONATION

Complex-oxide interfaces, e.g. LAO/STO, host a diversity of phenomena not present in traditional semiconductor heterostructures. Despite intense interest, many basic questions remain about the mechanisms that give rise to interfacial conductivity and the role of surface chemistry in dictating these properties. Here we demonstrate a fully reversible >4 order of magnitude conductance change at LAO/STO interfaces, regulated by LAO surface protonation. Nominally conductive interfaces are rendered insulating by solvent immersion which deprotonates the hydroxylated LAO surface; interface conductivity is restored by exposure to light, which induces reprotonation via photocatalytic oxidation of adsorbed water. The proposed mechanisms are supported by a coordinated series of electrical measurements, optical/solvent exposures, and X-ray photoelectron spectroscopy (XPS). This intimate connection between LAO surface chemistry and LAO/STO interface physics bears far-reaching implications for reconfigurable oxide nanoelectronics and raises the possibility of novel applications in which electronic properties of these materials can be locally tuned using synthetic chemistry. This work is collaborated with Dr. Keith Brown in Dr. Chad Mirkin’s group at Northwestern University.

6.1 EFFECTS OF SURFACE STATE OF LAO/STO INTERFACE

The continued miniaturization of electronics and emergence of novel 2D materials and heterostructures demands that the relationships between electronic properties and surface chemistry be well understood. With traditional (e.g. III-V) semiconductor heterostructures, the conducting interface is generally far (> 100 nm) from the functionally active surfaces, and consequently surface chemistry plays a minor role. However, for the more recent class of complex oxide heterostructures, that is, the interface between band insulators STO and LAO, a high-mobility 2DEL [30] can form less than 2 nm or 4 uc from the surface, bringing questions about the role of surface states into sharp focus. Understanding the surface chemistry of these complex-oxide interfaces is key to understanding the array of fascinating properties these materials exhibit, as described in Section 1.3.

More than a decade after the first reports of conductivity at the LAO/STO interface, the physical mechanism for 2DEL formation has not been fully and convincingly explained [83,84]. As described in Section 1.5, 2DEL formation is commonly attributed to an electronic reconstruction resulting from band bending in the polar (100) LAO layer. However the “polar catastrophe” framework does not explain 2DEL formation in (110) LAO/STO samples which have no polar discontinuity [31,32]. Furthermore, nominally insulating 3 uc (1.2 nm thick) LAO/STO samples can be rendered locally and persistently conductive via writing with charged scanning probes [49]. Switchable 2DELs in 3 uc samples implies the presence of a hidden degree of freedom, and initial investigations implicated LAO surface chemistry through the observation that humidity is required to write conductive regions with a scanning probe [114]. However, the relative importance of surface chemistry and LAO polarity is not well understood and while immersion in solvents has been observed to alter 2DEL mobility [94], post-synthetic wet chemical conditions that destroy 2DELs in samples with 4 uc or more LAO have not been previously identified. Despite this gap in experimental understanding, theoretical studies have stressed the importance of surface chemistry by linking 2DEL formation to chemical phenomena including the protonation of oxygen in LAO, the generation of oxygen vacancies, and adsorption of water [101,102,113].

6.2 SAMPLE GROWTH AND DEVICE FABRICATION

Nominally conductive 4 uc LAO films were grown on (100) single crystal STO substrates using pulsed laser deposition [79]. The growth temperature of substrates was 550 ℃ and the background oxygen pressure was 10^{-3} mbar. Details about the sample growth is described in Section 1.4. These samples were subsequently processed using standard photolithography and sputtering deposition or e-beam evaporation to define four electrodes at the corners for Van der Pauw measurements of interfacial sheet resistance R (Fig 6.1a). Unless noted otherwise, all measurements were taken in the dark under ambient atmospheric conditions.

All solvent immersion experiments were carried out in the dark or under light with the blue and UV components removed (*i.e.* cleanroom lighting). Scintillation vials were filled with ~10 mL of the solvent of interest. The sample was then placed at the bottom of the vial. Following a predetermined amount of time, the sample was removed and blown dry under flowing N_2. DI water was obtained from a filter system (Barnstead Pacific RO – Thermo Fisher Scientific Inc.).

Illumination experiments were carried out while the sample was mounted in the probe station. For broadband illumination, a mercury arc lamp (X-Cite 120Q – Excelitas Technologies Corp.) was used. At the distance at which the sample was positioned, the optical intensity in the range 400 to 500 nm was found to be 1-2 mW/cm^2. For monochromatic light, a monochromator (77250 series monochromator – Newport Corporation) was used to filter the light from a Xe arc lamp (66902 Series Arc Lamp – Newport Corporation).

6.3 CONDUCTIVITY SWITHING IN LAO/STO

6.3.1 Conductivity switching by solvent immersion/illumination

To explore the effect of solvent immersion, sheet resistance *R* was measured before and after immersing the sample in deionized water for 20 seconds and then drying under an N_2 stream. This immersion-drying-measurement cycle was iterated to generate a plot of *R* versus cumulative immersion time (Fig. 6.1b left). Surprisingly, *R* increased by > 4 orders of magnitude over the 3 total minutes of immersion. Although this insulating state was stable in the dark under ambient conditions (Fig. 6.1c), measurements of *R* following sequential 15 second exposures to broadband light revealed a decrease in R commensurate with the solvent-driven increase (Fig.6.1b right). Following illumination, *R* was found to change less than 10% over 24 hours when the sample was kept in vacuum or dry air (Fig. 6.1c), but the presence of ambient humidity accelerated the upward drift in *R* (Fig 6.1d), suggesting that water is playing a role in the light-driven process. Importantly, owing to the observed light sensitivity, samples were not exposed to light with wavelengths below 520 nm unless otherwise noted.

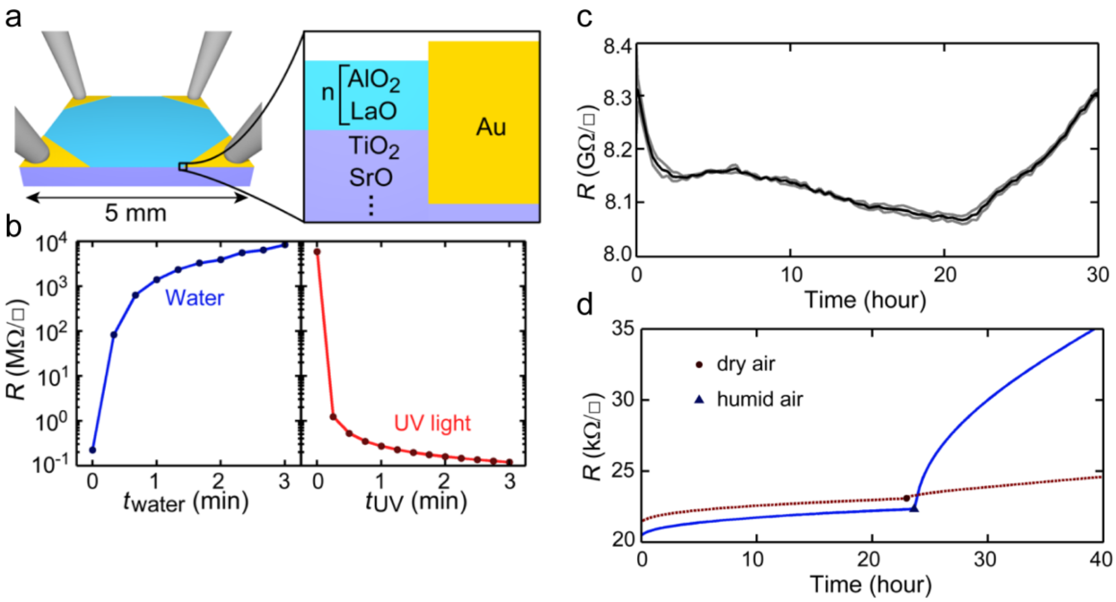

Figure 6.1 Observation of a reversible MIT transition by exposure to water and light. a, Schematic showing the bulk electrical transport measurement of 4 unit cell LAO/STO. **b,** Sheet resistance *R* as determined by a van der Pauw measurement vs. total time exposed to deionized water (t_{water}, left) and total time exposed to broadband light (t_{UV}, right). **c,** Transient response of *R* following immersion in water for 3 min and being blown dry using N_2. This sample was measured in the dark under ambient atmosphere. The grey lines indicate upper and lower bounds of measurement uncertainty. **d,** Transient response of *R* after UV exposure in vacuum followed by introduction of dry air (dashed line; circle denotes when air is introduced) and air at 30% relative humidity (solid line; triangle denotes when air is introduced). Measurement uncertainty is smaller than marker size.

6.3.2 XPS study of LAO surface protonation

To evaluate the chemical changes that correspond to the conductivity switching, XPS was employed [205]. XPS measurements were performed in a commercial spectrometer (Thermo Scientific ESCALAB 250Xi) with a monochromated Al Kα radiation source and care taken to avoid exposure to visible light. The electron flood gun was turned on in order to reduce surface charging. The pressure in the vacuum chamber during the analysis was less than 10^{-9} bar. Each scan was recorded as the average of five sequential scans. Each sample was measured in three distinct areas to establish statistical error bars for the measurements. After scanning, all the binding energies (BEs) were referenced to the adsorbed carbon C1s peak, which was set to 284.8 eV. Fitting was performed via an automated routine implemented in MATLAB wherein the bands were fit to a sum of Gaussian peaks plus a linear background. For example, the O1s region was fit to the sum of three Gaussians. This number was chosen because this is the maximum number that appreciably affected the mean square error. The peak widths were constrained to be the same for all peaks in a given scan and were found to be 1.02 ± 0.05 eV for all measurements.

The O1s peak was found to be descriptive of the chemical status of the LAO surface (Fig. 6.2a), as it exhibited peaks from three discernable species: fully coordinated lattice oxygen (M-O-M), protonated oxygen (M-OH), and oxygen in adsorbed water (H_2O). A 4 uc LAO sample was subjected to a series of UV and water treatments while alternatively measuring *R* and chemical composition (Fig. 6.2d-g). In all cases, exposure to light caused the M-O-M peak area to decrease relative to M-OH while water immersion displayed the opposite effect. Interestingly, the area of the H_2O peak tracks the M-OH peak, suggesting that the protonated surface binds more strongly to water (Fig. 6.2g). The XPS assignments are supported by literature [206] and a tilting experiment (Fig. 6.2 f-k). The Al/Sr peak area ratio increases with increasing tilt (Fig. 6.2h), confirming that Al is closer to the surface. As the tilt increases, the measured concentration of M-O-M (Fig. 6.2i) decreases, while the measured concentrations of M-OH (Fig 6.2j), and H_2O (Fig. 6.2k) increase, thus suggesting that the M-OH and H_2O species are localized to the surface.

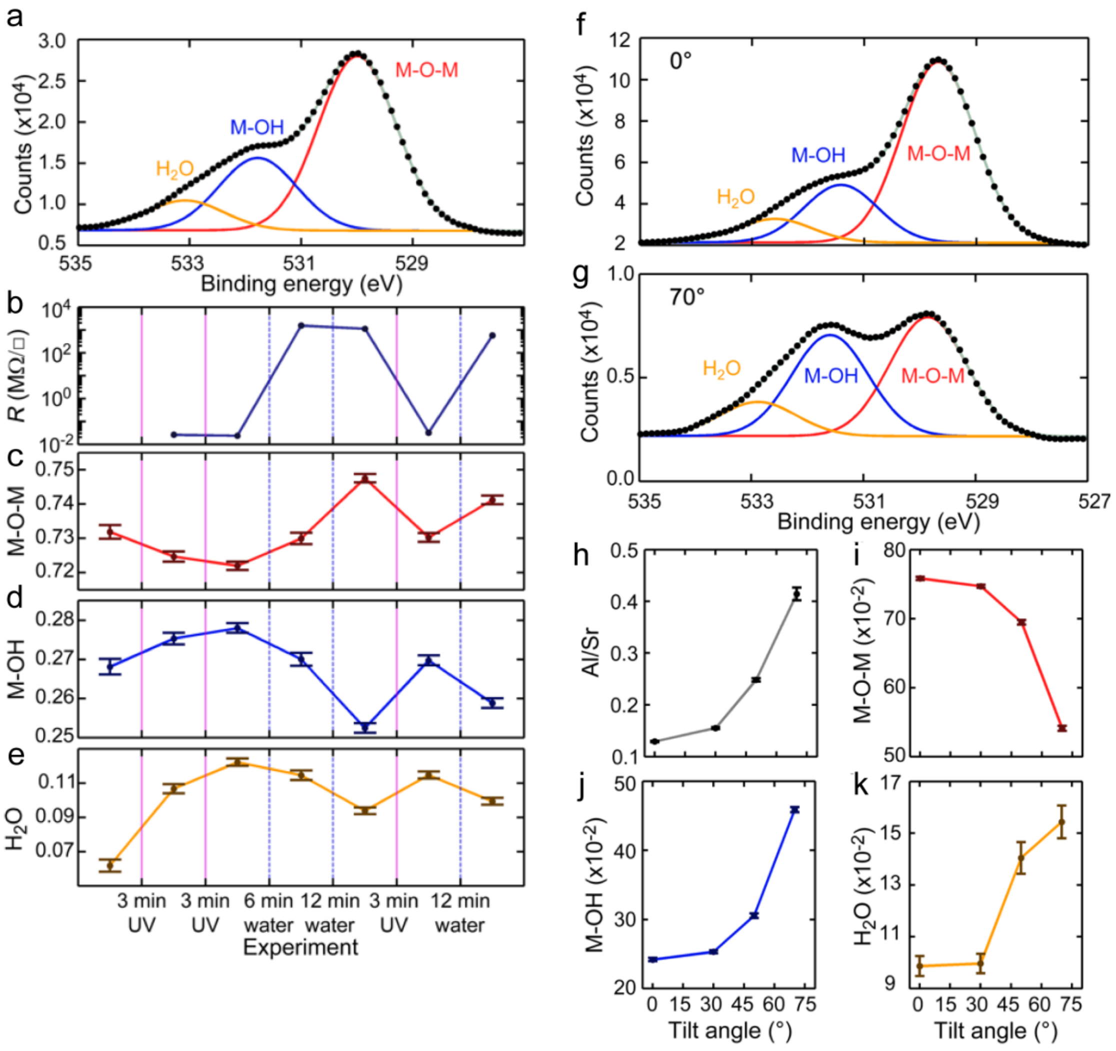

Figure 6.2 X-ray photoelectron spectroscopy (XPS) investigation. a XPS of 4 uc LAO/STO showing the O1s region. **b** R measured following each treatment, with optical excitation denoted by solid purple lines and water treatment denoted by dashed blue lines. Here uncertainty is smaller than marker size. Evolution of areas of M-O-M **c**), M-OH (**d**), and H2O (**e**) peaks normalized by the sum of M-O-M and M-OH measured while the sample was subjected to optical excitation and water immersion. XPS of 4 uc LAO on STO showing the O1s region at 0 ° tilt (**f**) and 70 ° tilt (**g**). As the tilt increases, The Al/Sr peak area ratio increases (**h**), and the concentration of M-O-M (**i**) decreases, while the measured concentrations of M-OH (**e**), and H_2O (**f**) increase. The peak areas for (**i-g**) are normalized by the sum of M-O-M and M-OH.

Although the XPS measurement only provided ratiometric information, the optical absorbance measured by spectroscopic ellipsometry (M-2000 - J.A. Woollam Co. Inc.) at 55°, 65°, and 75 ° from normal incidence did not appreciably change following illumination or solvent immersion (Fig 6.3). The resulting angles were used to compute a real (Fig 6.3a) and imaginary refractive index (Fig 6.3b). Note that there was no appreciable change following immersion in water or exposure to light. Alignment was performed through a 500 nm long pass filter to prevent triggering the light-driven transition.

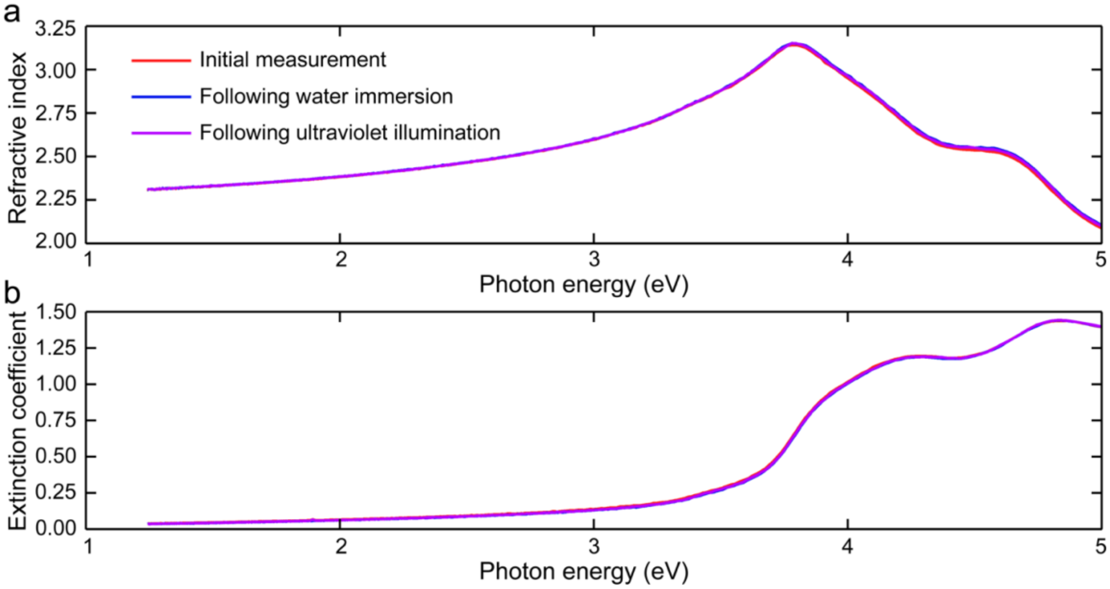

Figure 6.3 Spectroscopic ellipsometry of LAO/STO interfaces. The real (**a**) and imaginary (**b**) indices of refraction were extracted by modeling the interface as a homogenous material. Initial measurement (red), measurement following 3 min of immersion in DI water (blue), and measurement following 3 min of illumination under the light source used all showed superimposable curves.

The optical absorbance results suggest that the number of optically active oxygen vacancies is static during these treatments and that the change measured by XPS is due to a change in the protonation state of the LAO surface [207]. It is important to emphasize that optical characterization techniques (for example, XPS and ellipsometry) must be used with caution to study LAO/STO. Specifically, XPS measurements were found to return insulating samples to a conductive state, so it was important to perform XPS after measuring electrical transport. In light of this perturbative effect, XPS should be considered a qualitative measure of surface protonation.

Despite these limitations, we consistently observed the trend of protonation increasing with light exposure and decreasing with solvent immersion. We recommend that future studies focus on the use of alternative analytical surface tools such as scanning tunneling microscopy to provide a more detailed and quantitative picture of the chemical state of the surface.

The combination of XPS and electrical transport measurements suggests that interface conductivity increases with surface protonation. Although this trend is in agreement with first principles theoretical studies [113], immersion in water deprotonating the LAO surface is in apparent contradiction to studies in which water immersion was observed to increase protonation [78]. Thus, an extensive series of experiments were designed to test what properties of solvents drove the conductor to insulator transition.

6.3.3 Solvent and light wavelength dependence

To test the hypothesis that surface protonation dictates interface conductivity, we explored the effect of solvent pH on the conductivity of 4 uc samples (Fig. 6.4a). Following initialization in a conductive state, R was measured before and after immersion in an aqueous solution of sulfuric acid for 1 minute and subsequent drying. Interestingly, lowering the pH of the immersion solution from 7 to 3 decreased the magnitude of conductive switching over 100-fold, suggesting that immersion drives an acid-base reaction where water acts as a Lewis base and removes protons from the surface. This pH range was selected because the isoelectric point of crystalline aluminum oxide is pH ~ 5 [208], thus one would expect the surface charge of LAO to vary greatly between pH 3 and 7. To ensure that the effect was not related to the sulfate counterion, the sample was immersed in a sodium sulfate solution that was isomolar with pH < 2 sulfuric acid. Immersion in this salt solution increased R more than immersion in pH 7 water, indicating that pH is likely determining the observed conductivity change rather than the anionic counterions.

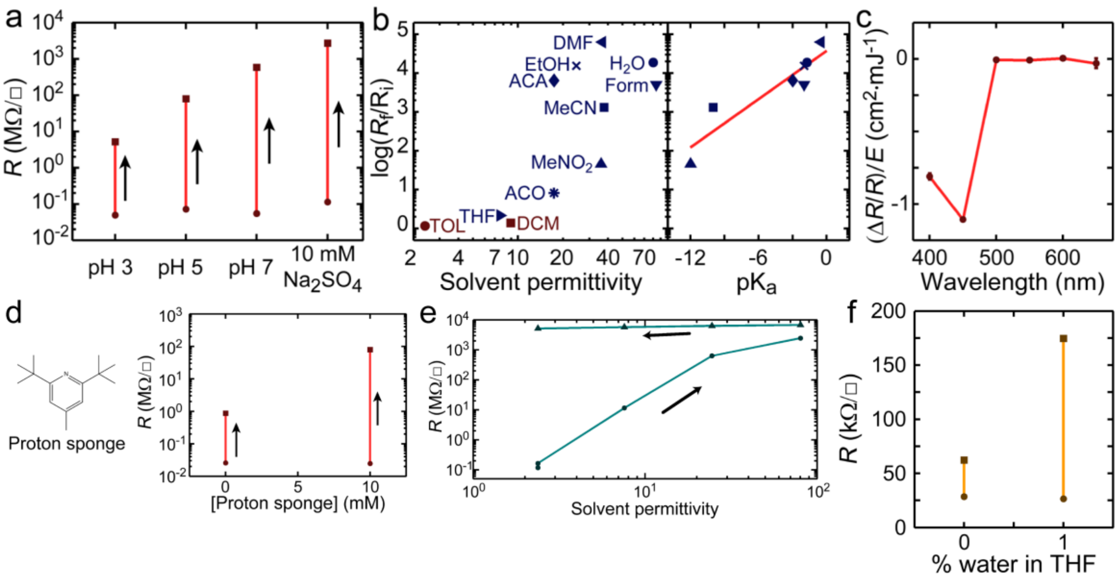

Figure 6.4 Effects of solvent and light wavelength on the conductivity switching in LAO/STO. a *R* of 4 uc LAO/STO measured before (circles) and after (squares) 1-minute immersion in solvents with varying concentrations of free protons. **b,** (left) Ratio of the resistance R_f measured following a 2-minute immersion in toluene (TOL), tetrahydrofuran (THF), dichloromethane (DCM), acetophenone (ACO), acetaldehyde (ACA), ethanol (EtOH), nitromethane (MeNO2), dimethylformamide (DMF), acetonitrile (MeCN), water (H_2O) or formamide (Form) to the resistance in the conductive state R_i. Blue and red markers represent solvents that do and do not function as Lewis bases, respectively. (right) Rf/Ri vs. the pKa of the protonated solvents. **c,** Ratio of sheet resistance change *ΔR* to *R* normalized by the delivered optical energy *E* following illumination with light of a specified wavelength. **d,** *R* of 4 uc LAO/STO measured following two minute immersions in nitromethane with the “proton sponge” 2,6-di-tert-butyl-4-methylpyridine. **e,** *R* of 4 uc LAO/STO measured following sequential one minute immersions in solvents with different relative permittivities (toluene, tetrahydrofuran, ethanol, and deionized water). **f,** *R* of 4 uc LAO/STO measured before and after two minute immersions in pure tetrahydrofuran (THF) or 1:99 DI water:THF by volume.

If LAO/STO interface conductivity is dictated by surface protonation, then immersion in solvents besides water can deprotonate the surface should have an analogous effect. Thus, a series of experiments was performed in which a conductive 4 uc sample was immersed in one of various solvents for 2 minute (Fig. 6.4b left). Interestingly, only Lewis basic solvents were found to drive conductivity switching; this observation is in support of deprotonation as the mechanism of conductivity switching during solvent immersion. More generally, solvents with relative permittivity $\varepsilon \lesssim 20$ had a small effect while those with $\varepsilon > 20$ substantially changed R. This result can be understood by considering that lower permittivity solvents are less able to screen the charge of the protons and overcome the electrostatic attraction between the protons and the electrons in the 2DEL. Importantly, while the resistance increase from immersion in high permittivity solvents did not correlate with solvent permittivity, it correlated extremely well with the pK_a of the protonated solvent (*i.e.* $BH^+ \rightarrow B + H^+$) (Fig. 6.4b – right), strongly suggesting that the mechanism is dependent upon an acid-base reaction in which the solvent accepts a proton from the surface. In further support of this hypothesis, while nitromethane immersion only increased R 30-fold, the addition of 10 mM of a proton sponge to nitromethane resulted in a solution that increased R 3,000-fold (Fig. 6.4d), indicating that the ability to accept protons is critical for this process. Furthermore, once the sample was prepared in the insulating state, sequential solvent immersion did not appreciably decrease R (Fig 6.4e). Care was taken to dry solvents before use, as even the addition of 1% water to tetrahydrofuran was found to triple the effect of immersion (Fig 6.4f).

Although it is plausible that solvent immersion can deprotonate a surface, it is not straight forward that light would reverse this process. In an effort to explore this photoconductivity effect, a 4 uc sample prepared in an insulating state was exposed to monochromatic light of various wavelengths (Fig. 6.4c). While R did not vary when illuminated by light at wavelengths ≥ 500 nm, illumination at wavelengths < 450 nm decreased R. Interestingly, 450 nm photons do not have enough energy to overcome the band gap of either LAO or STO, but oxygen vacancies in STO have optically active transitions between 400 and 460 nm [209,210], implicating these defect states in the persistent photoconductivity.

6.4 POSSIBLE MODEL

Based upon these observations, we postulate a surface protonation-based mechanism for the role of solvent immersion and exposure to light in LAO/STO interfaces (Fig. 6.5). Specifically, the cycle consists of a chemical change of the protonation state of LAO and an electronic change, in which an electron is exchanged with the environment. Initially, the sample is in the conductive state and the LAO surface is protonated (Fig. 6.5a). Solvent immersion deprotonates the surface through an acid-base reaction, removing the source of electrostatic attraction that holds electrons at the interface. Thus, an electron leaves the system either through the electrodes or through exchange with the solvent at the leads. With the interface state vacant, the system is insulating (Fig. 6.5b). Based upon the spectral dependence of the persistent photoconductivity and well-documented presence of oxygen vacancies near the LAO/STO interface,[211] we postulate that exposing the insulating surface to light excites oxygen vacancies at or near the LAO/STO interface. These photo-generated electron-hole pairs are split because the polar potential in the LAO drives the hole toward the LAO surface (Fig. 6.5c). Once on the surface, the hole is able to accept an electron from an adsorbed water molecule through the oxidative water splitting reaction, $1/2H_2O \rightarrow H^+ + 1/4O_2 + e^-$ (Fig. 6.5d), in analogy to the photocatalytic splitting of adsorbed water observed for many perovskite oxides [212,213]. Importantly, this process completes both the chemical and electronic cycle by annihilating the hole, thus preventing subsequent electron-hole recombination and creating a proton which is free to associate with Lewis basic sites on the LAO surface (Fig. 6.5a).

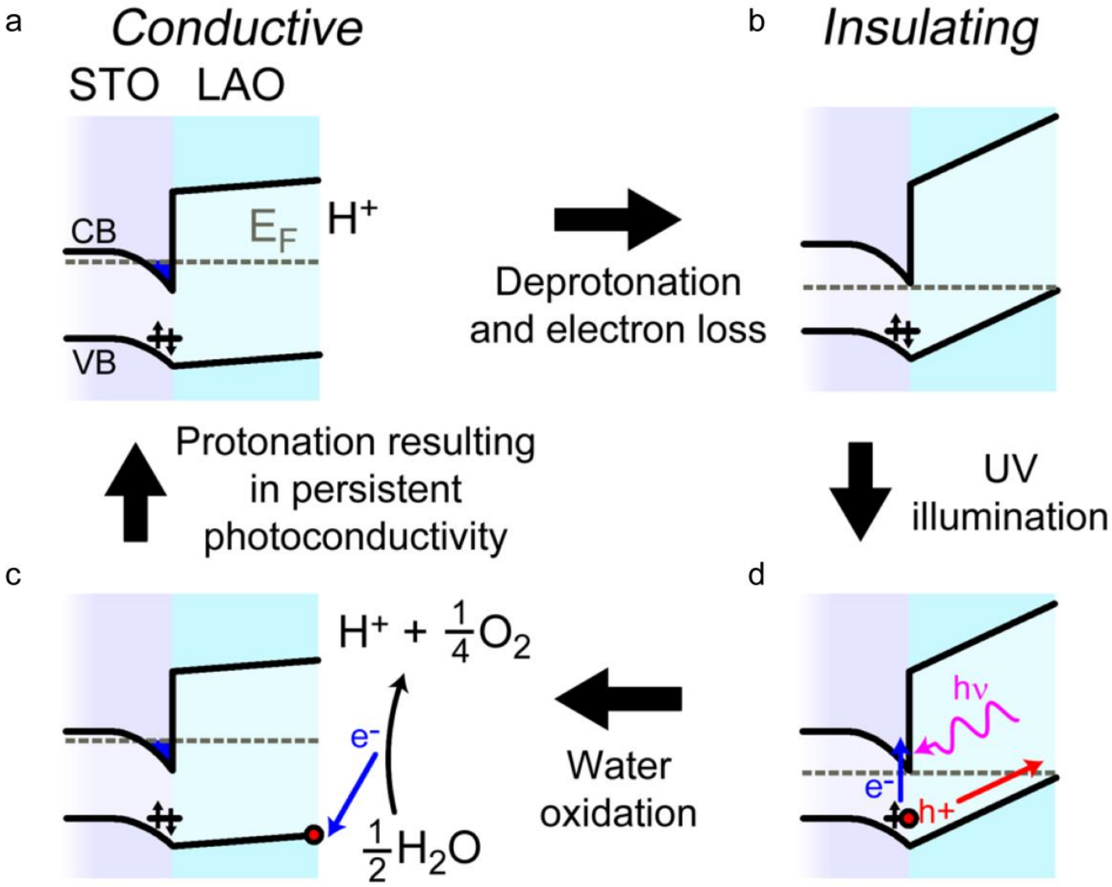

Figure 6.5 Model of giant conductivity switching in LAO/STO. a, Initially, the conducting band (CB) and valence band (VB) of the LAO/STO interface bend to create an occupied conductive state at the interface. In addition, a mid-gap oxygen vacancy state in the STO is present below the Fermi energy EF. **b,** Solvent immersion removes the proton and causes the electron to leave the interface. **c,** UV light creates electron-hole pairs at the oxygen vacancy, which are separated by the polar LAO potential. Specifically, the hole "bubbles up" the VB potential in the LAO and segregates to the surface. **d,** The surface hole oxidizes adsorbed water, thereby generating a proton. This proton can then interact with Lewis basic sites of the LAO.

6.5 LAO FILM THICKNESS DEPENDENCE

If surface chemistry, rather than band bending, is playing a dominant role in 2DEL formation, then the observed resistivity switching should persist beyond the reported 4 uc critical thickness. To explore this hypothesis, we performed a series of experiments testing the effects of water immersion and illumination on samples with 4, 5, 6, 7 and 8 uc of LAO. Samples were subjected to sequential 30 second immersions in DI water for a total of 3 minutes followed by 15 second exposures to light for a total of 3 minutes (Fig. 6.6). Surprisingly, the 5 uc sample exhibited a three order of magnitude shift in R and the 6 uc sample exhibited a two order of magnitude shift in R. These results support early theoretical work in which the critical thickness was computed to be ~ 6 uc and it was hypothesized that the experimentally observed critical thickness of 4 uc was due to defects or surface adsorbates [84]. Although experimental limitations prevented us from observing changes in transport properties faster than the scale of seconds, the fast dynamics of this transition represent a fascinating opportunity for further study.

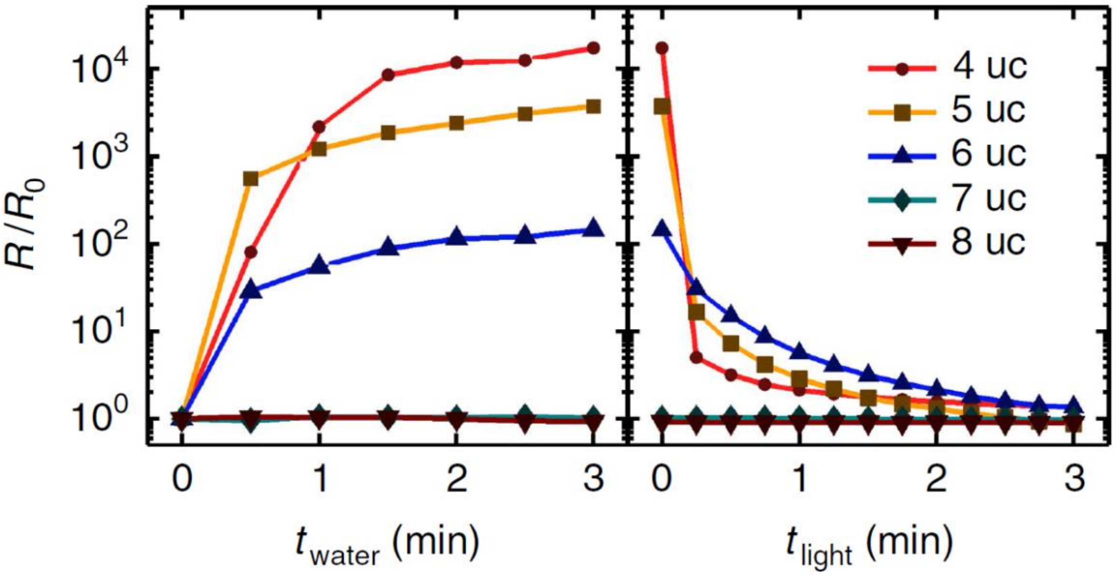

Figure 6.6 LAO thickness effect on conductivity switching. R vs. t_{water} (left) and t_{UV} (right) are measured for LAO/STO samples with different numbers of unit cells of LAO. Measurement uncertainty is smaller than the data markers in all cases. t_{water} and t_{UV} indicate cumulative exposure to water and light, respectively. R is normalized by the value before the first water immersion $R_0 = R(t_{\text{water}} = 0)$. The data corresponding to the 7 uc and 8 uc samples are difficult to distinguish because neither deviates more than 10% away from unity.

6.6 TEMPERATURE DEPENDENT TRANSPORT

In order to further explore the light induced conductivity, a 4 uc LAO/STO sample was exposed to broadband light for 3 minutes and subsequently loaded into a Physical Properties Measurement System (PPMS – Quantum Design). Van der Pauw and magnetotransport measurements were carried out in the temperature range 10 K to 300 K to determine the sheet resistance R, carrier density n_s, and mobility μ. The transport measurement revealed a smoothly varying mobility and carrier density (Fig 6.7) commensurate with previous measurements of LAO/STO samples. These observations are consistent with the picture that solvent immersion renders the LAO/STO heterointerface insulating and exposure to light recovers the conductivity.

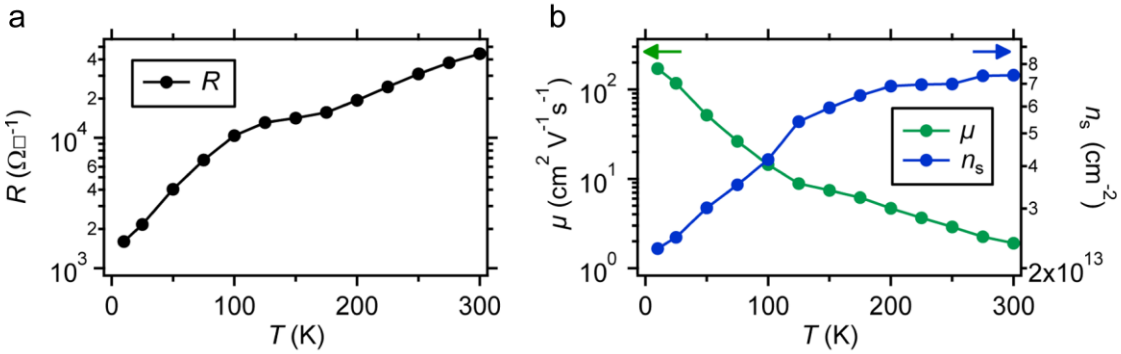

Figure 6.7 Temperature dependent transport measurements. a, Temperature dependence of sheet resistance *R* of a 4 uc LAO/STO sample measured after the sample was exposed to broadband light for 3 minutes. **b,** Temperature dependence of mobility μ and carrier density n_s of a 4 uc LAO/STO sample measured after the sample was exposed to broadband light for 3 minutes**.**

6.7 PHOTO PATTERNING EXPERIMENT

The ability to reversibly switch the conductivity of LAO/STO interfaces through solvent immersion and exposure to light suggests several approaches for realizing large-scale reconfigurable nanoscale patterning of conductive areas. Indeed, preliminary experiments demonstrate that photo patterning can achieve a >2 order of magnitude ratio between the resistance of the patterned and unpatterned regions using standard photolithography (Fig 6.7). The essential role that surface chemistry plays in mediating 2DEL formation implies that the full diversity of synthetic chemistry may be utilized to design self-assembled monolayers that precisely tune the 2DEL. Taken together, this work provides compelling experimental evidence for surface protonation playing a major role in the conductivity of LAO/STO interfaces and illustrates how this phenomena can be modulated using solvent immersion and illumination.

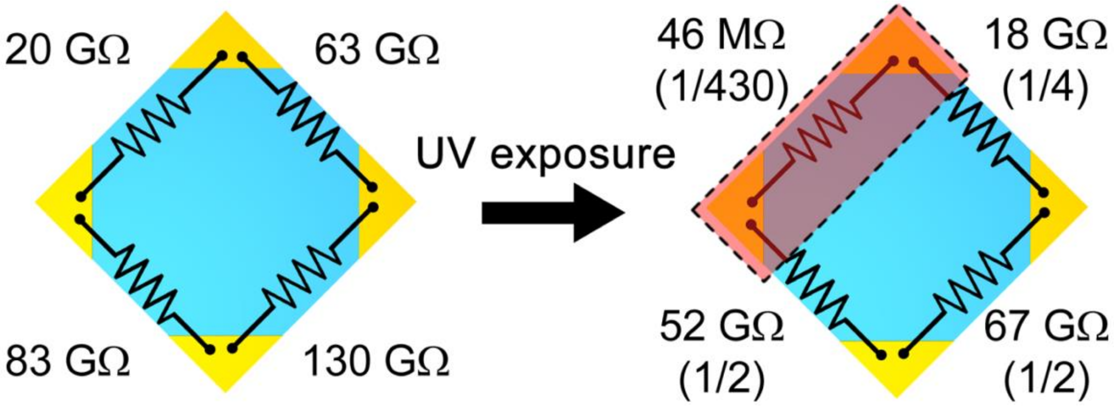

Figure 6.8 Patterning LAO/STO samples using the surface-driven insulator-to-conductor transition. Two terminal resistances measured between each neighboring pad for a 4 uc LAO on STO sample following immersion in water (left) and after one edge of the sample was exposed to UV light (right). The ratios indicate the change in resistance for each measurement.

6.8 DISCUSSION AND CONCLUSIONS

Here we report a large (> 4 order of magnitude) reversible switching of the LAO/STO interface conductivity in response to solvent immersion and optical illumination. Through coordinated electrical measurements, XPS and solvent immersions, we find that LAO/STO conductivity is correlated with the protonation of the LAO surface. Furthermore, by immersing the samples in various solutions including different pH aqueous solutions, solvents with a range of pK_a, and solutions of molecules that function as proton sponges, we find that a solvent's ability to render the LAO/STO layer insulating is dictated by its ability to deprotonate the LAO surface. Based on these results, we propose a model in which LAO surface protonation dictates the electronic state of the LAO/STO interface. In support of this, we find that this effect diminishes as the LAO film thickness is increased until it effective disappears in LAO films 7 uc thick. Finally, we find that the conductive state can be directly patterned by illuminating selected regions of the LAO/STO surface, suggesting a future method for realizing reconfigurable electronic based upon LAO/STO interface.

In apparent contrast to our observations, a prior study has shown that solvent immersion renders LAO/STO heterointerfaces somewhat more conductive (that is, doubling the conductivity) [94]. This discrepancy could be due to two factors: first, in the in the prior work, it was not stated whether or not the experiments were performed in the dark; however, some experimental variations were attributed to ‘fluctuations in the local illumination.’ Second, the study focused on 10 uc LAO/STO, which we expect to have a small variation with solvent immersion (extrapolating from Fig 6.6). The only experiment reported on samples with less than 10 uc of LAO utilized acetone, which we expect to have a modest effect both due to the low permittivity of the solvent (~ $20\varepsilon_0$) and the short duration of immersion (10 s). When we replicated these conditions (immersing a conductive 4 uc sample in acetone for 10 s) but kept the sample in the dark, we observed a mere 84% increase in R. Thus, we attribute illumination details and choice of immersion conditions to be the cause of the apparent inconsistency with previous work.

It is also worth addressing how this phenomenon could not have been observed previously despite many groups using solvent immersion as part of their fabrication processes. Ultimately, it is easy to expose a sample to enough adventitious light that the conductive state is restored despite a prior solvent immersion. In particular, samples stored in a transparent container overnight in normal workplace illumination conditions would commonly appear fully conductive.

Although XPS is used here as a qualitative measurement owing to its interaction with the surface, the abundance of protonated oxygen only changed by ~5%. This naturally raises the question: what change in surface protonation is required to drive the metal to insulator transition? Given that LAO/STO is a system characterized by small changes in parameters (for example, gate voltage, LAO film thickness) producing dramatic effects on electronic transport [48], it will be fascinating to complement these experiments with quantitative measurements of surface protonation.

7.0 SUMMARY AND PERSPECTIVE

In this thesis, we use local probes—nanodevices and nanostructures created by c-AFM lithography as well as the AFM itself, to investigate the fascinating emergent phenomena in LAO/STO, one prototype complex-oxide heterostructure. We applied a non-local PFM technique to study the electromechanical response of LAO/STO and built a connection between the PFM response and local carrier density at the interface as well as LAO surface chemical environment. We also used the non-local PFM technique to image the nanostructures created by c-AFM lithography at LAO/STO interface. Future experiments can be employing the PFM method to study a single electron transistor at low temperature, since the PFM can resolve local carrier density and reveal the coupling between the electronic and mechanical response.

We integrated single layer graphene onto LAO/STO and expanded our study from complex oxide heterostructures to graphene/complex oxides (GCO). We developed a standard method to transfer CVD-grown graphene into LAO/STO and patterning it using photolithography and c-AFM lithography. Our c-AFM lithography technique can still make conducting nanostructures (e.g. nanowires) at the LAO/STO interface covered by single layer graphene without degrading the high quality graphene. Field effect GCO devices were demonstrated and exhibit quantum transport signature at room temperature, e.g. half-integer quantum hall effect and weak antilocalization. We are developing a new graphene pattern method using photoresist and Hyflon layer instead of PMMA to achieve more precise control of the graphene layer shape and position, as well as cleaner sample surface. Future experiments can be using c-AFM lithography to created nanostructures (e.g. nanoscale superlattices structure) at graphene or LAO/STO interface to further exploring the transport properties. Another research direction of graphene/LAO/STO is study its optical properties since both graphene and LAO/STO interface can generate THz radiations. The coupling between the top graphene layer and the LAO/STO interface plays critical roles in both the transport and optical experiments.

We investigated the quasi-1D transport properties of nanowires at (110)-oriented LAO/STO interface. We observed anisotropic superconducting properties along the two crystal orientations—(1-10) and (001) and a superconducting dome shift between the two directions. We proposed a possible scenario involving anisotropic band structures and Lifshiz transition to explain our data. In future all the transport studies done in the regular (001)-oriented LAO/STO can migrate into the (110)-oriented LAO/STO with a twist of the anisotropic in-plan crystal orientations. Local inhomogeneity can also play a role in the anisotropic behavior since our nanowire sections are not in the same region. To rule out the local inhomogeneity effect, future experiments can be measuring the conductance along different directions within one nanodevice .

The surface chemical environment of LAO/STO can significantly affect the interface properties and we systematically studied and conductance switching under light illumination and solvent rinsing. We established a surface protonation procedure can tune the interface conductance by over 4 orders of magnitude in 4 uc LAO/STO. This effect become weaker as LAO thickness increase and finally disappear for over 7 uc LAO/STO. Our discovery shed more lights onto the formation mechanism of the conducting LAO/STO interface and can be used to photo pattern the interface. Further exploration can be completing these experiments with quantitative measurements of surface protonation.

Besides the four main research projects, I also actively involved in other projects, like magnetism study in LAO/STO, various transport study in LAO/STO, THz generation and detection in LAO/STO, Gigahertz-frequency operation of LAO/STO-based nanotransistors, Parallel c-AFM lithography in LAO/STO, field effect and tunneling properties investigation of *in-situ* Au/LAO/STO; transport study of amorphous LAO/STO heterostructures and LAO/MBE-grown STO on STO substrates. The large range of the projects I involved is due to the rich spectrum of physics at LAO/STO, which has attracted intensive investigations. Our local probes can create nanostructure and study these emergent phenomena in nanoscale, which is even more attracting since the 1D and 0D confinements will result in more exotic behaviors. The research path in complex oxides never ends and gets even wider by combining complex oxides with other novel material, e.g. graphene, transition metal dichalcogenides etc. Our research can provide the physics foundation for potential future technologies, e.g. incorporation of functional oxide heterostructures into electronic circuits, quantum simulation in solid-state platform and even quantum computation.

BIBLIOGRAPHY

[1] Kroemer, H. Nobel Lecture: Quasielectric fields and band offsets: teaching electrons new tricks. *Rev Mod Phys* **73**, 783-793, (2001).

[2] Hwang, H. Y. *et al.* Emergent phenomena at oxide interfaces. *Nat Mater* **11**, 103-113, (2012).

[3] Mannhart, J. & Schlom, D. G. Oxide interfaces--an opportunity for electronics. *Science* **327**, 1607-1611, (2010).

[4] Packan, P. A. Perspectives: Device physics - Pushing the limits. *Science* **285**, 2079-+, (1999).

[5] Podkaminer, J. P. *et al.* Creation of a two-dimensional electron gas and conductivity switching of nanowires at the LaAlO3/SrTiO3 interface grown by 90 degrees off-axis sputtering. *Appl Phys Lett* **103**, (2013).

[6] The interface is still the device. *Nat Mater* **11**, 91-91, (2012).

[7] Chakhalian, J., Millis, A. J. & Rondinelli, J. Whither the oxide interface. *Nat Mater* **11**, 92-94, (2012).

[8] Sulpizio, J. A., Ilani, S., Irvin, P. & Levy, J. Nanoscale Phenomena in Oxide Heterostructures. *Annu Rev Mater Res* **44**, 117-149, (2014).

[9] Muller, K. A., Berlinge.W & Waldner, F. Characteristic Structural Phase Transition in Perovskite-Type Compounds. *Phys Rev Lett* **21**, 814-&, (1968).

[10] Fleury, P. A., Scott, J. F. & Worlock, J. M. Soft Phonon Modes and 110 Degrees K Phase Transition in Srtio3. *Phys Rev Lett* **21**, 16-&, (1968).

[11] Lytle, F. W. X-Ray Diffractometry of Low-Temperature Phase Transformations in Strontium Titanate. *J Appl Phys* **35**, 2212-&, (1964).

[12] Muller, K. A. & Burkard, H. Srtio3 - Intrinsic Quantum Para-Electric Below 4-K. *Phys Rev B* **19**, 3593-3602, (1979).

[13] Rytz, D., Hochli, U. T. & Bilz, H. Dielectric Susceptibility in Quantum Ferroelectrics. *Phys Rev B* **22**, 359-364, (1980).

[14] Sakudo, T. & Unoki, H. Dielectric Properties of Srtio3 at Low Temperatures. *Phys Rev Lett* **26**, 851-&, (1971).

[15] Haeni, J. H. *et al.* Room-temperature ferroelectricity in strained $SrTiO_3$. *Nature* **430**, 758-761, (2004).

[16] Luo, W. D., Duan, W. H., Louie, S. G. & Cohen, M. L. Structural and electronic properties of n-doped and p-doped SrTiO3. *Phys Rev B* **70**, (2004).

[17] Ueno, K. *et al.* Electric-field-induced superconductivity in an insulator. *Nat Mater* **7**, 855-858, (2008).

[18] Schooley, J. F., Hosler, W. R. & Cohen, M. L. Superconductivity in Semiconducting Srtio3. *Phys Rev Lett* **12**, 474-+, (1964).

[19] Koonce, C. S., Cohen, M. L., Schooley, J. F., Hosler, W. R. & Pfeiffer, E. R. Superconducting Transition Temperatures of Semiconducting Srtio3. *Phys Rev* **163**, 380-&, (1967).

[20] Brinkman, A. *et al.* Magnetic effects at the interface between non-magnetic oxides. *Nat Mater* **6**, 493-496, (2007).

[21] Lee, J. S. *et al.* Titanium d_{xy} ferromagnetism at the $LaAlO_3/SrTiO_3$ interface. *Nat Mater* **12**, 703-706, (2013).

[22] Ariando *et al.* Electronic phase separation at the LaAlO(3)/SrTiO(3) interface. *Nat Commun* **2**, 188, (2011).

[23] Bi, F. *et al.* Room-temperature electronically-controlled ferromagnetism at the $LaAlO_3/SrTiO_3$ interface. *Nat Commun* **5**, 5019, (2014).

[24] Hayward, S. A. *et al.* Transformation processes in LaAlO3: Neutron diffraction, dielectric, thermal, optical, and Raman studies. *Phys Rev B* **72**, (2005).

[25] Delugas, P., Fiorentini, V. & Filippetti, A. Dielectric properties and long-wavelength optical modes of the high-kappa oxide LaAlO3. *Phys Rev B* **71**, (2005).

[26] Simon, R. W. *et al.* Low-Loss Substrate for Epitaxial-Growth of High-Temperature Superconductor Thin-Films. *Appl Phys Lett* **53**, 2677-2679, (1988).

[27] Yang, W. H., Hou, D. S., Li, C. Z., Fan, H. & Zhang, H. Y. Laalo3 Single-Crystal Substrate for Epitaxial Superconducting Thin-Films. *Solid State Commun* **75**, 421-424, (1990).

[28] Chakoumakos, B. C., Schlom, D. G., Urbanik, M. & Luine, J. Thermal expansion of LaAlO3 and (La,Sr)(Al,Ta)O-3, substrate materials for superconducting thin-film device applications. *J Appl Phys* **83**, 1979-1982, (1998).

[29] de Ligny, D. & Richet, P. High-temperature heat capacity and thermal expansion of SrTiO3 and SrZrO3 perovskites. *Physical review. B, Condensed matter* **53**, 3013-3022, (1996).

[30] Ohtomo, A. & Hwang, H. Y. A high-mobility electron gas at the $LaAlO_3/SrTiO_3$ heterointerface. *Nature* **427**, 423-426, (2004).

[31] Herranz, G., Sanchez, F., Dix, N., Scigaj, M. & Fontcuberta, J. High mobility conduction at (110) and (111) LaAlO3/SrTiO3 interfaces. *Sci Rep-Uk* **2**, (2012).

[32] Annadi, A. *et al.* Anisotropic two-dimensional electron gas at the LaAlO(3)/SrTiO(3) (110) interface. *Nat Commun* **4**, 1838, (2013).

[33] Chen, Y. Z. *et al.* Metallic and Insulating Interfaces of Amorphous SrTiO3-Based Oxide Heterostructures. *Nano Lett* **11**, 3774-3778, (2011).

[34] Lee, S. W., Liu, Y., Heo, J. & Gordon, R. G. Creation and control of two-dimensional electron gas using Al-based amorphous oxides/SrTiO(3) heterostructures grown by atomic layer deposition. *Nano Lett* **12**, 4775-4783, (2012).

[35] Zhong, Z. C., Toth, A. & Held, K. Theory of spin-orbit coupling at LaAlO3/SrTiO3 interfaces and SrTiO3 surfaces. *Phys Rev B* **87**, (2013).

[36] Popovic, Z. S., Satpathy, S. & Martin, R. M. Origin of the two-dimensional electron gas carrier density at the LaAlO3 on SrTiO3 interface. *Phys Rev Lett* **101**, 256801, (2008).

[37] Salluzzo, M. *et al.* Orbital reconstruction and the two-dimensional electron gas at the LaAlO3/SrTiO3 interface. *Phys Rev Lett* **102**, 166804, (2009).

[38] Pesquera, D. *et al.* Two-dimensional electron gases at LaAlO3/SrTiO3 interfaces: orbital symmetry and hierarchy engineered by crystal orientation. *Phys Rev Lett* **113**, 156802, (2014).

[39] Herranz, G. *et al.* Engineering two-dimensional superconductivity and Rashba spin-orbit coupling in LaAlO3/SrTiO3 quantum wells by selective orbital occupancy. *Nat Commun* **6**, (2015).

[40] Wang, Z. *et al.* Anisotropic two-dimensional electron gas at SrTiO3(110). *Proc Natl Acad Sci U S A* **111**, 3933-3937, (2014).

[41] Santander-Syro, A. F. *et al.* Two-dimensional electron gas with universal subbands at the surface of SrTiO(3). *Nature* **469**, 189-193, (2011).

[42] Son, W. J., Cho, E., Lee, B., Lee, J. & Han, S. Density and spatial distribution of charge carriers in the intrinsic n-type LaAlO3-SrTiO3 interface. *Phys Rev B* **79**, (2009).
[43] Delugas, P. *et al.* Spontaneous 2-Dimensional Carrier Confinement at the n-Type SrTiO3/LaAlO3 Interface. *Phys Rev Lett* **106**, (2011).
[44] Basletic, M. *et al.* Mapping the spatial distribution of charge carriers in LaAlO(3)/SrTiO(3) heterostructures. *Nat Mater* **7**, 621-625, (2008).
[45] Sing, M. *et al.* Profiling the interface electron gas of LaAlO3/SrTiO3 heterostructures with hard x-ray photoelectron spectroscopy. *Phys Rev Lett* **102**, 176805, (2009).
[46] Fix, T., Schoofs, F., MacManus-Driscoll, J. L. & Blamire, M. G. Charge Confinement and Doping at LaAlO3/SrTiO3 Interfaces. *Phys Rev Lett* **103**, (2009).
[47] Caviglia, A. D. *et al.* Electric field control of the LaAlO3/SrTiO3 interface ground state. *Nature* **456**, 624-627, (2008).
[48] Thiel, S., Hammerl, G., Schmehl, A., Schneider, C. W. & Mannhart, J. Tunable quasi-two-dimensional electron gases in oxide heterostructures. *Science* **313**, 1942-1945, (2006).
[49] Cen, C. *et al.* Nanoscale control of an interfacial metal-insulator transition at room temperature. *Nat Mater* **7**, 298-302, (2008).
[50] Reyren, N. *et al.* Superconducting interfaces between insulating oxides. *Science* **317**, 1196-1199, (2007).
[51] Li, L., Richter, C., Mannhart, J. & Ashoori, R. C. Coexistence of magnetic order and two-dimensional superconductivity at $LaAlO_3/SrTiO_3$ interfaces. *Nat Phys* **7**, 762-766, (2011).
[52] Bert, J. A. *et al.* Direct imaging of the coexistence of ferromagnetism and superconductivity at the LaAlO3/SrTiO3 interface. *Nat Phys* **7**, 767-771, (2011).
[53] Dikin, D. A. *et al.* Coexistence of Superconductivity and Ferromagnetism in Two Dimensions. *Phys Rev Lett* **107**, (2011).
[54] Ben Shalom, M., Sachs, M., Rakhmilevitch, D., Palevski, A. & Dagan, Y. Tuning Spin-Orbit Coupling and Superconductivity at the $SrTiO_3/LaAlO_3$ Interface: A Magnetotransport Study. *Phys Rev Lett* **104**, (2010).
[55] Caviglia, A. D. *et al.* Tunable Rashba Spin-Orbit Interaction at Oxide Interfaces. *Phys Rev Lett* **104**, (2010).
[56] Bark, C. W. *et al.* Switchable induced polarization in $LaAlO_3/SrTiO_3$ heterostructures. *Nano Lett* **12**, 1765-1771, (2012).
[57] Cen, C., Thiel, S., Mannhart, J. & Levy, J. Oxide Nanoelectronics on Demand. *Science* **323**, 1026-1030, (2009).
[58] Reyren, N. *et al.* Anisotropy of the superconducting transport properties of the LaAlO3/SrTiO3 interface. *Appl Phys Lett* **94**, (2009).
[59] Cheng, G. *et al.* Electron pairing without superconductivity. *Nature* **521**, 196-199, (2015).
[60] Joshua, A., Ruhman, J., Pecker, S., Altman, E. & Ilani, S. Gate-tunable polarized phase of two-dimensional electrons at the $LaAlO_3/SrTiO_3$ interface. *PNAS* **110**, 9633, (2013).
[61] Banerjee, S., Erten, O. & Randeria, M. Ferromagnetic exchange, spin-orbit coupling and spiral magnetism at the LaAlO3/SrTiO3 interface. *Nat Phys* **9**, 625-629, (2013).
[62] Michaeli, K., Potter, A. C. & Lee, P. A. Superconducting and Ferromagnetic Phases in $SrTiO_3/LaAlO_3$ Oxide Interface Structures: Possibility of Finite Momentum Pairing. *Phys Rev Lett* **108**, (2012).
[63] Pavlenko, N., Kopp, T., Tsymbal, E. Y., Mannhart, J. & Sawatzky, G. A. Oxygen vacancies at titanate interfaces: Two-dimensional magnetism and orbital reconstruction. *Phys Rev B* **86**, (2012).

[64] Salluzzo, M. *et al.* Origin of Interface Magnetism in BiMnO3/SrTiO3 and LaAlO3/SrTiO3 Heterostructures. *Phys Rev Lett* **111**, (2013).

[65] Loder, F., Kampf, A. P. & Kopp, T. Superconductivity with Rashba spin-orbit coupling and magnetic field. *J Phys-Condens Mat* **25**, (2013).

[66] Kim, Y., Lutchyn, R. M. & Nayak, C. Origin and transport signatures of spin-orbit interactions in one- and two-dimensional SrTiO3-based heterostructures. *Phys Rev B* **87**, (2013).

[67] Huang, M. *et al.* Non-local piezoresponse of $LaAlO_3/SrTiO_3$ heterostructures. *Appl Phys Lett* **104**, (2014).

[68] Bi, F. *et al.* Electro-mechanical response of top-gated LaAlO3/SrTiO3. *J Appl Phys* **119**, (2016).

[69] Huang, M. C. *et al.* Direct imaging of LaAlO3/SrTiO3 nanostructures using piezoresponse force microscopy. *Apl Mater* **1**, (2013).

[70] Sharma, P. *et al.* Mechanical Tuning of LaAlO3/SrTiO3 Interface Conductivity. *Nano Lett* **15**, 3547-3551, (2015).

[71] Kumar, A. *et al.* Probing surface and bulk electrochemical processes on the LaAlO3-SrTiO3 interface. *ACS nano* **6**, 3841-3852, (2012).

[72] Huang, M. C. *et al.* Non-local piezoresponse of $LaAlO_3/SrTiO_3$ heterostructures. *Appl Phys Lett* **104**, 161606, (2014).

[73] Smith, H. M. & Turner, A. F. Vacuum Deposited Thin Films Using a Ruby Laser. *Appl Optics* **4**, 147, (1965).

[74] A. Y. Cho, J. R. A. Molecular beam expitaxy. *Progress in Solid State Chemistry* **10**, 157-191, (1975).

[75] Segal, Y., Ngai, J. H., Reiner, J. W., Walker, F. J. & Ahn, C. H. X-ray photoemission studies of the metal-insulator transition in LaAlO3/SrTiO3 structures grown by molecular beam epitaxy. *Phys Rev B* **80**, (2009).

[76] Sbrockey, N. M. *et al.* $LaAlO_3/SrTiO_3$ Epitaxial Heterostructures by Atomic Layer Deposition. *J Electron Mater* **41**, 819-823, (2012).

[77] Kawasaki, M. *et al.* Atomic Control of the SrTiO3 Crystal Surface. *Science* **266**, 1540-1542, (1994).

[78] Koster, G., Kropman, B. L., Rijnders, G. J. H. M., Blank, D. H. A. & Rogalla, H. Quasi-ideal strontium titanate crystal surfaces through formation of strontium hydroxide. *Appl Phys Lett* **73**, 2920-2922, (1998).

[79] Bark, C. W. *et al.* Tailoring a two-dimensional electron gas at the LaAlO3/SrTiO3 (001) interface by epitaxial strain. *P Natl Acad Sci USA* **108**, 4720-4724, (2011).

[80] Warusawithana, M. P. *et al.* $LaAlO_3$ stoichiometry is key to electron liquid formation at $LaAlO_3/SrTiO_3$ interfaces. *Nat Commun* **4**, (2013).

[81] Sato, H. K., Bell, C., Hikita, Y. & Hwang, H. Y. Stoichiometry control of the electronic properties of the LaAlO3/SrTiO3 heterointerface. *Appl Phys Lett* **102**, (2013).

[82] Sambri, A. *et al.* Plasma plume effects on the conductivity of amorphous-LaAlO3/SrTiO3 interfaces grown by pulsed laser deposition in O-2 and Ar. *Appl Phys Lett* **100**, (2012).

[83] Nakagawa, N., Hwang, H. Y. & Muller, D. A. Why some interfaces cannot be sharp. *Nat Mater* **5**, 204-209, (2006).

[84] Pentcheva, R. & Pickett, W. E. Avoiding the Polarization Catastrophe in $LaAlO_3$ Overlayers on $SrTiO_3$(001) through Polar Distortion. *Phys Rev Lett* **102**, (2009).

[85] Kalabukhov, A. *et al.* Effect of oxygen vacancies in the $SrTiO_3$ substrate on the electrical properties of the $LaAlO_3/SrTiO_3$ interface. *Phys Rev B* **75**, (2007).

[86] Herranz, G. *et al.* High mobility in LaAlO3/SrTiO3 heterostructures: Origin, dimensionality, and perspectives. *Phys Rev Lett* **98**, (2007).

[87] Siemons, W. *et al.* Origin of charge density at LaAlO3 on SrTiO3 heterointerfaces: Possibility of intrinsic doping. *Phys Rev Lett* **98**, (2007).

[88] Zhong, Z. C., Xu, P. X. & Kelly, P. J. Polarity-induced oxygen vacancies at LaAlO3/SrTiO3 interfaces. *Phys Rev B* **82**, (2010).

[89] Li, Y., Phattalung, S. N., Limpijumnong, S., Kim, J. & Yu, J. Formation of oxygen vacancies and charge carriers induced in the n-type interface of a LaAlO3 overlayer on SrTiO3(001). *Phys Rev B* **84**, (2011).

[90] Liu, Z. Q. *et al.* Origin of the Two-Dimensional Electron Gas at LaAlO3/SrTiO3 Interfaces: The Role of Oxygen Vacancies and Electronic Reconstruction. *Physical Review X* **3**, (2013).

[91] Rice, W. D. *et al.* Persistent optically induced magnetism in oxygen-deficient strontium titanate. *Nat Mater* **13**, 481-487, (2014).

[92] Willmott, P. R. *et al.* Structural basis for the conducting interface between $LaAlO_3$ and $SrTiO_3$. *Phys Rev Lett* **99**, (2007).

[93] Qiao, L., Droubay, T. C., Kaspar, T. C., Sushko, P. V. & Chambers, S. A. Cation mixing, band offsets and electric fields at $LaAlO_3/SrTiO_3$ (001) heterojunctions with variable La:Al atom ratio. *Surf Sci* **605**, 1381-1387, (2011).

[94] Xie, Y. W., Hikita, Y., Bell, C. & Hwang, H. Y. Control of electronic conduction at an oxide heterointerface using surface polar adsorbates. *Nat Commun* **2**, (2011).

[95] Arras, R., Ruiz, V. G., Pickett, W. E. & Pentcheva, R. Tuning the two-dimensional electron gas at the LaAlO3/SrTiO3(001) interface by metallic contacts. *Phys Rev B* **85**, (2012).

[96] Chan, N. Y. *et al.* Palladium Nanoparticle Enhanced Giant Photoresponse at LaAl3/SrTiO3 Two-Dimensional Electron Gas Heterostructures. *ACS nano* **7**, 8673-8679, (2013).

[97] Jnawali, G. *et al.* Photoconductive response of a single Au nanorod coupled to LaAlO3/SrTiO3 nanowires. *Appl Phys Lett* **106**, (2015).

[98] Tra, V. T. *et al.* Ferroelectric Control of the Conduction at the LaAlO3/SrTiO3 Heterointerface. *Adv Mater* **25**, 3357-3364, (2013).

[99] Huijben, M. *et al.* Defect Engineering in Oxide Heterostructures by Enhanced Oxygen Surface Exchange. *Adv Funct Mater* **23**, 5240-5248, (2013).

[100] Son, W. J., Cho, E., Lee, J. & Han, S. Hydrogen adsorption and carrier generation in LaAlO3-SrTiO3 heterointerfaces: a first-principles study. *Journal of physics. Condensed matter : an Institute of Physics journal* **22**, 315501, (2010).

[101] Bristowe, N. C., Littlewood, P. B. & Artacho, E. Surface defects and conduction in polar oxide heterostructures. *Phys Rev B* **83**, (2011).

[102] Li, Y. & Yu, J. Modulation of electron carrier density at the n-type LaAlO3/SrTiO3 interface by water adsorption. *J Phys-Condens Mat* **25**, (2013).

[103] Brown, K. A. *et al.* Giant conductivity switching of LaAlO3/SrTiO3 heterointerfaces governed by surface protonation. *Nat Commun* **7**, (2016).

[104] Klinov, D. & Magonov, S. True molecular resolution in tapping-mode atomic force microscopy with high-resolution probes. *Appl Phys Lett* **84**, 2697-2699, (2004).

[105] Lauritsen, J. V. & Reichling, M. Atomic resolution non-contact atomic force microscopy of clean metal oxide surfaces. *J Phys-Condens Mat* **22**, (2010).

[106] Binnig, G. K. Atomic-Force Microscopy. *Phys Scripta* **T19a**, 53-54, (1987).
[107] Geisse, N. A. AFM and combined optical techniques. *Mater Today* **12**, 40-45, (2009).
[108] Kenton, B. J., Fleming, A. J. & Leang, K. K. Compact ultra-fast vertical nanopositioner for improving scanning probe microscope scan speed. *Rev Sci Instrum* **82**, (2011).
[109] Huo, F. W. *et al.* Polymer pen lithography. *Science* **321**, 1658-1660, (2008).
[110] McGuire, N. K. Windows on a Small World. *Today's Chemist At Work*, (2002).
[111] Zhong, Q., Inniss, D., Kjoller, K. & Elings, V. B. Fractured Polymer Silica Fiber Surface Studied by Tapping Mode Atomic-Force Microscopy. *Surf Sci* **290**, L688-L692, (1993).
[112] Geng, Y. N. *et al.* Direct visualization of magnetoelectric domains. *Nat Mater* **13**, 163-167, (2014).
[113] Son, W. J., Cho, E., Lee, J. & Han, S. Hydrogen adsorption and carrier generation in LaAlO3-SrTiO3 heterointerfaces: a first-principles study. *J Phys-Condens Mat* **22**, (2010).
[114] Bi, F. *et al.* 'Water-cycle' mechanism for writing and erasing nanostructures at the LaAlO3/SrTiO3 interface (vol 97, 173110, 2010). *Appl Phys Lett* **100**, (2012).
[115] Irvin, P. *et al.* Gigahertz-frequency operation of a LaAlO3/SrTiO3-based nanotransistor. *Appl Phys Lett* **102**, (2013).
[116] Cheng, G. L. *et al.* Sketched oxide single-electron transistor. *Nat Nanotechnol* **6**, 343-347, (2011).
[117] Bogorin, D. F. *et al.* Nanoscale rectification at the $LaAlO_3/SrTiO_3$ interface. *Appl Phys Lett* **97**, (2010).
[118] Irvin, P. *et al.* Rewritable nanoscale oxide photodetector. *Nat Photonics* **4**, 849-852, (2010).
[119] Ma, Y. J. *et al.* Broadband Terahertz Generation and Detection at 10 nm Scale. *Nano Lett* **13**, 2884-2888, (2013).
[120] Veazey, J. P. *et al.* Oxide-based platform for reconfigurable superconducting nanoelectronics. *Nanotechnology* **24**, (2013).
[121] Veazey, J. P. *et al.* Nonlocal current-voltage characteristics of gated superconducting sketched oxide nanostructures. *Epl-Europhys Lett* **103**, (2013).
[122] Irvin, P. *et al.* Anomalous High Mobility in $LaAlO_3/SrTiO_3$ Nanowires. *Nano Lett* **13**, 364-368, (2013).
[123] Xie, Y., Bell, C., Yajima, T., Hikita, Y. & Hwang, H. Y. Charge Writing at the $LaAlO_3/SrTiO_3$ Surface. *Nano Lett* **10**, 2588-2591, (2010).
[124] Cancellieri, C. *et al.* Electrostriction at the LaAlO3/SrTiO3 Interface. *Phys Rev Lett* **107**, (2011).
[125] Maurice, J. L. *et al.* Electronic conductivity and structural distortion at the interface between insulators $SrTiO_3$ and $LaAlO_3$. *Phys Status Solidi A* **203**, 2209-2214, (2006).
[126] Vonk, V. *et al.* Interface structure of $SrTiO_3/LaAlO_3$ at elevated temperatures studied in situ by synchrotron x rays. *Phys Rev B* **75**, (2007).
[127] Zhou, K. J. *et al.* Localized and delocalized Ti 3d carriers in LaAlO3/SrTiO3 superlattices revealed by resonant inelastic x-ray scattering. *Phys Rev B* **83**, (2011).
[128] Park, M. S., Rhim, S. H. & Freeman, A. J. Charge compensation and mixed valency in LaAlO3/SrTiO3 heterointerfaces studied by the FLAPW method. *Phys Rev B* **74**, (2006).
[129] Jesse, S., Mirman, B. & Kalinin, S. V. Resonance enhancement in piezoresponse force microscopy: Mapping electromechanical activity, contact stiffness, and Q factor. *Appl Phys Lett* **89**, (2006).
[130] Li, L. *et al.* Very Large Capacitance Enhancement in a Two-Dimensional Electron System. *Science* **332**, 825-828, (2011).

[131] Jany, R. *et al.* Diodes with breakdown voltages enhanced by the metal-insulator transition of LaAlO3-SrTiO3 interfaces. *Appl Phys Lett* **96**, (2010).

[132] Singh-Bhalla, G. *et al.* Built-in and induced polarization across LaAlO3/SrTiO3 heterojunctions. *Nat Phys* **7**, 80-86, (2011).

[133] Soergel, E. Piezoresponse force microscopy (PFM). *J Phys D Appl Phys* **44**, (2011).

[134] Eliseev, E. A., Kalinin, S. V., Jesse, S., Bravina, S. L. & Morozovska, A. N. Electromechanical detection in scanning probe microscopy: Tip models and materials contrast. *J Appl Phys* **102**, (2007).

[135] Zhao, M. H., Wang, Z. L. & Mao, S. X. Piezoelectric characterization of individual zinc oxide nanobelt probed by piezoresponse force microscope. *Nano Lett* **4**, 587-590, (2004).

[136] Agronin, A. G., Rosenwaks, Y. & Rosenman, G. I. Piezoelectric coefficient measurements in ferroelectric single crystals using high voltage atomic force microscopy. *Nano Lett* **3**, 169-171, (2003).

[137] Xie, S. H. *et al.* High resolution quantitative piezoresponse force microscopy of BiFeO3 nanofibers with dramatically enhanced sensitivity. *Nanoscale* **4**, 408-413, (2012).

[138] Gruverman, A. & Kalinin, S. V. Piezoresponse force microscopy and recent advances in nanoscale studies of ferroelectrics. *J Mater Sci* **41**, 107-116, (2006).

[139] Jia, C. L. *et al.* Oxygen octahedron reconstruction in the SrTiO3/LaAlO3 heterointerfaces investigated using aberration-corrected ultrahigh-resolution transmission electron microscopy. *Phys Rev B* **79**, (2009).

[140] Kalinin, S. V., Borisevich, A. & Fong, D. Beyond Condensed Matter Physics on the Nanoscale: The Role of Ionic and Electrochemical Phenomena in the Physical Functionalities of Oxide Materials. *ACS nano* **6**, 10423-10437, (2012).

[141] Kim, Y. *et al.* Ionically-Mediated Electromechanical Hysteresis in Transition Metal Oxides. *ACS nano* **6**, 7026-7033, (2012).

[142] Jiang, W. *et al.* Mobility of oxygen vacancy in $SrTiO_3$ and its implications for oxygen-migration-based resistance switching. *J Appl Phys* **110**, (2011).

[143] Jahn, H. A. & Teller, E. *Proc. R. Soc. (London)* **161**, 220, (1937).

[144] Zubko, P., Catalan, G., Buckley, A., Welche, P. R. L. & Scott, J. F. Strain-Gradient-Induced Polarization in $SrTiO_3$ Single Crystals. *Phys Rev Lett* **99**, 167601, (2007).

[145] Okamoto, S., Millis, A. J. & Spaldin, N. A. Lattice relaxation in oxide heterostructures: LaTiO3/SrTiO3 superlattices. *Phys Rev Lett* **97**, (2006).

[146] Song, Y., Noh, T. W., Lee, S. I. & Gaines, J. R. Experimental-Study of the 3-Dimensional Ac Conductivity and Dielectric-Constant of a Conductor-Insulator Composite near the Percolation-Threshold. *Phys Rev B* **33**, 904-908, (1986).

[147] Huang, M. C. *et al.* Electric field effects in graphene/LaAlO3/SrTiO3 heterostructures and nanostructures. *Apl Mater* **3**, (2015).

[148] Novoselov, K. S. *et al.* Electric field effect in atomically thin carbon films. *Science* **306**, 666-669, (2004).

[149] Zhang, Y. B., Tan, Y. W., Stormer, H. L. & Kim, P. Experimental observation of the quantum Hall effect and Berry's phase in graphene. *Nature* **438**, 201-204, (2005).

[150] Novoselov, K. S. *et al.* Room-temperature quantum hall effect in graphene. *Science* **315**, 1379-1379, (2007).

[151] Geim, A. K. & Novoselov, K. S. The rise of graphene. *Nat Mater* **6**, 183-191, (2007).

[152] Castro Neto, A. H., Guinea, F., Peres, N. M. R., Novoselov, K. S. & Geim, A. K. The electronic properties of graphene. *Rev Mod Phys* **81**, 109-162, (2009).

[153] Hong, X., Zou, K., DaSilva, A. M., Ahn, C. H. & Zhu, J. Integrating functional oxides with graphene. *Solid State Commun* **152**, 1365-1374, (2012).

[154] Zheng, Y. *et al.* Wafer-scale graphene/ferroelectric hybrid devices for low-voltage electronics. *Epl-Europhys Lett* **93**, (2011).

[155] Jin, D. F., Kumar, A., Fung, K. H., Xu, J. & Fang, N. X. Terahertz plasmonics in ferroelectric-gated graphene. *Appl Phys Lett* **102**, (2013).

[156] Andress, W. F. *et al.* Ultra-subwavelength two-dimensional plasmonic circuits. *Nano Lett* **12**, 2272-2277, (2012).

[157] Novoselov, K. S. *et al.* Two-dimensional gas of massless Dirac fermions in graphene. *Nature* **438**, 197-200, (2005).

[158] Gupta, A., Chen, G., Joshi, P., Tadigadapa, S. & Eklund, P. C. Raman scattering from high-frequency phonons in supported n-graphene layer films. *Nano Lett* **6**, 2667-2673, (2006).

[159] Vlassiouk, I. *et al.* Role of Hydrogen in Chemical Vapor Deposition Growth of Large Single-Crystal Graphene. *ACS nano* **5**, 6069-6076, (2011).

[160] Dhingra, S., Hsu, J. F., Vlassiouk, I. & D'Urso, B. Chemical vapor deposition of graphene on large-domain ultra-flat copper. *Carbon* **69**, 188-193, (2014).

[161] Lui, C. H., Liu, L., Mak, K. F., Flynn, G. W. & Heinz, T. F. Ultraflat graphene. *Nature* **462**, 339-341, (2009).

[162] Ishigami, M., Chen, J. H., Cullen, W. G., Fuhrer, M. S. & Williams, E. D. Atomic structure of graphene on SiO2. *Nano Lett* **7**, 1643-1648, (2007).

[163] Nilsen, W. G. & Skinner, J. G. Raman Spectrum of Strontium Titanate. *J Chem Phys* **48**, 2240-&, (1968).

[164] Yan, J., Zhang, Y. B., Kim, P. & Pinczuk, A. Electric field effect tuning of electron-phonon coupling in graphene. *Phys Rev Lett* **98**, (2007).

[165] Kalbac, M. *et al.* The Influence of Strong Electron and Hole Doping on the Raman Intensity of Chemical Vapor-Deposition Graphene. *ACS nano* **4**, 6055-6063, (2010).

[166] Rao, C. N. R., Sood, A. K., Voggu, R. & Subrahmanyam, K. S. Some Novel Attributes of Graphene. *J Phys Chem Lett* **1**, 572-580, (2010).

[167] Abrahams, E., Anderson, P. W., Licciardello, D. C. & Ramakrishnan, T. V. Scaling Theory of Localization - Absence of Quantum Diffusion in 2 Dimensions. *Phys Rev Lett* **42**, 673-676, (1979).

[168] Hikami, S., Larkin, A. I. & Nagaoka, Y. Spin-Orbit Interaction and Magnetoresistance in the 2 Dimensional Random System. *Prog Theor Phys* **63**, 707-710, (1980).

[169] Bergman, G. Influence of Spin-Orbit-Coupling on Weak Localization. *Phys Rev Lett* **48**, 1046-1049, (1982).

[170] Bergmann, G. Weak Localization in Thin-Films - a Time-of-Flight Experiment with Conduction Electrons. *Phys Rep* **107**, 1-58, (1984).

[171] Konschuh, S., Gmitra, M. & Fabian, J. Tight-binding theory of the spin-orbit coupling in graphene. *Phys Rev B* **82**, (2010).

[172] McCann, E. *et al.* Weak-localization magnetoresistance and valley symmetry in graphene. *Phys Rev Lett* **97**, (2006).

[173] Morozov, S. V. *et al.* Strong suppression of weak localization in graphene. *Phys Rev Lett* **97**, (2006).

[174] Tikhonenko, F. V., Horsell, D. W., Gorbachev, R. V. & Savchenko, A. K. Weak localization in graphene flakes. *Phys Rev Lett* **100**, (2008).

[175] Horsell, D. W., Tikhonenko, F. V., Gorbachev, R. V. & Savchenko, A. K. Weak localization in monolayer and bilayer graphene. *Philos T R Soc A* **366**, 245-250, (2008).

[176] Wu, X. S., Li, X. B., Song, Z. M., Berger, C. & de Heer, W. A. Weak antilocalization in epitaxial graphene: Evidence for chiral electrons. *Phys Rev Lett* **98**, (2007).

[177] Tikhonenko, F. V., Kozikov, A. A., Savchenko, A. K. & Gorbachev, R. V. Transition between Electron Localization and Antilocalization in Graphene. *Phys Rev Lett* **103**, (2009).

[178] Rycerz, A., Tworzydlo, J. & Beenakker, C. W. J. Valley filter and valley valve in graphene. *Nat Phys* **3**, 172-175, (2007).

[179] San-Jose, P., Prada, E., McCann, E. & Schomerus, H. Pseudospin Valve in Bilayer Graphene: Towards Graphene-Based Pseudospintronics. *Phys Rev Lett* **102**, (2009).

[180] Pesin, D. & MacDonald, A. H. Spintronics and pseudospintronics in graphene and topological insulators. *Nat Mater* **11**, 409-416, (2012).

[181] Banerjee, S. K., Register, L. F., Tutuc, E., Reddy, D. & MacDonald, A. H. Bilayer PseudoSpin Field-Effect Transistor (BiSFET): A Proposed New Logic Device. *Ieee Electr Device L* **30**, 158-160, (2009).

[182] Ando, T. Screening effect and impurity scattering in monolayer graphene. *J Phys Soc Jpn* **75**, (2006).

[183] Hwang, E. H., Adam, S. & Das Sarma, S. Carrier transport in two-dimensional graphene layers. *Phys Rev Lett* **98**, (2007).

[184] Dean, C. R. *et al.* Boron nitride substrates for high-quality graphene electronics. *Nat Nanotechnol* **5**, 722-726, (2010).

[185] Zheng, Y. *et al.* Gate-controlled nonvolatile graphene-ferroelectric memory. *Appl Phys Lett* **94**, (2009).

[186] Giesbers, A. J. M. *et al.* Nanolithography and manipulation of graphene using an atomic force microscope. *Solid State Commun* **147**, 366-369, (2008).

[187] Weng, L. S., Zhang, L. Y., Chen, Y. P. & Rokhinson, L. P. Atomic force microscope local oxidation nanolithography of graphene. *Appl Phys Lett* **93**, (2008).

[188] Hong, X. *et al.* Unusual resistance hysteresis in n-layer graphene field effect transistors fabricated on ferroelectric Pb(Zr0.2Ti0.8)O-3. *Appl Phys Lett* **97**, (2010).

[189] Saha, S. *et al.* Unconventional Transport through Graphene on SrTiO3: A Plausible Effect of SrTiO3 Phase-Transitions. *Sci Rep-Uk* **4**, (2014).

[190] Sachs, R., Lin, Z. S. & Shi, J. Ferroelectric-like SrTiO3 surface dipoles probed by graphene. *Sci Rep-Uk* **4**, (2014).

[191] Wang, H. M., Wu, Y. H., Cong, C. X., Shang, J. Z. & Yu, T. Hysteresis of Electronic Transport in Graphene Transistors. *ACS nano* **4**, 7221-7228, (2010).

[192] Xu, H., Chen, Y. B., Zhang, J. & Zhang, H. L. Investigating the Mechanism of Hysteresis Effect in Graphene Electrical Field Device Fabricated on SiO2 Substrates using Raman Spectroscopy. *Small* **8**, 2833-2840, (2012).

[193] Martin, J. *et al.* Observation of electron-hole puddles in graphene using a scanning single-electron transistor. *Nat Phys* **4**, 144-148, (2008).

[194] Hong, X., Posadas, A., Zou, K., Ahn, C. H. & Zhu, J. High-Mobility Few-Layer Graphene Field Effect Transistors Fabricated on Epitaxial Ferroelectric Gate Oxides. *Phys Rev Lett* **102**, (2009).

[195] Yusuf, M. H., Nielsen, B., Dawber, M. & Du, X. Extrinsic and Intrinsic Charge Trapping at the Graphene/Ferroelectric Interface. *Nano Lett* **14**, 5437-5444, (2014).

[196] Li, X. S. *et al.* Graphene Films with Large Domain Size by a Two-Step Chemical Vapor Deposition Process. *Nano Lett* **10**, 4328-4334, (2010).

[197] Gannett, W. *et al.* Boron nitride substrates for high mobility chemical vapor deposited graphene. *Appl Phys Lett* **98**, (2011).

[198] Lee, J. S. *et al.* Gate-controlled metal-insulator transition in the LaAlO3/SrTiO3 system with sub-critical LaAlO3 thickness. *Phys Status Solidi-R* **6**, 472-474, (2012).

[199] Berger, C. *et al.* Electronic confinement and coherence in patterned epitaxial graphene. *Science* **312**, 1191-1196, (2006).

[200] Ki, D. K., Jeong, D., Choi, J. H., Lee, H. J. & Park, K. S. Inelastic scattering in a monolayer graphene sheet: A weak-localization study. *Phys Rev B* **78**, (2008).

[201] Suzuura, H. & Ando, T. Crossover from symplectic to orthogonal class in a two-dimensional honeycomb lattice. *Phys Rev Lett* **89**, (2002).

[202] Ando, T. Effects of magnetic field and flux on perfect channel in metallic carbon nanotubes. *J Phys Soc Jpn* **73**, 1273-1280, (2004).

[203] Baker, A. M. R. *et al.* Weak localization scattering lengths in epitaxial, and CVD graphene. *Phys Rev B* **86**, (2012).

[204] Joshua, A., Pecker, S., Ruhman, J., Altman, E. & Ilani, S. A universal critical density underlying the physics of electrons at the $LaAlO_3/SrTiO_3$ interface. *Nat Commun* **3**, (2012).

[205] Drera, G. *et al.* Band offsets and density of Ti3+ states probed by x-ray photoemission on LaAlO3/SrTiO3 heterointerfaces and their LaAlO3 and SrTiO3 bulk precursors. *Phys Rev B* **87**, (2013).

[206] Kienzle, D., Koirala, P. & Marks, L. D. Lanthanum aluminate (110) 3 x 1 surface reconstruction. *Surf Sci* **633**, 60-67, (2015).

[207] Hanzig, J. *et al.* Single crystal strontium titanate surface and bulk modifications due to vacuum annealing. *J Appl Phys* **110**, (2011).

[208] Franks, G. V. & Meagher, L. The isoelectric points of sapphire crystals and alpha-alumina powder. *Colloid Surface A* **214**, 99-110, (2003).

[209] Tebano, A., Fabbri, E., Pergolesi, D., Balestrino, G. & Traversa, E. Room-Temperature Giant Persistent Photoconductivity in $SrTiO_3/LaAlO_3$ Heterostructures. *ACS Nano* **6**, 1278-1283, (2012).

[210] Liu, Z. Q. *et al.* Metal-Insulator Transition in $SrTiO_{3-x}$ Thin Films Induced by Frozen-Out Carriers. *Phys. Rev. Lett.* **107**, 146802, (2011).

[211] Nakagawa, N., Hwang, H. Y. & Muller, D. A. Why some interfaces cannot be sharp. *Nature Mater.* **5**, 204-209, (2006).

[212] Wagner, F. T. & Somorjai, G. A. Photocatalytic and photoelectrochemical hydrogen production on strontium titanate single crystals. *J. Am. Chem. Soc.* **102**, 5494-5502, (1980).

[213] Peña, M. A. & Fierro, J. L. G. Chemical Structures and Performance of Perovskite Oxides. *Chemical Reviews* **101**, 1981-2018, (2001).